Brillouin scattering in optophononic heterostructures working at ultrahigh acoustic frequencies

Anne Rodriguez

université
PARIS-SACLAY

Brillouin scattering in optophononic heterostructures working at ultrahigh acoustic frequencies

Diffusion Brillouin dans des hétérostructures optophononiques fonctionnant à des fréquences acoustiques ultra-hautes

Thèse de doctorat de l'Université Paris-Saclay

École doctorale n° 572, Ondes et Matière (EDOM)
Spécialité de doctorat: Physique
Graduate School : Physique. Référent : Faculté des sciences d'Orsay

Thèse préparée dans l'unité de recherche **Centre de Nanosciences et de Nanotechnologies** (Université Paris-Saclay, CNRS), sous la direction de **Daniel LANZILLOTTI-KIMURA**, Chargé de recherche.

Thèse soutenue à Palaiseau, le 20/03/2023, par

Anne RODRIGUEZ

Composition du jury

Membres du jury avec voix délibérative

Delphine MARRIS-MORINI Professeure des universités, C2N - CNRS, Université Paris-Saclay	Présidente
Olivier BOURGEOIS Directeur de recherche, Institut Néel - Université Grenoble-Alpes, CNRS	Rapporteur & Examinateur
Jérémie MARGUERITAT Chargé de recherche, Institut Lumière matière - Université de Lyon	Rapporteur & Examinateur
Clivia SOTOMAYOR-TORRES Professeure, ICN2 - Universitat Autonoma de Barcelona	Examinatrice
Chris STURM Docteur, Felix-Bloch-Institut für Festkörperphysik - Universität Leipzig	Examinateur

Thèse de doctorat

NNT: 2023UPASP031

université PARIS-SACLAY

ÉCOLE DOCTORALE
Ondes et matière
(EDOM)

Titre: Diffusion Brillouin dans des hétérostructures optophononiques fonctionnant à des fréquences acoustiques ultra-hautes

Mots clés: Diffusion Brillouin, acoustique, nanomécanique, topologie

Résumé: La nanophononique, c'est-à-dire l'ingénierie des phonons acoustiques, est un domaine de recherche prometteur qui offre un potentiel dans la manipulation du son et de la chaleur à l'échelle nanométrique. La recherche sur les propriétés vibratoires des systèmes formés par des multicouches de semi-conducteurs a permis d'atteindre un nouveau niveau de compréhension des phonons acoustiques dans ces structures. Dans ce travail, nous présentons des dispositifs phononiques topologiques constitués de super-réseaux de semiconducteurs permettant de contrôler la propagation des phonons dans la gamme des dizaines au centaines de gigahertz. Nous avons développé des schémas expérimentaux de spectroscopie Brillouin pour accéder aux modes acoustiques confinés dans des cavités optophononiques planaires et micropiliers où la lumière dans le proche infrarouge et les phonons acoustiques dans la gamme des 20 GHz peuvent être confinés simultanément.

Title: Brillouin scattering in optophononic heterostructures working at ultrahigh acoustic frequencies

Keywords: Brillouin scattering, acoustics, nanomechanics, topology

Abstract: Nanophononics, i.e. acoustic phonon engineering, is a promising research domain with potential in the manipulation of sound and heat at the nanometric scales. Research on the vibrational properties of systems formed by semiconductor multilayers has permitted to achieve a new level of understanding of acoustic phonons in these structures. In this work we introduce topological phononic devices made of semiconductor superlattices to control the propagation and confinement of acoustic phonons in the tens to hundreds of gigahertz range. We developed Brillouin spectroscopy experimental schemes to access the confined acoustic modes in planar and micropillar optophononic cavities where both light in the near infrared range and acoustic phonons in the 20 GHz range can be simultaneously confined.

Résumé

L'objectif de cette thèse est de contrôler les phonons à l'échelle nanométrique par l'ingénierie de nouvelles hétérostructures GaAs/AlAs et de développer de nouveaux schémas de spectroscopie Brillouin pour étudier les phonons acoustiques confinés à ultra-hautes fréquences.
Le contrôle précis de la dynamique des phonons acoustiques a permis l'ingénierie des interactions avec d'autres excitations (photons, électrons, magnons, polaritons ou plasmons). Pour cela, une grande variété de systèmes a été développée pour contrôler la propagation et le confinement des phonons à haute fréquence à l'échelle nanométrique (nanodisques, micropiliers, nanotrompettes, cristaux phononiques unidimensionnels, et tambours). Les super-réseaux faits à partir de GaAs/AlAs permettent de contrôler le champ acoustique à ultra-hautes fréquences avec une grande précision. Ces structures permettent de concevoir des miroirs acoustiques, des cavités Fabry-Pérot ou des filtres. Les systèmes multicouches de semi-conducteurs peuvent également être gravés en forme des micropiliers, ce qui permet de contrôler les champs optique et acoustique en trois dimensions. Contrairement à l'acoustique macroscopique, l'absence de transducteurs standards dans la gamme de fréquences allant du GHz au THz encourage le développement de techniques optiques pour accéder expérimentalement aux modes acoustiques des systèmes étudiés.
Dans cette thèse, nous abordons les défis théoriques et expérimentaux dans le domaine de la nanophononique. Le premier axe de recherche est l'ingénierie de structures multicouches basées sur des concepts topologiques pour contrôler le confinement des phonons acoustiques à haute fréquences. Nous étudions le confinement des phonons dans des dispositifs topologiques, imitant le comportement topologique déjà observé en acoustique macroscopique, optique ou électronique. La deuxième ligne de recherche consiste à développer des schémas optiques pour mesurer les modes acoustiques confinés dans des microstructures multicouches. Plus précisément, il s'agit de faire progresser les expériences de diffusion Brillouin spontanée pour accéder aux modes acoustiques à 18 GHz dans des cavités planaires et en trois dimensions. Le manuscrit présente cinq chapitres qui vont des concepts théoriques utilisés dans cette thèse, aux simulations et aux résultats expérimentaux obtenus au cours de la thèse.
Le premier chapitre est dédié à présenter les concepts qui permettent de contrôler la propagation d'ondes acoustiques dans la gamme des GHz dans des systèmes multicouches. Nous rappelons qu'il est possible de modifier la bande interdite dans des super-réseaux pour fabriquer des réseaux de Bragg acoustiques et des cavités Fabry-Pérot. De plus, en raison d'une coïncidence par nature dans les matériaux GaAs/AlAs, il est possible de simultanément confiner la lumière et le son dans un résonateur Fabry-

Pérot à une longueur d'onde d'environ 900 nm et à une fréquence acoustique d'environ 18 GHz. Ces concepts sont à la base des résonateurs acoustiques étudiés dans cette thèse.
Le deuxième hapitre aborde l'interaction photoélastique qui a lieu entre la lumière et le son à l'échelle nanométrique. Nous présentons la diffusion Brillouin, qui est la diffusion inélastique de la lumière due à la présence de phonons dans le milieu. Nous rappelons les différentes règles de polarisation et de sélection géométrique de la diffusion Brillouin dans les matériaux semi-conducteurs nécessaires dans la suite de la thèse. Nous discutons également deux autres techniques expérimentales pour la détection de phonons. La première technique est la génération et la détection cohérente de phonons acoustiques, qui permet d'étudier la dynamique des phonons acoustiques cohérents dans le temps. La deuxième technique est la spectroscopie de bruit, habituellement utilisée en optomécanique. Dans cette thèse, nous étudions les modes acoustiques confinés dans les résonateurs optophoniques par le biais de la diffusion inélastique de la lumière avec la spectroscopie Brillouin.
Dans le troisième chapitre, nous présentons une méthode théorique pour générer un état d'interface acoustique dans un résonateur topologique, basée sur le principe de l'inversion de bande. En modifiant le ratio d'épaisseur des couches de GaAs et d'AlAs dans la cellule unitaire, les symétries des modes autour de la bande interdite changent. Un état d'interface est alors généré lorsque deux super-réseaux avec des symétries inversées sont concaténés.
Nous avons étendu ce principe pour créer des états d'interface dans les bandes interdites d'ordre élevé. En ajustant l'épaisseur des couches dans la cellule unitaire, nous avons pu générer de multiples états d'interface acoustiques topologiques dans une large gamme de fréquences. Nous avons également simulé des structures hybrides pour lesquelles un état d'interface est généré en combinant deux super-réseaux présentant des bandes interdites de différents ordres centrés autour de la même fréquence avec des symétries identiques. Il est ainsi possible d'explorer des structures topologiques inaccessibles en électronique ou en optique en raison des relations de dispersion. De plus, nous avons montré que, pour des super-réseaux conçus à des fréquences acoustiques 18 GHz et à la longueur d'onde optique 900 nm, l'inversion des symétries des modes de bord se produit simultanément dans les domaines optique et acoustique. Il en résulte un confinement simultané de la lumière et du son avec des états optiques et acoustiques colocalisés.
Dans le quatrième chapitre, nous démontrons expérimentalement la présence d'états d'interface acoustiques dans des cavités topologiques au moyen de la spectroscopie Brillouin. La technique développée permet d'accéder aux modes acoustiques dans la gamme de 18 à 300 GHz dans des cavités planaires. Nous bénéficions de la double résonance optique des cavités optiques multicouches qui induit un décalage angulaire entre le laser réfléchi et le signal Brillouin. Le signal est filtré à l'aide d'une fibre monomode ce qui améliore le rapport signal sur bruit. Cette technique est optimale pour des fréquences acoustiques dans la dizaine du GHz. De plus, l'utilisation d'un étalon avant le spectromètre permet de réduire la lumière parasite résiduelle et d'augmenter la résolution des spectres Brillouin (jusqu'à 2 GHz). Cependant, cette méthode est limitée aux mesures sur des cavités planaires en raison de la forte modification de la relation de dispersion optique de la cavité dans les objets tridimensionnels et de la diffraction de la lumière

imposée par des objets de taille micrométrique. Il est donc nécessaire de développer une technique adaptée à l'étude de micrcopiliers.
Dans le dernier chapitre, nous démontrons qu'il est possible de contrôler l'état de polarisation du signal de diffusion Brillouin dans des cavités optiques polarisées. Nous exploitons la rotation de polarisation dépendante de la longueur d'onde induite par l'ellipticité du micropilier pour contrôler indépendamment l'état de polarisation du signal Brillouin et du laser d'excitation réfléchi. Par conséquent, nous modifions les règles de sélection en polarisation de la diffusion Brillouin. En contrôlant la forme des micropiliers, nous contrôlons de manière déterministe l'état de polarisation du signal Brillouin. De plus, les polarisations des différents modes Brillouin peuvent être contrôlées indépendamment les unes des autres. Le contrôle de la polarisation du signal Brillouin permet d'implémenter un dispositif expérimental basé sur un filtrage en polarisation pour mesurer le signal d'intérêt dans gamme de quelques dizaines de GHz. Les résultats expérimentaux montrent que nous sommes capables de mesurer les modes Stokes et anti-Stokes de $\pm$ 18 GHz à $\pm$ 90 GHz dans un résonateur 3D. Il s'agit d'un défi technique, car la faible différence de longueur d'onde entre le signal Brillouin et le laser ne permet pas de filtrer en longueurs d'onde ni d'adapter les modes spatiaux des deux champs avant le filtrage spatial.
Nous avons étudié différents paramètres contrôlant l'état de polarisation de la diffusion Brillouin : la longueur d'onde du laser, l'ellipticité de la section transversale et l'état de polarisation du laser incident. En complément des expériences de spectroscopie Brillouin, nous avons effectué des simulations des différents états de polarisation qui soutiennent les spectres expérimentaux. Les conditions idéales pour mesurer sans bruit de fond les spectres de diffusion spontanée améliorée sans bruit de fond avec le meilleur filtrage possible est une interdépendance entre l'ellipticité de la section transversale, la longueur d'onde et l'état de polarisation du laser, ainsi que le couplage du mode de Brillouin les modes de la cavité optique.

Acknowledgements

I couldn't have done this journey alone. There are a lot of people who have encouraged me, helped me, and made my life through my thesis a great adventure, and this is the place to thank them all.

I want to thank Daniel for welcoming me in the team and for his guidance during my thesis. The discussions with him about physics (but not only) were the main thread of my thesis and I wouldn't be here without his advice. I want to thank all the colleagues and friends from the phonon team with whom I worked. To Omar, who has shown and guided me since my first day in the lab, I am very grateful, I have learnt a lot from him. He always supported me and became a great friend. To Martin, thanks for always answering my questions until the very end of my thesis. I learned a lot (and thanks for dropping me home in the evening). It was great working with him, and I had the chance to keep working with him even after he left the lab. To Priya with whom I spent a lot of time in the lab, and I had such a great time working with her. I want to thank her for her guidance, her positivity, and her friendship. I have learnt a lot, whether it be scientific knowledge or rigor. I wish you all the best for your next great adventure. To Edson, who always had an interesting input in scientific discussions, I am really thankful. Sharing time with him was really fulfilling and he always has a fun story to tell around a beer. Him and Chushuang also became great friends. To Chushuang, she arrived in the middle of my thesis. She has taken over Omar's experiment and is already showing impressive results in the transport measurements. I am sure she will succeed and achieve great results. To Kostas who arrived in the last month of my thesis. Thanks a lot for the support and the help to achieve my presentation.

I want to thank Loïc for all the discussions about polarization, it was a great help. I want to thank Olivier for being my thesis supervisor when Daniel didn't have his HDR. I want to thank the GOSS team for all their support and help, but also for the great time we had together. I learned a lot about quantum optics with them, and I have also made good friends! Thanks Ilse, Dario, Sarah and all the others. I would especially like to thank Elham for making my time in the GOSS team so wonderful. We started our internship and then our thesis together, and you became a great friend of mine. Thanks for the endless discussions and all the support (and for the beautiful colormap). Soon it will be your turn to defend and I'm sure you will do a fantastic job! I want to thank the people who shared my office and among others Nicolas and Martin with whom I shared a lot of time.

I thank the IT service and administration for their help through my thesis and particularly Christophe Chassat for printing all copies of my thesis. I want to thank the groups of Aristide Lemaître and Isabelle Sagnes. Without them, I couldn't have done

experiments.

I want to thank all jury members for having taken the time to read and review my manuscript.

I want to thank Jack for proofreading my manuscript, even though he probably understood nothing of it. I thank Clara for the support, the laugh, and the discussions. The orchestra wouldn't have been the same without you. And one day we will manage to play our duet! Merci à Alexandre pour m'avoir soutenu, encouragé et supporté pendant ces années. Merci pour les délicieux repas et pour m'avoir écouté raconter ma thèse en long et en large. Merci à ma famille et à mes ami(e)s pour leur soutien et leur amour sans lesquels je ne serais pas arrivée si loin.

Contents

Motivation

Nanophononics refers to the study and manipulation of acoustic phonons at the nanoscale [1–4]. The objective of this thesis is to control phonons at the nanoscale by engineering novel GaAs/AlAs heterostructures and to develop new Brillouin spectroscopy schemes to study the confined acoustic phonons at ultrahigh frequencies.
The engineering of acoustic waves at the nanoscale is based on the design of structures to control the propagation of phonons. Acoustic waves can be controlled in a very broad frequency range; from Hertz to terahertz using similar engineering principles. For instance, mechanical waves in the infrasound have low frequencies (up to a few Hz) and are associated to long wavelengths in the order of hundreds of meters. At this scale, the study of acoustic waves can provide information about what happens in the ocean, such as whale vocalizations or seismic events [5]. It also allows the identification of earthquake sources [6]. The human audible domain covers the frequency range from 20 Hz to 20 kHz, with wavelengths of a few meters. In this domain, noise has become an issue affecting human health. To address that problem, metamaterials have been developed to control the propagation of sound for architectural noise mitigation [7]. In addition, there is a variety of musical instruments with various sound generation processes. For example, castanets produce sound when the two shells forming the instrument are clapped together [8], while the sound generated by trombones is due to the interaction between the vibrating lips of the musician and the airflow in the instrument [9]. The study of audible sound can also benefit the exploration of the evolution of language in a small community of individuals in social sciences [10]. Acoustic waves with frequencies above the audible domain range and up to a few hundreds of MHz are known as ultrasound. There is a large scope of applications in the ultrasound domain, from medical sensing [11] to sound navigation ranging (SONAR) [12]. It also includes acoustic tweezers which can be applied to trap particles sensitive to the electromagnetic field [13]. Above a few hundreds of MHz, the mechanical vibrations are known as hypersound and can be used for sensing applications and nano-electro-mechanical systems (NEMS) [14, 15]. At this order of magnitude, the typical size of the devices is of a few tens to few hundred of micrometers. Finally, the control of mechanical vibrations in the GHz to THz range corresponds to the branch of nanophononics [1, 2, 4, 16, 17].

Acoustic phonons were considered as a main source of decoherence in solid-state systems and as a main heat carrier. The reduction of decoherence effects and the development of novel thermal management strategies are classical applications of acoustic phonon engineering at the nanoscale [18–20]. More recently, the fine control achieved over acoustic phonon dynamics enabled the engineering of interactions with other excitations: photons

[21–23], electrons [24], magnons [25], polaritons [26] or plasmons [27]. For this purpose, a large variety of devices were developed to control the propagation and confinement of phonons at high frequencies at the nanoscale, such as: nanodisks [28, 29], micropillars [30, 31], nanotrumpets [21, 32], one-dimensional phononic crystal [33, 34], and drums [35, 36].

Acoustic phonons at GHz−THz frequencies have a low occupation number at standard cryogenic temperatures enabling applications in the quantum regime [37–40]. Finally, the short wavelengths (of a few nanometers to few hundreds of nanometers) and the long mean free paths unlock new potential nanoscopies, and a simulation platform where large systems can be simulated (near-free electron approximation and tight-binding model) [41, 42]. Furthermore, the properties of solid-state systems affected by the position of the atoms can be modulated by high-frequency phonons in the device.

The fabrication process of GaAs/AlAs-based heterostructures by molecular beam epitaxy allows to control the layer thickness at the atomic scale. By carefully adjusting the layer thickness, it is possible to design structures with control of the acoustic field at ultrahigh frequencies with acoustic devices designed in the THz range [43], contrary to top-down fabrication techniques. GaAs/AlAs-based multilayered devices are thus of interest to control the confinement of ultrahigh-frequency acoustic phonons [44, 45]. Multilayered devices can be engineered to fabricate acoustic mirrors, Fabry-Perot cavities, filters, or acoustic potentials [41, 46, 47]. In the GHz range, the acoustic wavelength is in the order of a few tens to few hundred of nanometers which are comparable to optical wavelength in the near infrared (NIR) and infrared (IR) in semiconductors. GaAs/AlAs-based superlattices can then be designed to simultaneously control the confinement of photons in the near-infrared and phonons at a few tens of GHz, resulting in colocalized acoustic and optical fields which greatly enhances the interactions between both fields [48, 49]. At higher frequencies, the acoustic wavelength is in the order of a few nanometers. Semiconductor multilayered devices can be etched in micropillars leading to the three-dimensional confinement of light and sound [31], altering the acoustic and optical dispersion relations and density of states. The remarkable colocalization of light and sound can be used to design optophononic resonators working in the near-infrared at a few tens of GHz [50, 51]. These devices can also be integrated with quantum dots or quantum wells where phonons can be used as actuators for quantum emitters [52].

Topological acoustics was developed in recent years to mimic the topological behavior already studied in optics or electronics [53]. Structures demonstrating topological behavior have been engineered from the audible range to acoustic frequencies of a few hundred of GHz [31, 54, 55]. The robustness that topological devices show when they undergo local perturbations or fabrication defects [56] is desirable to investigate low-loss information transmission and phonon transport [57]. The application of topological principles to engineer the interactions with other excitations remains an open challenge in nanophononics.

Contrary to macroscopic acoustics, the absence of standard commercial transducers in the GHz to THz frequency range incites to develop optical techniques to experimentally access the acoustic modes. In the temporal domain, the development of picosecond acoustics permits the study of coherent acoustic phonons [58]. Whereas in the spectral domain, Brillouin and Raman scattering spectroscopies permit the study of incoherent

phonons important for general characterization and thermal management [59]. Brillouin scattering spectroscopy is a versatile and non-destructive technique used to probe the presence of acoustic modes. Over recent years, there have been important developments for Brillouin spectroscopy in a large variety of fields, such as: biology [60–62], acoustic metamaterials [59] or plasmonics [63]. Brillouin spectroscopy techniques were previously developed to explore confined acoustic modes in Fabry-Perot resonators at high frequency of a few hundreds of GHz [31, 64]. Despite promising results, these techniques restrict the access to lower frequencies in the few tens of GHz range in 3D optophononic Fabry-Perot cavities [50]. The confined acoustic modes in optophononic Fabry-Perot micropillar cavities were only evidenced using pump-probe experimental schemes [48, 65].
Standard Brillouin and Raman spectroscopy techniques [66–69] are optimized for fixed optical wavelengths, and therefore they are not adapted to optophononic cavities with tunable optical modes in a wide wavelength range and acoustic modes in a large frequency range. Further progress of the nanophononic field requires the development of experimental schemes to study 3D microresonators with frequencies in the tens of GHz range.

In this thesis we address current theoretical and experimental challenges in nanophononics. The first research line is the engineering of multilayered structures based on topology concepts to control the confinement of high-frequency acoustic phonons. We theoretically study the confinement of phonons in topological devices, mimicking the topological behavior already studied in macroscopic acoustics, optics or electronics [53].
The second research line consists of developing optical schemes to measure confined acoustic modes in multilayered microstructures. More specifically, it concerns advances of spontaneous Brillouin scattering experiments to access acoustic modes at $\sim$18 GHz in both planar and micropillar cavities.
The manuscript presents five chapters which range from theoretical concepts used in this thesis, to simulations and experimental results obtained during the thesis.

Chapter 1 addresses the fundamental concepts for phonon engineering in layered systems. We introduce one-dimensional superlattices, acoustic distributed Bragg reflectors and acoustic Fabry-Perot resonators working at high-frequency range. Finally, we address the colocalization of the optical and acoustic fields in multilayer systems made from GaAs and AlAs semiconductors.

In Chapter 2, we present optical characterization techniques to probe acoustic modes. In particular, we describe the process of Brillouin inelastic light scattering. We cover the different selection rules of Brillouin scattering which are of paramount importance. Then, we discuss the relaxation of some of these selection rules by engineering optical cavities. We also present the photoelastic model which we use for our calculations of Brillouin scattering spectra. In addition, we briefly introduce two other experimental techniques which are widely used to probe acoustic modes: the coherent generation and detection of phonons with pump-probe spectroscopy and noise measurement with Brownian motion experiments.

Chapter 3 focuses on the engineering of acoustic superlattices to generate acoustic confined states by band inversion. We address the relation between the topological properties of a superlattice and the symmetry of its modes. A variety of designs of topological interface states between two acoustic distributed Bragg reflectors are presented and analyzed. Moreover, we also use the colocalization of light and sound discussed in Chapter 1 to create optophononic topological resonators.

In Chapter 4, we present a Brillouin spectroscopy scheme to measure acoustic modes on planar optophononic GaAs/AlAs-based multilayered cavities at a few tens to a few hundreds of GHz. We exploit the optical dispersion relation of the Fabry-Perot cavity to spatially discriminate the signal from the reflected laser. We optimize the technique to measure confined acoustic modes at a frequency of a few tens of gigahertz.

In Chapter 5, we discuss an experimental Brillouin spectroscopy scheme based on polarization filtering to measure confined acoustic modes on optophononic micropillars. We introduce micropillars with an elliptical cross section to independently control the polarization of the reflected laser and of the Brillouin scattering signal. We theoretically and experimentally study the behavior of the Brillouin scattering signal as functions of different external parameters such as wavelength, micropillar ellipticity or incident polarization.

Finally, we end the manuscript with a general conclusion which summarizes the results obtained in this thesis and presents the perspectives of this work.

Chapter 1

Fundamentals of phonon engineering

The engineering of phonons at the nanoscale, i.e., nanophononics [1, 2, 4], is based on the design of nanostructures to control the propagation of phonons. In recent years, there have been important developments involving the control of acoustic phonons, such as: phonon lasing [26, 70], sensing [14], data storage [71, 72], heat control [17, 73], Brillouin laser [74], reaching the mechanical quantum ground state [75, 76].
Due to the similar wave behavior of light and sound, the concepts developed in optics for photonic crystals [77] were transposed to design phononic crystals. In the case of acoustic phonons, the acoustic dispersion relation can be altered by the modulation of acoustic impedances of the materials forming the structure. This leads to the creation of a variety of phononic crystals in one dimension [41, 70, 78, 79], two dimensions [73, 80, 81] and three dimensions [82].
In this work, we focus on one-dimensional superlattices. Multilayered systems are used to manipulate the propagation of acoustic nanowaves [41, 75, 83]. These devices work in the high-frequency range from a few GHz to a few THz. They can be grown by molecular beam epitaxy (MBE) with precise control of the layer thicknesses at the atomic scale, leading to flat interfaces. At high acoustic frequencies, in the tens to hundreds of GHz range, the system presents layer thicknesses in the range of a few nm to tens of nm.
In this chapter, we introduce GaAs/AlAs nanometric superlattices as phononic crystals in one-dimension. In section 1.1, we present the phononic band structure, and show the main elastic and optical properties used to engineer the optophononic resonators. In section 1.2, we introduce the building blocks to control the propagation of phonons in phononic crystals. Section 1.3 is devoted to presenting the acoustic Fabry-Perot cavity, as the nanoacoustic counterparts of the optical ones. Finally, in section 1.4, we discuss the coincidence in the optical and acoustic properties of GaAs and AlAs leading to simultaneous confinement of light and sound in one-dimensional heterostructures.

1.1 Phonon band structure

The devices studied in this thesis are formed by alternated layers of two different materials with contrasting acoustic and optical properties. GaAs and AlAs semiconductors have well-known optical, electronic and mechanical properties and are widely used in the optoelectronic industry. In addition, GaAs and AlAs present a small lattice mismatch.

Therefore, semiconductor samples with high quality can be readily fabricated with epitaxy techniques, making them relevant materials for one-dimensional nanophononic crystals. The optical and mechanical properties of GaAs and AlAs are displayed in table 1.1. The sound velocities are given for longitudinal acoustic phonons propagating in the (001) direction of the crystal.
Both semiconductors, GaAs and AlAs, have a zinc-blende crystal lattice which contains two atoms per unit cell, resulting in similar acoustic dispersion relations [84]. The dispersion relation of GaAs is represented in panel **a** of Fig.1.1. There are six branches which can be separated in two groups. The three branches at lower energy, corresponding to acoustic phonons, have an approximately linear dispersion relation crossing zero at the Γ point. For acoustic phonons, two neighbouring atoms move in the same direction, as shown in panel **c** of Fig.1.1, while the three upper branches correspond to optical phonons. In that case, there is a π phase shift between the motion of two consecutive atoms. Thus, they oscillate with opposite directions (panel **b** of Fig.1.1).
Both type of phonons can be classified into longitudinal or transverse phonons depending on the orientation of their wavevector $\vec{q}$. When the wavevector is perpendicular to the direction of propagation they are known as transverse phonons. On the contrary, when the wavevector is parallel to the direction of propagation they are called longitudinal phonons.

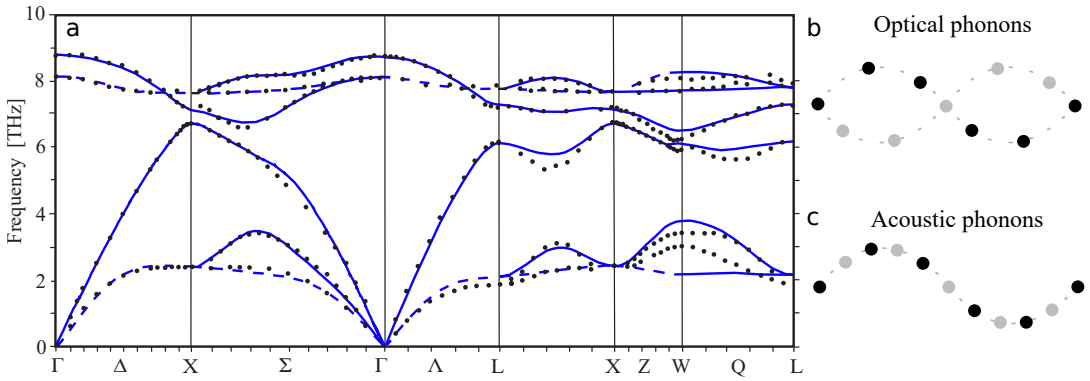

Figure 1.1: **a** Phononic band structure of GaAs. The dotted lines are experimental data points and the continuous lines are simulations. The three lower branches correspond to acoustic phonons while the three upper bands are optical phonons. The figure is reproduced from reference [84]. **b** and **c** represent the motion of atoms for transverse optical and acoustic phonons, respectively.

Material	Density (g.cm^{-3})	LA Sound velocity (m.s^{-1})	Refractive index
GaAs	5.35	4780	3.54
AlAs	3.77	5660	2.96

Table 1.1: Optical and mechanical properties of GaAs and AlAs [85–87]. LA stands for longitudinal acoustic.

1.2 One-dimensional phononic crystal

1.2.1 Acoustic superlattices

We consider an infinite structure composed of alternating layers of GaAs and AlAs (designated by the indices A and B), with thicknesses d_A and d_B. The unit cell of the superlattice is formed by a layer of each material, as represented in Fig.1.2, and has an associated thickness defined as $a = d_A + d_B$. The stacking of two materials into a superlattice causes the folding of the acoustic dispersion relation into the reduced Brillouin zone, which is defined by the new periodicity a [44, 88]. The growth direction is aligned along the (001) direction of the crystal, which corresponds to the z axis. The one-dimensional acoustic wave propagating along the z direction can be described with the mechanical wave equation:

$$\frac{\partial}{\partial t}\left(\rho(z)\frac{\partial u(z,t)}{\partial t}\right) = \frac{\partial}{\partial z}\left(C(z)\frac{\partial u(z,t)}{\partial z}\right), \tag{1.1}$$

where $u(z,t)$ is the displacement, $\rho(z)$ and $C(z)$ are the mass density and the stiffness constant along the (001) crystal direction, respectively.

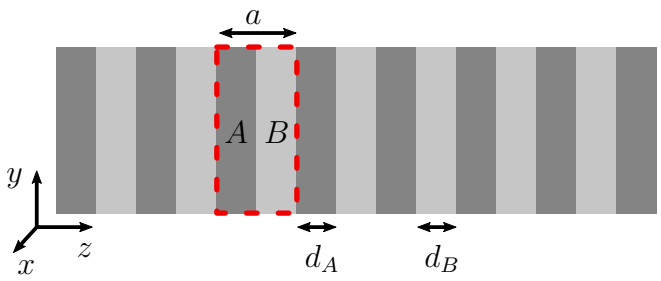

Figure 1.2: Schematic of a superlattice. The dark (light) grey represents material A (B). The red box identifies the unit cell. The acoustic wave propagates along the z direction.

If we consider concatenated layers made of materials A and B with homogeneous properties ($\rho(z)$ and $C(z)$) in each layer, the equation 1.1 in each layer can be rewritten as:

$$\rho_j \frac{\partial^2 u_j(z,t)}{\partial t^2} = C_j \frac{\partial^2 u_j(z,t)}{\partial z^2}, \tag{1.2}$$

where the index j indicates the considered layer, either A or B. In order to solve the wave equation, we need to consider the boundary conditions between two consecutive layers, related to the continuity of the displacement and stress at the interface between the layers, z_{int}. The conditions are:

$$u_A(z_{int}) = u_B(z_{int}) \tag{1.3}$$

and

$$C_A \frac{\partial u_A(z_{int},t)}{\partial z} = C_B \frac{\partial u_B(z_{int},t)}{\partial z}. \tag{1.4}$$

The solutions for an acoustic wave with wavevector $\vec{q}$ propagating in the z direction and obeying the selection rules are of the form:

$$u_j(z,t) = D_j e^{iq_j z} + E_j e^{-iq_j z}, \tag{1.5}$$

where D_j and E_j are constant coefficients. Taking into account the boundary conditions and using the Bloch theorem, we can determine the dispersion relation of phonons which links the wavevector q and the acoustic frequency ω [89]:

$$\cos(qa) = \cos\left(\omega\left(\frac{d_A}{v_A} + \frac{d_B}{v_B}\right)\right) - \frac{\epsilon^2}{2}\sin\left(\omega\frac{d_A}{v_A}\right)\sin\left(\omega\frac{d_B}{v_B}\right), \tag{1.6}$$

with

$$\epsilon = \frac{\left(\rho_B v_B - \rho_A v_A\right)^2}{\rho_B v_B \rho_A v_A}. \tag{1.7}$$

ϵ describes the acoustic modulation in the superlattice due to the change in acoustic impedance in the two materials, with ρ_A (ρ_B) and v_A (v_B) the mass density and the speed of sound for longitudinal acoustic phonons in material A (material B) respectively. In the case of III-V materials like GaAs and AlAs, the term $\epsilon^2/2$ is small (in the order of 10^{-2}). Therefore, the second term can be neglected in a first order approximation. This gives [89]:

$$\cos(qa) = \cos\left(\omega\left(\frac{d_A}{v_A} + \frac{d_B}{v_B}\right)\right). \tag{1.8}$$

We can also write:

$$qa = \pm\omega\frac{1}{v} + 2p\pi, \quad p \in \mathbb{Z} \tag{1.9}$$

where

$$v = \frac{v_A v_B}{(1-\beta)v_B + \beta v_A} \quad \text{with} \quad \beta = d_B/a. \tag{1.10}$$

Equation 1.9 corresponds to the folding of a linear dispersion line into the first Brillouin zone. The dispersion relation reaches the zone center and zone edge of the Brillouin zone at the energy Ω defined by:

$$\Omega = \frac{m\pi v}{a}, \quad m \in \mathbb{N}. \tag{1.11}$$

m refers to the number of times the acoustic dispersion relation crosses the zone edge or zone center of the Brillouin zone. Even (odd) numbers refer to the zone center (edge) of the Brillouin zone. In a second approximation, we can consider $\omega = \Omega + \Delta\Omega$, where Ω designates the central frequency of the bandgap and $\Delta\Omega$ designates the amplitude of the bandgap opening. The second term in equation 1.6 is responsible for the opening and closing of the bandgap. The amplitude of the bandgap is given by [86, 89]:

$$\Delta\Omega = \pm\epsilon\frac{v}{a}\sin\left(\frac{m\pi}{2}\frac{(1-\beta)v_B - \beta v_A}{(1-\beta)v_B + \beta v_A}\right) = \pm\epsilon\frac{v}{a}\sin\left(m\pi\delta\right), \tag{1.12}$$

where $\delta = d_B/a$ is the ratio of material B in the unit cell. Note that both the opening and the central frequency of the bandgap depend on the unit cell thickness a. Therefore, when the thickness of the unit cell increases, the bandgap amplitude expands and the central frequency reduces. In addition to the thickness of a, the bandgap amplitude also depends on the relative ratio of both materials in the unit cell δ. This effect will be discussed later on, in Chapter 3. Figure 1.3 displays the acoustic dispersion relation of acoustic phonons in an infinite GaAs/AlAs superlattice. The structure is designed to have the first bandgap centered around $f_0 = 18.6$ GHz, i.e. $\Omega_1 = 2\pi f_0$. We define the layer thicknesses as a quarter of the wavelength λ of the acoustic wave of frequency f_0 propagating with a velocity $v_{A/B}$ for both GaAs and AlAs $(\lambda/4, \lambda/4)$. In the case of GaAs, we obtain $d_{GaAs} = \lambda_{GaAs}/4 = f_0/(v_{GaAs} \times 4) = 63.61$ nm. For AlAs, this gives $d_{AlAs} = \lambda_{AlAs}/4 = f_0/(v_{AlAs} \times 4) = 75.95$ nm. The speeds of sound in GaAs and in AlAs are given in Table 1.1. We observe that the mode at the zone center of the Brillouin zone is closed, whereas the bandgaps at the edge of the Brillouin zone are open. For this design of the unit cell, the amplitude of the zone edge bandgaps is maximized. For the opened bandgaps, the dispersion relation flattens at the edge of the Brillouin zone, and the modes surrounding the bandgap have a group velocity $d\omega/dq = 0$. Note that the $(\lambda/4, \lambda/4)$ design is the one commonly used in photonics.

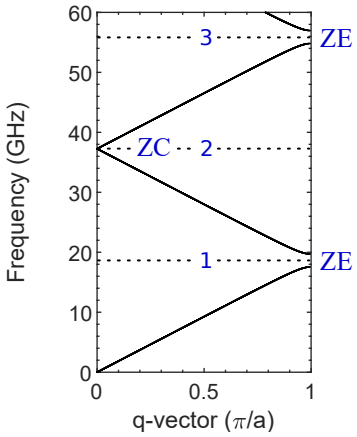

Figure 1.3: Dispersion relation of longitudinal acoustic phonons for an infinite superlattice made of GaAs/AlAs layers with thicknesses $(\lambda/4, \lambda/4)$ designed at a frequency $f_0 \approx 18.6$ GHz. The dashed lines indicate the central frequency of each bandgap. The numbers designate the bandgap. ZE and ZC indicate the zone edge and zone center of the Brillouin zone, respectively. The second bandgap, located at the zone center, is closed, whereas the bandgaps at the zone edge are open.

1.2.2 Acoustic distributed Bragg reflectors

Acoustic distributed Bragg reflectors (DBRs) are the finite version of infinite acoustic superlattices. Contrary to the latter, acoustic DBRs can be experimentally studied. In this section, we consider an acoustic DBR embedded in bulk GaAs medium, as represented in the schematic of Fig.1.4.

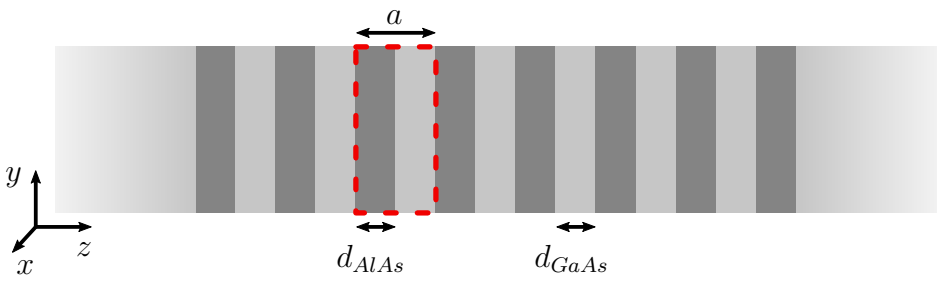

Figure 1.4: Schematic of a distributed Bragg reflector. The layer of AlAs and GaAs are embedded in a GaAs substrate.

We consider a longitudinal acoustic wave propagating in the z direction. Due to different acoustic impedances Z between GaAs and AlAs, the acoustic wave is separated in two fields composed of a reflected and a transmitted part at each interface between two consecutive layers. The different reflected fields add up in constructive or destructive waves, likewise for the transmitted fields. We simulate the acoustic properties of the distributed Bragg reflector using the transfer matrix formalism in one dimension to solve the 1D wave equation and boundary conditions [86]. Figure 1.5**a** displays the acoustic reflectivity spectrum calculated for a DBR composed of 24 pairs of GaAs/AlAs layers with thicknesses $(\lambda/4, \lambda/4)$, designed for a frequency $f_0 = 18.6$ GHz. The DBR presented here is the finite counterpart of the superlattice whose band diagram is represented in Fig.1.3. The spectrum shows high reflectivity regions at the positions of the open bandgaps, centered around 18.6 GHz and 55.8 GHz. The bandwidth of the high reflectivity region is equal to the bandwidth of the bandgap and is ≈ 2.4 GHz. The high reflectivity regions are due to constructive interferences in the reflected field. The maximum of reflectivity depends on the ratio between the acoustic impedances $Z = Z_{AlAs}/Z_{GaAs}$ and on the number of periods constituting the DBR. The reflectivity increases with the number of periods.

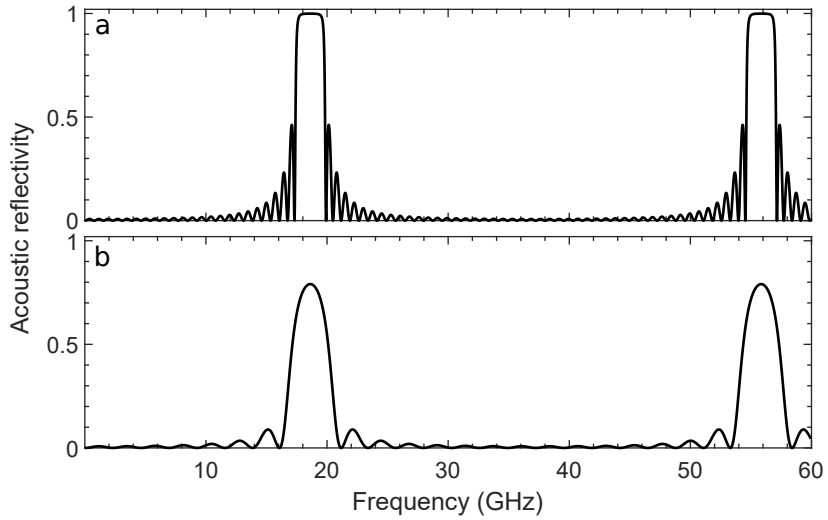

Figure 1.5: Calculated acoustic reflectivity for a $(\lambda/4, \lambda/4)$ GaAs/AlAs DBR formed by **a** 24 periods and **b** 8 periods, embedded in GaAs substrate.

As a comparison to the previous DBR, we simulated the acoustic reflectivity spectrum for a DBR formed by only 8 periods designed at the same frequency f_0, and display the result in panel **b** of Fig.1.5. Similarly to panel **a** of Fig.1.5, we observe high reflectivity regions at the positions of the bandgaps with a maximum of reflectivity in the center of the bandgaps. In the case displayed here, due to the reduced number of layers, the maximum of reflectivity does not reach 1. Whereas for a higher number of periods, the DBR becomes an almost perfect mirror at the bandgap frequency range. The number of oscillations surrounding the high reflectivity regions, called Bragg oscillations, also depend on the number of periods.

1.3 Phononic Fabry-Perot cavity

By introducing a defect, e.g., an extra layer with a different thickness, between two distributed Bragg reflectors, a confined acoustic mode appears in the bandgap zone. Here, we concatenate two DBRs with a GaAs spacer layer in between to form an acoustic Fabry-Perot resonator [46, 90, 91]. The spacer thickness between the two mirrors verifies [85]:

$$d_{spacer} = p\frac{f_0}{2v_{GaAs}}, \quad p \in \mathbb{N}, \tag{1.13}$$

where v_{GaAs} is the speed of sound in GaAs and f_0 is the acoustic frequency at which the DBRs are designed. In that case, the confined acoustic mode is pinned at the center of the bandgap. Inside the spacer, the acoustic field at the frequency f_0 forms a standing wave.

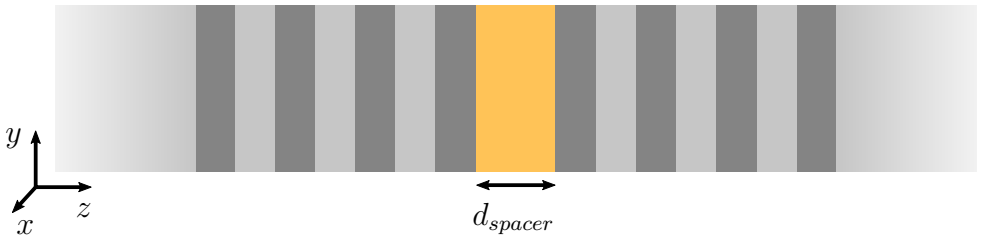

Figure 1.6: Schematic of a Fabry-Perot cavity embedded in a GaAs medium. The spacer identified in orange is made of GaAs.

Figure 1.7 displays reflectivity spectra for two Fabry-perot resonators made from the DBRs whose reflectivities are shown in Fig.1.5. Panels **a** and **b** of Fig.1.7 show calculated acoustic reflectivity spectra for two Fabry-Perot resonators formed by two DBRs of 24 and 8 $(\lambda/4, \lambda/4)$ GaAs/AlAs periods embedding a $\lambda/2$ GaAs spacer ($p = 1$), respectively. The confined acoustic mode appears as a dip in the center of the high-reflectivity region. The amplitude of the acoustic displacement $|u(z)|^2$ of the confined mode is represented in panels **a** and **b** of Fig.1.8 for both designs of Fabry-Perot resonators. The field is calculated by considering an incident wave propagating from the substrate. It is then normalized by the amplitude of the acoustic displacement in the substrate to account for the thermal bath. The complete multilayer structure is represented on top of the

spatial profile. For the two structures, the acoustic displacement presents a maximum amplitude in the spacer layer, with a minimum of displacement at the center of the spacer. The envelope of the acoustic displacement field exponentially decays inside the DBRs. We observe that the enhancement of the field inside the structure is different for both Fabry-Perot resonators.

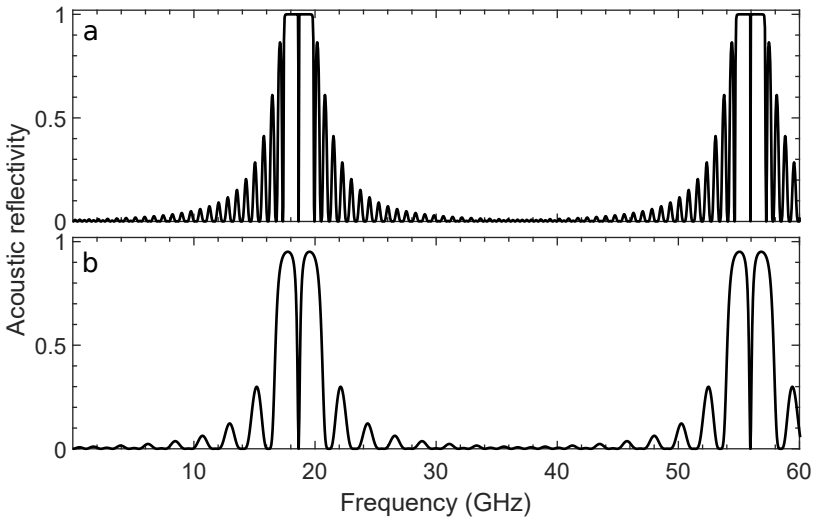

Figure 1.7: Calculated acoustic reflectivity of a Fabry-Perot cavity made of two (λ_4, λ_4) GaAs/AlAs DBRs with **a** 24, **b** 8 periods and a $\lambda/2$ GaAs spacer.

The enhancement of the field inside the structure is scaled with the mechanical quality factor Q_m. The mechanical quality factor quantifies the field confinement strength. It can be obtained from the reflectivity spectrum: $Q_m = f_0/\Gamma$, where Γ is the full width at half maximum of the Lorentzian acoustic mode. The linewidth of the mode is linked to the energy lost per cycle of oscillation of the field inside the cavity. The mechanical quality factor of the first Fabry-Perot resonator (24 periods in each DBR) is $Q_m = 24063$, whereas $Q_m = 73$ in the case of 8 periods in each DBR. On panels **a** and **b** of Fig.1.7, the difference in linewidth of the acoustic mode between the two designs is clearly visible: the mode for the Fabry-Perot with the lowest number of layers is broader.
The quality factor directly depends on the number of periods in each DBR. Therefore, when the number of layers in each DBR is increased, the confinement strength increases, thus the mechanical quality factor increases.

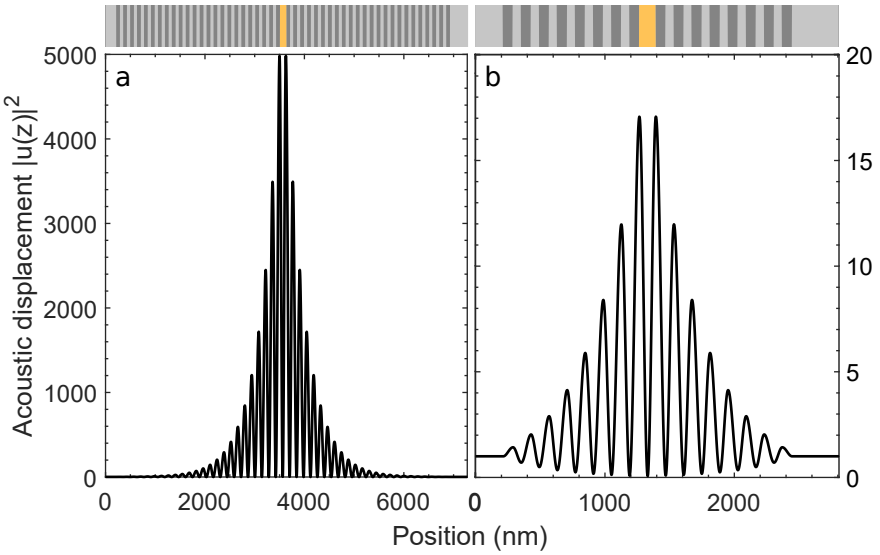

Figure 1.8: Calculated acoustic displacement of the confined acoustic mode. The Fabry-Perot cavity is made of two $(\lambda/4, \lambda/4)$ GaAs/AlAs DBRs with **a** 24, **b** 8 periods and a $\lambda/2$ GaAs spacer. The complete structure is plotted on top of the acoustic displacement.

1.4 Simultaneous confinement of light and sound

1.4.1 One-dimensional colocalization

In multilayered structures, the behavior of the optical field is similar to the one of the acoustic field, since both respond to 1D wave equations [48, 92]. The acoustic wave propagation at the interface between two materials is governed by the difference in speed of sound and acoustic impedances. Likewise, the behavior of the electromagnetic wave at the interface is constrained by the different speed of light and optical indices of refraction in the two materials. GaAs and AlAs materials present two "magic" coincidences in their properties: the ratio of speeds of sound and speeds of light in the materials are equal, as well as the ratio of the optical and acoustic impedances [48, 49].

$$\frac{n_{GaAs}}{n_{AlAs}} \approx \frac{Z_{GaAs}}{Z_{AlAs}} = 1.2, \tag{1.14}$$

$$\frac{c_{GaAs}}{c_{AlAs}} \approx \frac{v_{GaAs}}{v_{AlAs}} = 0.84, \tag{1.15}$$

where $Z_{GaAs} = \rho_{GaAs} v_{GaAs}$ ($Z_{AlAs} = \rho_{AlAs} v_{AlAs}$) is the acoustic impedance in GaAs (AlAs), n_{GaAs} (n_{AlAs}) is the optical index of GaAs (AlAs), c_{GaAs} and v_{GaAs} are the speeds of light and sound in GaAs and c_{AlAs} and v_{AlAs} are the speeds of light and sound in AlAs. Thus, an acoustic Fabry-Perot resonator designed to have a confined mode f_0^{ac} at tens of GHz will also confine an optical mode in the near-infrared range at a frequency f_0^{opt} [48].

In an acoustic multilayered structure, we can define the thickness d_A of the layer A as a function of a given acoustic frequency f_0^{ac} and the speed of sound in the material

v_A. Likewise, the thickness of the layer can be expressed as a function of the optical frequency f_0^{opt} and the speed of light in the matrial c_A. Thus, we define the thickness of the material A as [92, 93]:

$$\begin{aligned} d_A &= \alpha_A \lambda_A^{ac} = \alpha_A \frac{v_A}{f_0^{ac}} \quad \text{and} \\ d_A &= \beta_A \lambda_A^{opt} = \beta_A \frac{c_A}{f_0^{opt}}, \end{aligned} \tag{1.16}$$

where α_A and β_A are coefficients. We consider the particular optical frequency $f_0^{opt} = f_0^{ac}\frac{c_A}{v_A}$. In the material A, we obtain that

$$\lambda_A^{ac} = \lambda_A^{opt}. \tag{1.17}$$

If we consider the same frequencies in material B, we have:

$$\lambda_B^{ac} = \frac{v_B}{f_0^{ac}} \quad \text{and} \tag{1.18a}$$

$$\lambda_B^{opt} = \frac{c_B}{f_0^{opt}}. \tag{1.18b}$$

By replacing f_0^{opt} in equation 1.18b, the optical wavelength in the material B becomes:

$$\lambda_B^{opt} = \lambda_A^{ac}\frac{c_B}{c_A} = \lambda_B^{ac}\left(\frac{v_A}{v_B}\frac{c_B}{c_A}\right). \tag{1.19}$$

For the particular case of GaAs and AlAs, equation 1.15 is verified. As a consequence, equation 1.19 simplifies into:

$$\lambda_B^{opt} = \lambda_B^{ac}. \tag{1.20}$$

From the results obtained in equations 1.17 and 1.20, we conclude that a $(\lambda/4, \lambda/4)$ GaAs/AlAs acoustic Fabry-Perot resonator with a $\lambda/2$ spacer designed to confine acoustic phonons at a frequency f_0^{ac} also confines photons at the same wavelength and at a frequency f_0^{opt}.
Note that these coincidences are not present in every set of materials. For example, it does not exist for Si and Ge. However, similar coincidences in the material properties can also be found for SiO_2/TiO_2 or $InP/Ga_{0.53}In_{0.47}$ [51].
We consider the design for the acoustic Fabry-Perot resonator defined in section 1.3. The confined acoustic mode is at $f_0^{ac} \approx 18.6$ GHz. This corresponds to a near-infrared confined optical mode at $f_0^{opt} \approx 333$ THz (with a wavelength ≈ 900 nm). Panels **a** and **b** of Fig.1.9 display the confined optical mode at 900 nm for two Fabry-Perot cavities with 24 and 8 $(\lambda/4, \lambda/4)$ GaAs/AlAs periods, respectively.

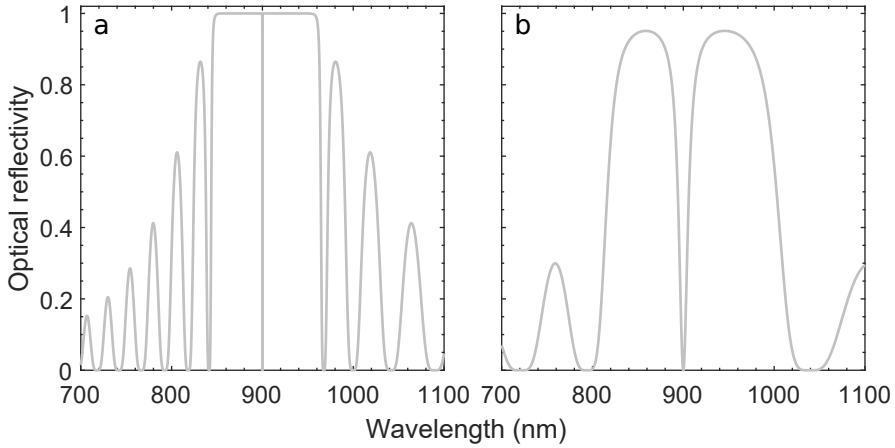

Figure 1.9: Calculated optical reflectivity of a Fabry-Perot cavity made of two $(\lambda/4, \lambda/4)$ GaAs/AlAs DBRs with **a** 24, **b** 8 periods and a $\lambda/2$ GaAs spacer. The designs of the structures are the same as in previous section.

The optical quality factor depends on the ratio between the optical indices of refraction and on the number of periods constituting the DBRs, analogous to the acoustic counterpart. Moreover, thanks to the relation between the optical and acoustic impedances expressed in equation 1.14, the optical and acoustic reflectivity contrasts are identical. As a result, the optical and acoustic quality factors for a Fabry-Perot cavity embedded in GaAs are equal.

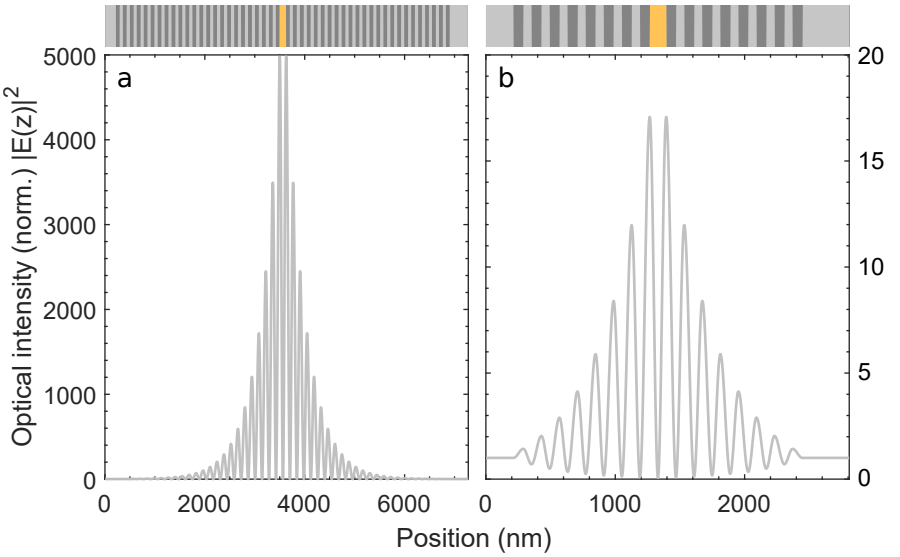

Figure 1.10: Calculated optical field of the confined optical mode. The Fabry-Perot cavity is made of two $(\lambda/4, \lambda/4)$ GaAs/AlAs DBRs with **a** 24, **b** 8 periods and a $\lambda/2$ GaAs spacer. The complete structure is plotted on top of the intensity profile.

Panels **a** and **b** of Fig.1.10 plot the intensity of the electromagnetic field $|E(z)|^2$ of the confined optical mode at f_0^{opt} for the same two Fabry-Perot resonators presented before. The optical field overlaps perfectly with the acoustic displacement field. That is, the enhancement of the optical field is maximal in the spacer, with a minimum at

the center of the spacer layer, and decays in the DBRs. Moreover, the maximum field intensity in the spacer is equal for both the optical and acoustic fields.
Note that differences arise when the system is in experimental conditions, i.e., when one side of the structure is in contact with air or vacuum. The air or vacuum acts as a perfect mirror for acoustic waves. To compensate for the change in boundary conditions on both sides of the optical Fabry-Perot resonator, the number of periods in the DBRs is unbalanced. The DBR in contact with the air (or vacuum) contains less pairs to account for the difference in optical reflectivity. Despite the asymmetry of the Fabry-Perot cavity, there is still colocalization of the optical and acoustic fields in the structure.

1.5 Conclusions

In this chapter, we introduced the concepts which permit the control of the propagation of acoustic waves in the GHz range in multilayered systems. First, we introduced the acoustic band diagram of superlattices. We showed that we can engineer the bandgap in superlattices to fabricate acoustic distributed Bragg reflectors and Fabry-Perot cavities to work at a given frequency. Moreover, we have seen that due to a coincidence by nature in GaAs/AlAs, we can simultaneously confine light and sound in Fabry-Perot resonators at a wavelength around 900 nm and an acoustic frequency around 18 GHz. These concepts are the foundation of the acoustic resonators which we will present in Chapter 3. In Chapter 5, we present Brillouin spectroscopy measurements on micropillars fabricated from optophononic Fabry-Perot resonators described in this chapter.
The multilayered devices discussed in this thesis have typical resonant acoustic frequencies at $\sim$18 GHz. These devices simultaneously present an optical mode at 900 nm with optical quality factor ranging from 2300 to 11000. We study an acoustic resonator with layer thickness of few nanometers confining phonons at 300 GHz.

Chapter 2

Optical measurement of acoustic phonons

Contrary to what happens in audible acoustics, in the GHz to THz range there are no standard and commercial acoustic transducers that would permit the generation and detection of acoustic waves. We mainly rely on optical schemes for the excitation and detection of phonons. Several techniques enable the study of acoustic waves either in the spectral domain or in the time domain. In this chapter, we present spectroscopy techniques to evidence the presence of phonons. We introduce the mechanisms involved in inelastic Brillouin scattering. We describe the process with a microscopic approach associated to the interaction between different systems, and a macroscopic approach related to the photoelastic effect. Then, we discuss the resulting geometric and polarization selection rules, and we show that by introducing an optical cavity the scattered signal can be modified. Finally, we introduce two other techniques to measure acoustic vibrations. In the time domain, we present the coherent generation and detection of acoustic phonons in a pump-probe scheme. In the spectral domain, we discuss noise measurements or Brownian motion characterization, which are standard in cavity optomechanics.

2.1 Brillouin/Raman scattering

When light propagates through a medium it can either be transmitted, reflected or absorbed. However, a small fraction of the light is scattered by the inhomogeneities in the material. Atomic displacement due to phonons propagating in the medium is also a source of scattering of the light [84, 94]. On one hand, the light can be elastically scattered (without change in frequency) in what is called Rayleigh scattering. On the other hand, the light can be inelastically scattered with a gain or loss of energy in Brillouin/Raman Stokes or anti-Stokes scattering processes. The difference between Brillouin and Raman scattering is discussed in section 2.1.1.

2.1.1 Brillouin scattering by acoustic phonons

Brillouin scattering is the inelastic scattering of light due to acoustic phonons, while Raman scattering is the inelastic scattering of light due to optical phonons. The main differences between Brillouin and Raman scattering processes come from the distinction between the dispersion relations of the acoustic and optical phonons, and on the frequency range associated to each of them. The dispersion relation of optical phonons is rather flat (see Fig.1.1**a**), and their energies do not change much with the wavevector. The Raman scattering spectrum presents a large spectral shift in the tens of THz range leading to specific experimental tools. On the other hand, the acoustic phonon dispersion is linear with the acoustic wavevector q [84]:

$$\omega_{ac} = v_{ac} q, \tag{2.1}$$

where ω_{ac} and v_{ac} are the acoustic angular frequency and the velocity of sound in the medium. Typically, a Brillouin spectroscopy spectrum presents a short spectral shift with phonon frequencies $\leq \sim$12 GHz. In this thesis, we discuss Brillouin scattering involving high-frequency acoustic phonons. Due to the particular frequency range, above 10 GHz and much lower than optical phonon frequencies, we will develop experimental tools based on Raman spectrometer adapted to measure acoustic phonons.

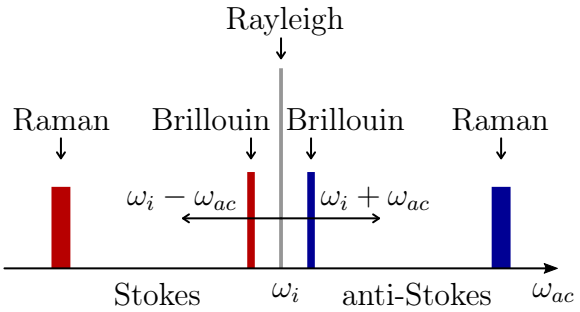

Figure 2.1: Schematic spectrum of the different scattered optical fields. ω_i is the frequency of the incident optical field and ω_{ac} is the acoustic frequency.

2.1.2 Microscopic description of the Brillouin scattering process

The microscopic description of spontaneous Brillouin scattering considers the different steps and systems involved in the process. Three systems are concerned: the incident and scattered photons, the absorbed or emitted phonons and the semiconductor electron-hole pairs. Since the interactions in the scattering process are weak, we can use the perturbation theory to obtain the scattering probability [85, 94]. Stokes (anti-Stokes) scattering is a three steps process whhich can be described as follows:

1. The incident photon excites the electron of the semiconductor from an initial state $|i\rangle$ to an intermediate state $|n\rangle$ and creates an electron-hole pair, an exciton (grey arrows in Fig.2.2). This interaction is described by an electron-radiation Hamiltonian $\hat{H}_{e-R}$.

2. The exciton is scattered from the state $|n\rangle$ to another state $|n'\rangle$ due to the interaction with a phonon. This interaction is dictated by the electron-phonon interaction

Hamiltonian $\hat{H}_{e-latt}$. In the case of Stokes scattering, the energy of the state $|n'\rangle$ is lower than the energy of the state $|n\rangle$, and conversely for anti-Stokes scattering (black arrows in Fig.2.2).

3. The exciton recombines by emitting a scattered photon. Stokes (anti-Stokes) scattered photon is represented by the red (blue) arrow in Fig.2.2, respectively. This interaction is described by an electron-radiation Hamiltonian $\hat{H}_{e-R}$.

Note that, during the process, the electron stays unchanged. The energy and wavevector are preserved in the overall process. However, it is not the case for each step independently.

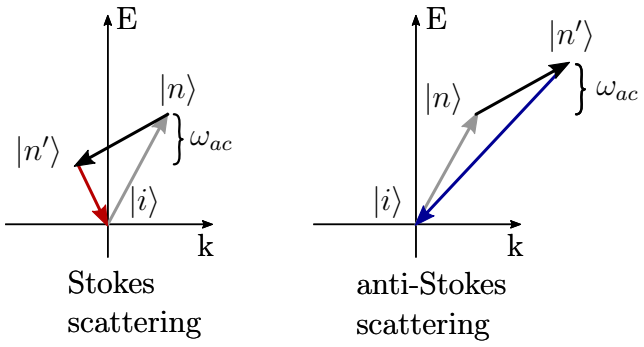

Figure 2.2: Diagram of the Brillouin scattering processes. The grey arrows are the excitations path of the photons.The black arrows are the absorption or emission of a phonon. The red and blue arrows are the de-excitation paths of the photons in Stokes and anti-Stokes Brillouin scattering, respectively.

The three steps can be transferred into a scattering probability using the perturbation theory. All the steps are virtual processes and do not involve real transitions. The scattering probability is [84, 85]:

$$P_s(\omega_s) = \frac{2\pi}{\hbar}\left|\sum_{n,n'}\frac{\langle i|\hat{H}_{e-R}|n'\rangle\langle n'|\hat{H}_{e-latt}|n\rangle\langle n|\hat{H}_{e-R}|i\rangle}{[\hbar\omega_i-(E_n-E_i)][\hbar\omega_i-\hbar\omega_{ac}-(E_{n'}-E_i)]}\right|^2 \times \delta(\hbar\omega_i-\hbar\omega_{ac}-\hbar\omega_s) \tag{2.2}$$

Each successive interaction explained above is described by a term in the numerator. The delta function represents the energy conservation. The denominator contains the energy of the scattered and incident photons. The electron-radiation Hamiltonian $\hat{H}_{e-R}$ is defined as [84]:

$$\hat{H}_{e-R} = \frac{e}{mc}\vec{A}\cdot\vec{p} \tag{2.3}$$

where e, m and $\vec{p}$ are the charge, the mass and the momentum operator of the electron, respectively. c is the speed of light and $\vec{A}$ is the vector potential of the electromagnetic field.
The electron-phonon interaction can be assumed to be a deformation potential. The electron energy responds instantaneously to the lattice vibration. For longitudinal acoustic

phonons with a small wavevector, the electron-phonon interaction Hamiltonian $\hat{H}_{e-latt}$ can be expressed as:

$$\hat{H}_{e-latt,LA} = a_{nk}\left(\vec{q}\cdot\delta\vec{R}\right) \tag{2.4}$$

where a_{nk} is the volume deformation and $\vec{q}$ is the phonon wavevector. $\delta\vec{R}$ depends on the phonon creation and annihilation operators. Stokes is considered to be a creation process and anti-Stokes an annihilation process.

2.1.3 The photoelastic model

The inelastic scattering induced by acoustic phonons is mediated through the photoelastic effect [84, 95, 96]. The propagation of an acoustic wave in the z direction in a medium is described by the equation of motion:

$$\rho\frac{\partial^2 u_z}{\partial t^2} - C\frac{\partial^2 u_z}{\partial z^2} = 0 \tag{2.5}$$

The acoustic wave causes the deformation of the medium which is expressed through the strain tensor:

$$\eta_{ij} = \left(\frac{\partial u_i}{\partial z_j} + \frac{\partial u_j}{\partial z_i}\right) \tag{2.6}$$

The strain tensor is responsible for variations in the dielectric tensor:

$$\Delta(\epsilon^{-1})_{ij} = \sum_{kl} p_{ijkl}\eta_{kl}\ , \tag{2.7}$$

where p_{ijkl} is the photoelastic tensor. The photoelastic tensor is related to the electric susceptibility of the material by:

$$p = \frac{\partial\chi}{\partial\eta}. \tag{2.8}$$

The strain is linked to the optical field through the refractive index of the medium. For materials with cubic crystal structure such as GaAs and AlAs, we can write:

$$\Delta(\epsilon)_{ij} = -n^4\sum_{kl} p_{ijkl}\eta_{kl} \tag{2.9}$$

If we consider an acoustic wave propagating along the growth direction z of a GaAs/AlAs superlattice, the photoelastic tensor can be simplified to $p(z) = -n^4 p_{1133}(z)$. We can write the polarization components at the source of Stokes and anti-Stokes scattering, respectively [95]:

$$\begin{aligned} P_S(z,t) &= p(z)\frac{\partial u^\star(z)}{\partial z}E_i(z,t) \\ P_{aS}(z,t) &= p(z)\frac{\partial u(z)}{\partial z}E_i(z,t) \end{aligned} \tag{2.10}$$

The Brillouin cross-section is obtained by integrating the induced polarization components. It corresponds to the probability to scatter photons due to the presence of phonons in the medium [85, 89, 95]:

$$\sigma(\omega) \propto \left| \int E_i(z) p(z) \frac{\partial u(\omega, z)}{\partial z} E_s^\star(z) dz \right|^2 \tag{2.11}$$

Equation 2.11 gives the intensity of the scattered Brillouin signal. It depends on the overlap between the incident optical field, the scattered optical field, the strain induced by the acoustic wave in the medium and the photoelastic constant in the material. Note that in the case of a Fabry-Perot cavity simultanously confining photons and phonons this cross-section is enhanced due to the overlap of both fields.

Polarization selection rules

The intensity of the scattered beam is dependent on the polarization of the incident and scattered beams. If we define the polarization of the incident beam $\vec{e}_i$, the intensity of the scattered field depends on its polarization $\vec{e}_s$ and is proportional to [96]:

$$I_S \propto |\vec{e}_s \cdot \Delta\epsilon \cdot \vec{e}_i|^2 . \tag{2.12}$$

Thus, the Brillouin polarization selection rules depend on the dielectric tensor of the material. By combining equations 2.8 and 2.9, we obtain that the dielectric tensor depends on the electric susceptibility. Therefore, the polarization selection rules of Brillouin scattering are identical to those of Raman scattering. The polarization selection rules of Raman scattering in GaAs and AlAs is described in Appendix A. For the case of longitudinal acoustic phonons in an isotropic material, the polarization is preserved for Brillouin scattering. That is the scattered light and the reflected laser have parallel polarizations [84].

2.1.4 Scattering geometry selection rules

We consider an optical wave propagating in the z direction in a multilayered system. The electric field can be described as a plane wave: $E \propto e^{ik_z z}$. At high acoustic frequencies, the energy of phonons (∼0.1 meV) is small compared to the energy of photons (∼1.34 eV). Therefore we can approximate $|k_i| \approx |k_s|$ for the incident and scattered fields, which allows two scattering geometries, represented in Fig.2.3. Forward scattering corresponds to the scattered light propagating in the same direction as the incident field, and backward scattering to both fields propagating in opposite directions.

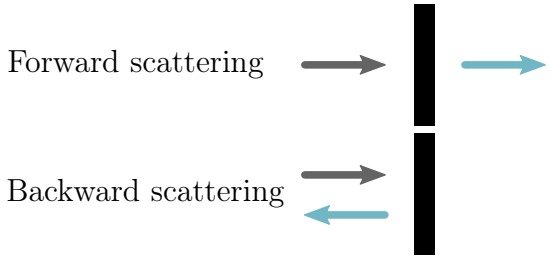

Figure 2.3: Schematic of forward and backward scattering geometries. The grey and blue arrows figure the incident laser and scattered field, respectively.

In forward scattering geometry, $k_i = k_s$, resulting in $q \approx 0$. This gives the Brillouin cross-section:

$$\sigma(\omega) \propto \left| \int p(z) \frac{\partial u(\omega, z)}{\partial t} dz \right|^2 \tag{2.13}$$

In the case of backward scattering: $k_i = -k_s$, resulting in $q \approx 2k_i$. The Brillouin cross-section is:

$$\sigma(\omega) \propto \left| \int e^{2ik_z z} p(z) \frac{\partial u(\omega, z)}{\partial t} dz \right|^2 \tag{2.14}$$

2.2 Enhancement of the Brillouin scattering intensity

There are two different mechanisms which can enhance Brillouin scattering. Electronic resonance, when the energy of the scattered signal or of the incident beam is resonant with the electronic transition of the material; and optical enhancement, when the scattered signal and/or the the incident beam is amplified by the optical density of states [97]. In the adiabatic approximation, both enhancements can be treated separately since the processes are independent [98].

2.2.1 Optical resonant Brillouin scattering

The enhancement of light in microcavities can enhance Brillouin scattering. In a planar optical microcavity, the spacer thickness is $d_{spacer} = p\frac{\lambda_0}{2n_{spacer}}$, with p an integer number. The wavenumber $\vec{k}$ of the optical mode in the cavity can be decomposed as $\vec{k} = \vec{k}_z + \vec{k}_{//}$ where $\vec{k}_{//}$ is the in-plane component and $\vec{k}_z$ is the component normal to the surface, see Fig.2.4. The optical dispersion relation of the cavity follows:

$$\omega = \frac{c}{n_{spacer}} \sqrt{k_z^2 + k_{//}^2}\,, \tag{2.15}$$

where c is the speed of light in vacuum and n_{spacer} is the refractive index of the spacer. The $\vec{k}_z$ component complies with:

$$k_z = p\frac{\pi}{n_{spacer} d_{spacer}}\,, \tag{2.16}$$

where p is an integer number and d_{spacer} is the thickness of the spacer. Therefore, the resonance is achieved for a fixed k_z. The dispersion relation only depends on $k_{//}$:

$$\omega(k_{//}) = \frac{c}{n_{spacer}} \sqrt{\left(p\frac{\pi}{n_{spacer} d_{spacer}}\right)^2 + k_{//}^2}\,. \tag{2.17}$$

Figure 2.4 shows the optical dispersion for a Fabry-Perot cavity with k_z kept constant and varying $k_{//}$. When changing $k_{//}$, and thus the incident angle, the overall optical wavevector is modified, causing an increase in the resonant frequency.

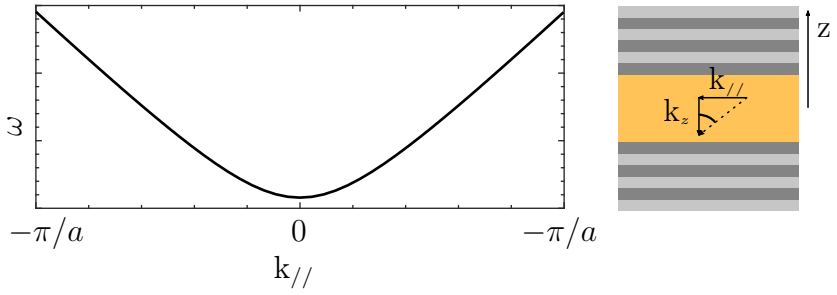

Figure 2.4: Dispersion relation of an optical cavity with a $\lambda/2$ spacer as a function of the in-plane wavevector $\vec{k}_{//}$. Schematic of the different components of $\vec{k}$ in a Fabry-Perot cavity.

2.2.2 Double optical resonance

The objective of the double optical resonance is to simultaneously enhance the incident and the scattered fields by taking advantage of the optical dispersion of the planar cavity. In a planar optical microcavity, the incident and scattered fields can be described by a standing wave inside the spacer, with their electric field written as [85]: $E_{i/s} = A_{i/s}\left(e^{2ik_{z,i/s}z} + e^{-2ik_{z,i/s}z}\right)$, where $A_{i/s}$ is the enhancement factor of the intensity of the incident/scattered field at the center of the cavity, respectively. Thus, the enhancement of the Brillouin scattering intensity is maximal when both the incident and scattered beams are tuned in resonance with an optical cavity, in double optical resonance (DOR). Under double optical resonance both fields are almost equal: $E_i = E_s = A\left(e^{2ik_z z} + e^{-2ik_z z}\right)$ [46]. Therefore, we can write:

$$E_i E_s^{\star} = |E(z)|^2 = A^2\left(2 + e^{2ik_z z} + e^{-2ik_z z}\right) \tag{2.18}$$

The enhancement of the field inside the cavity is quantified by the optical Q-factor of the cavity, giving $A \propto Q$ [99]. Consequently, by combining equations 2.11 and 2.18, we obtain:

$$\sigma(\omega) \propto Q^2 \times \left| \int \left(2 + e^{2ik_z z} + e^{-2ik_z z}\right) p(z) \frac{\partial u(\omega, z)}{\partial t} dz \right|^2 . \tag{2.19}$$

Equation 2.19 can be expressed as:

$$\sigma(\omega) \propto \left| \int |E(z)|^2 p(z) \frac{\partial u(\omega, z)}{\partial t} dz \right|^2 . \tag{2.20}$$

Let us consider the Stokes scattering component. In that case, $\omega_S = \omega_i - \omega_{ac}$ and $\vec{k}_S = \vec{k}_i - \vec{q}$. According to equation 2.17, the energy of the resonant field depends on the wavevector $k_{//}$. Due to the energy difference between the scattered and incident photons, both fields are resonant with the optical cavity at different $k_{//}$. Figure 2.5**a** shows the optical dispersion relation of a Fabry-Perot cavity. The red and blue points mark the frequency of the incident and scattered beams separated by the acoustic frequency. Both fields are resonant with distinct wavevectors. We suppose that the scattered signal is resonant at normal incidence (i.e. $k_{//} = 0$). To experimentally achieve the double optical resonance condition, the angle of incidence of the incoming beam can be tuned so the

energies of the scattered and incident photons are resonant with the optical cavity [97, 99, 100]. In the simulations we achieve the DOR condition by considering that $E_i \sim E_s$.

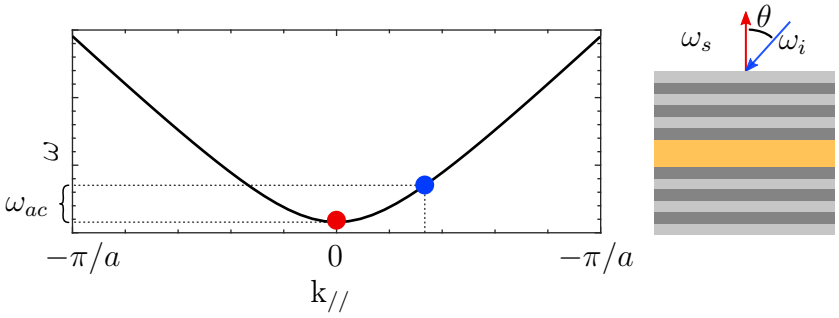

Figure 2.5: Dispersion relation of an optical cavity with a $\lambda/2$ spacer as a function of the in-plane wavevector $\vec{k}_{//}$. The incident (blue) and scattered (red) frequencies are marked on the dispersion relation. Schematic of the double optical resonance geometry in the case of Stokes scattering.

The experimental configuration allowing to reach the double optical resonance condition for Stokes scattering is shown in Fig.2.5**b**. The incident and scattered beams have an angular shift which depends on the energy detuning. The incident beam, represented by the blue arrow, enters the sample with an angle of incidence θ compared to the normal of the sample, while the scattered beam is collected at normal incidence. Note that, due to the energy conservation, Stokes and anti-Stokes are resonant with the optical cavity with nonidentical energies. Therefore, the conditions to achieve the double optical resonance will differ in both cases. The detuning angle between the incident and scattered frequencies is given by [100]:

$$\theta = n_{eff} \arccos\left(\omega_i/\omega_s\right), \tag{2.21}$$

where n_{eff} is the effective optical index of refraction. The implementation of an experimental technique benefiting from the double optical resonance is presented in more detail in Chapter 4.

2.2.3 Relaxation of backscattering selection rules

Considering a stationary electromagnetic field in a cavity, the cross-section of the optical enhanced Brillouin scattering $\sigma(\omega)$ (equation 2.19) can be separated into two components [98]:

$$\sigma(\omega) \propto \sigma_{FS} + \sigma_{BS} \tag{2.22}$$

with

$$\begin{aligned} \sigma_{FS} &= Q^2 \times \left| \int 2p(z) \frac{\partial u(\omega, z)}{\partial t} dz \right|^2 \quad \text{and} \\ \sigma_{BS} &= Q^2 \times \left| \int \left(e^{2ik_z z} + e^{-2ik_z z}\right) p(z) \frac{\partial u(\omega, z)}{\partial t} dz \right|^2 . \end{aligned} \tag{2.23}$$

The first term σ_{FS} is a constant field. σ_{FS} is related with acoustic phonons having an acoustic wavevector $q \approx 0$. This term corresponds to photons scattered in a forward scattering configuration ($k_i = k_s$). The term σ_{BS} corresponds to a standing wave inside the spacer. It is responsible for the photons scattered with $q \approx 2k_i$ which are usually observable in backscattering configuration. This term gives rise to two Brillouin peaks: one corresponding to backscattering to the left and the other one corresponding to backscattering to the right. In an optical cavity, the modes which should be active in forward scattering are also detectable in backward scattering configuration and vice versa. This can be explained by the fact that both waves are standing waves inside the cavity. The excitation and scattered photons are bouncing back and forth in the cavity, before tunnelling through the DBRs. As a result, both contributions can be observed in any geometry.

2.3 Coherent generation and detection of acoustic phonons

The coherent generation and detection of acoustic phonons is based on a pump-probe experimental technique. It is in contrast with Brillouin scattering spectroscopy, where we study spontaneous emission or absorption of acoustic phonons. The pump-probe spectroscopy technique is a time dependent technique which allows to reconstruct the phonon dynamics over time [101].

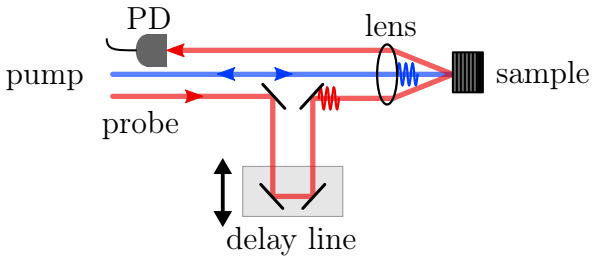

Figure 2.6: Schematic of a pump-probe experiment. The pump (blue) generates phonons in the system. The probe (red) is delayed in time and measures the change of reflectivity as a function of time. The signal is analyzed with a photodiode.

The principle of a pump-probe experiment is the following. A laser emits pulses of light of a few picoseconds or femtoseconds with a repetition rate of a few tens of MHz that are focused onto the sample. The light pulses are separated into two paths: the pump and the probe. In a very simplified protocol:

1. The pump pulse arrives on the sample at time $t_0 = 0$ ns. The pulse interacts with the sample and generates a strain which propagates through the sample. There are four mechanisms involved in the generation of coherent phonons: electrostriction, thermoelasticity, piezoelectricity and deformation potential [58]. The coherent phonons generated through this process modulate the optical properties of the medium through the photoelastic effect and induce the displacement of the interfaces.

2. The probe goes through a mechanical delay line and arrives on the sample with a delay time $t = t_0 + \Delta t$. The intensity of the reflected probe is modulated by the phonons generated in the medium [58]. The reflected probe is sent to a detector to measure the relative intensity of the beam, $\Delta R/R$. By controlling the time delay between the pump and the probe, the change in reflectivity is reconstructed as a function of time.

An experimental time-trace is displayed in Fig.2.7**a**. At $t = 0$ ns, the pump and probe reach the sample simultaneously. This appears as a rapid change from zero to 2.2 in the reflectivity. Then, the signal decays, as the optical cavity mode returns to equilibrium. A complete description of the optical response of the cavity is described in references [51, 86, 102, 103]. In the inset of Fig.2.7, we can see the modulation in the reflectivity induced by the presence of acoustic phonons. The oscillations have a period of ∼50 ps corresponding to an acoustic frequency $f_0 = 18.5$ GHz. The frequency spectrum is obtained after applying a fast Fourier transformation to the derivative of the time trace. The resulting spectrum is shown in panel **b** of Fig.2.7. The peak at 18.5 GHz corresponds to the confined acoustic mode.

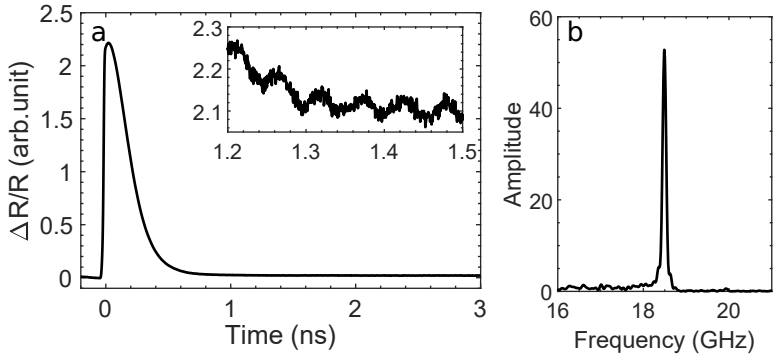

Figure 2.7: **a** Time trace of the optical reflectivity obtained from a pump-probe experiment on an optophononic Fabry-Perot resonator. At zero delay, a rapid change of the instantaneous reflectivity is the result of the pump pulse ultrafast action on the sample. Inset: zoom in the time resolved reflectivity. The oscillations with a ∼50 ps period feature the confined acoustic mode. **b** Phononic spectrum obtained after Fourier transforming the reflectivity time trace. The peak at 18.5 GHz corresponds to the fundamental mode of the structure.

2.4 Probing the mechanical motion by noise spectroscopy

In the context of cavity optomechanics, the interaction between optical and acoustic waves is usually studied through noise spectroscopy measurements. For an optomechanical resonator simultaneously confining light and sound, the mechanical and optical degrees of freedom are not independent. As a model, we consider a standard Fabry-Perot resonator made of two mirrors separated by a distance L and constituting a cavity with optical resonant frequency ω_c. One mirror is attached to a spring oscillating at a frequency ω_m, as displayed in Fig.2.8. When the spring is oscillating, the mirror displacement $u(t)$ modifies the length of the cavity, modulating the optical field inside the cavity. In return, the modulation of optical field induces a dynamic backaction on the

acoustic resonator [104]. The thermal fluctuations induced by the mechanical resonator on the optical cavity modulate the optical reflectivity $R(t)$ in time. Figure 2.9 shows a schematic of the optical reflectivity. The orange sinusoid represents the oscillations of the optical mode as a function of the acoustic displacement $u(t)$. In a Brownian motion experiment, a continuous wave laser is tuned on the flank of the cavity at a frequency ω_{laser}, where the slope is maximal. The variation in intensity of the reflected laser $I(t)$ is represented by a blue sinusoid. The reflected laser intensity is acquired in time with a photodiode and then sent to a spectrum analyzer. Thus, we can acquire the noise spectrum of the optomechanical resonator [85].

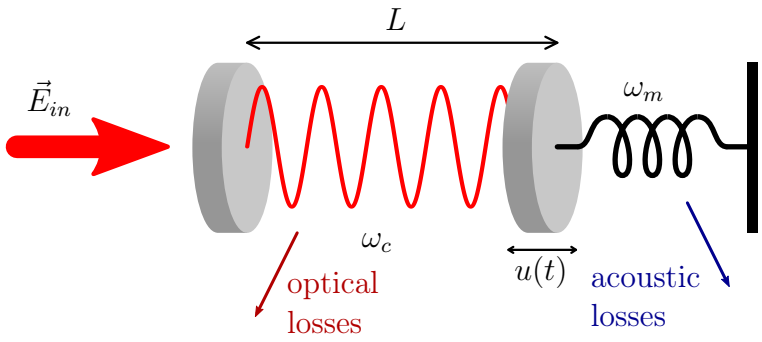

Figure 2.8: Schematic of an optomechanical Fabry-Perot resonator. The Fabry-Perot resonator is made of two mirrors forming an optical cavity. The right mirror is attached to a mechanical resonator. The optical and mechanical resonances are ω_c and ω_m, respectively. A incident beam $\vec{E}_{in}$ impinges on the Fabry-Perot resonator. The motion of the mirror is indicated by an arrow $u(t)$.

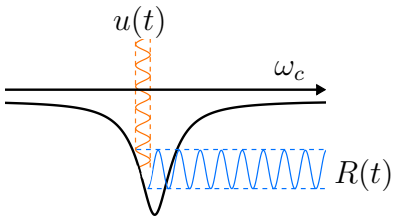

Figure 2.9: Schematic principle of Brownian motion. The orange sinusoid represents the fluctuations of the optical mode as a function of time due to the mechanical vibrations. The blue sinusoid represents the fluctuations of the reflected laser R(t) as a function of time.

In optomechanics, there is a vast spectrum of systems where the coupling of light and mechanical vibrations is studied. In Table 2.1 we compiled a list of representative devices studied with noise spectroscopy experiments and their figures of merit. The typical Fabry-Perot optophononic resonator studied in our group work at optical wavelength comparable to that of reference [105], which is shorter than most of the devices which are working in the mid-infrared and which benefit from all the available tools in the telecom range. On the contrary, the acoustic frequency of our resonator is above the ones of the devices presented in Table 2.1. The acoustic frequency of the Fabry-Perot multilayered cavity studied in our group is three orders of magnitude higher than that of the Bragg cantilever presented in reference [106] and two times higher than the frequency of the

diamond optomechanical crystal presented in reference [107]. The typical optical quality-factor of our device (in the 3000 to 11000 range) is rather low, especially considering reference [108] which is also at room temperature. A high-quality factor is important for the detection sensitivity. However, due to the colocalization of the optical and acoustic field in GaAs/AlAs superlattices, the acoustic quality-factor of the multilayered resonator presented in this thesis is similar to the optical one. A large mechanical quality factor is desired for self-cooling towards the quantum limit. Due to their acoustic frequency and optical wavelength, the devices studied in our group are challenging to study with noise measurement spectroscopy. Therefore, it is necessary to develop tools which are adapted to these characteristics.

Type of sample	Optical wavelength	Optical Q-factor or Finesse	Acoustic frequency	Acoustic Q-factor	T°	Power	Citation
Si toroidal µ-cavity	970 nm	6.2×10^6	58 MHz	2 890	RT	10 µW – 2 mW	[108]
TiO_2/SiO_2Bragg cantilever	1 064 nm	$F = 500 - 650$	0.2 – 5 MHz	9 000 – 2 000	RT	0.5 mW	[106]
clamped Si_3N_4 beam + Bragg mirror	1 064 nm	F = 3 900	0.945 MHz	30 000 5 000	5.3 K 300 K	7 µW	[109]
Si nanobeam	1 545 nm	30 000	2.9 GHz	2 300	RT/RP	40 µW	[78]
GaAs nanodisk	1 550 nm	10^5	300 – 800 MHz	1 000	RT/RP	-	[29]
Si nanobeam	1 537 nm	4×10^5	3.68 GHz	10^5	20 K	-	[110]
Si membrane	1 064 nm	F = 30 000	0.814 MHz	10 000	300 K	50 µW – 5 mW	[111]
Si waveguide	1 528 nm	22 000	54 MHz	450	RT	1 mW	[70]
SiN nanostring + Si toroid	1 548 nm	F = 230 000	8 MHz	40 000	RT	65 µW	[112]
diamond OMC	1 529 nm	1.76×10^5	5.5 – 12 GHz	4 100	RT/RP	-	[107]
Si racetrack cavity	1 535 nm	$0.4 - 2.4 \times 10^6$	6.03 GHz	13 MHz	RT	1 – 25 mW	[74]
GaAs nanotrumpet	940 nm	-	522.4 kHz 530 kHz	1 000 3 000	300 K 8 K	-	[105]
AlN ring	1 545 nm	125 000	0.3 – 1 GHz	1 200 – 2 500	RT		[113]
Silica Chiral PCF	1 500 nm	-	11 GHz	31 MHz	RT	0.95 W	[114]

Table 2.1: Devices studied with noise spectroscopy experiments and their characteristics in the literature.

2.5 Conclusions

In this chapter we discussed the photoelastic interaction which takes place between light and sound at the nanoscale. We discussed Brillouin scattering which is the inelastic scattering of light due to the presence of phonons in the medium. We introduced the different polarization and geometric selection rules of Brillouin scattering in semiconductor materials.
We explained that by engineering an optical cavity, the geometric selection rules are bent and all the modes are accessible in a backscattering geometry. In addition, the scattered signal is enhanced by the presence of an optical cavity. Both the incident and scattered beams can be resonant with the cavity when the angle of incidence on the sample is tuned to be in double optical resonance condition.
We also presented two other experimental techniques employed for the detection of phonons. The first one is the coherent generation and detection of acoustic phonons, which allows to study the dynamics of coherent acoustic phonons over time. This technique will be occasionally used in this thesis in Chapter 3. The second technique is the noise spectroscopy experiment usually used in the context of cavity optomechanics.
In this thesis, we study confined acoustic modes in optophononic resonators through the inelastic scattering of light with Brillouin spectroscopy. In Chapter 4, we will discuss how we take advantage of the double optical resonance to implement a filtering scheme for Brillouin spectroscopy. Finally, in Chapter 5, we discuss how we can bend the polarization selection rules of Brillouin scattering to achieve filtering based on the polarization.

Chapter 3

Acoustic confinement in one-dimensional topological structures

The study of topology enabled the development of new tools to describe the physical properties of matter, and in particular electronic properties such as topological insulators or the quantum hall effect[115, 116]. The principles of topology were transferred to other platforms (photons [117–120], polaritons [121–123], phonons [124, 125], acoustic vibrations or mechanical vibrations [32, 54, 126]) leading to the generation of a new class of topological devices. These devices show unchanged properties when they undergo local perturbations or fabrication defects [56].
In the previous chapter, we discussed the confinement of acoustics phonons in standard Fabry-Perot resonators. In this chapter, we extend the principle of multilayered structures to confine phonons in topological one-dimensional cavities. We take advantage of the relation between the topological and acoustic properties of superlattices to create an interface state between two DBRs. The presence of ultrahigh-frequencies topological acoustic interface states in GaAs/AlAs-based multilayered structures has already been demonstrated by means of Brillouin spectroscopy [31]. Moreover, in the optical domain, it was demonstrated that in superlattice devices, it is possible to generate optical interface states in any bandgap of the band-structure [120].
In this chapter, we present acoustic multilayered systems where topological interface states are generated in any bandgap of the nanoacoustic band-structure. In addition, we present a multilayered GaAs/AlAs structure which supports simultaneously an optical and an acoustic interface state.
First, we introduce the Su-Schrieffer-Heeger model which can be employed to describe the topological properties of periodic systems. We introduce the Zak phase, which is a topological invariant relevant for one-dimensional multilayered systems. We discuss the generation of topological interface states based on the principle of band inversion. We present the generalization of this principle to high-order bandgaps of the acoustic band-structure. Then, we present a GaAs/AlAs structure in which we can simultaneously design perfectly overlapping acoustic and optical interface states. We discuss the efficiency of these systems compared with a traditional Fabry-Perot resonator. Finally, we present experimental results on a one-dimensional topological optophononic resonator.

3.1 Topological microcavities by band inversion

3.1.1 The Su-Schrieffer-Heeger model

The devices we present in this chapter are designed in analogy with the Su-Schrieffer-Heeger (SSH) model [124, 127]. The SSH model was originally used to describe electrons in a one-dimensional polyacetylene chain composed of alternated single and double bonds connecting carbon atoms [128], as shown in Fig.3.1. In the tight binding approximation, we can associate an electronic band structure to the chain. The relative strength of the bonds defines the symmetries of the electronic wave function around the bandgap. When the unit cell changes from being centered around a double bond (panel **a** of Fig.3.1) to a single bond (panel **b**), the symmetries of the electronic wave functions around the bandgap are inverted. The swap in symmetries when changing the relative strength of the bond is the principle of band inversion. This results in two energetically degenerate isomers with different topological configurations [115].
This model could be applied to high frequency acoustic superlattice devices, since by alternating layers of GaAs and AlAs bandgaps are open. In this chapter, we extend the concept of band inversion to nanoacoustic superlattices to generate topological interface states.

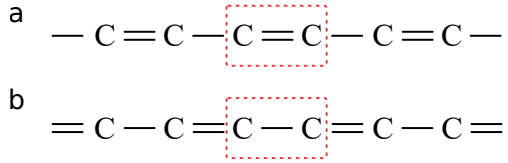

Figure 3.1: Polyacetylene molecule. The unit cell is indicated with a red box. **a** and **b** are two different topological cases.

3.1.2 Topological invariants

Let us consider a periodic phononic 1D system of periodicity a. The Zak phase of the n^{th} band is calculated by integrating across the Brillouin zone:

$$\theta_n^{Zak} = \int_{-\pi/a}^{\pi/a} \left[i \int_{unit\,cell} \frac{1}{2\rho(z)v^2(z)} dz u_{n,k}^*(z) \partial_k u_{n,k}(z) \right] dk, \tag{3.1}$$

where $u_{n,k}(z)$ is the acoustic displacement, k is the acoustic wave-vector and $\rho(z)$ and $v(z)$ are the mass density and speed of sound in the materials [126, 129]. We consider a periodic structure with inversion symmetry, that is the unit-cell is defined centro-symmetric around AlAs. Consequently, the Zak phase can only take two values: 0 or π [120, 126]. The Zak phase is the 1D equivalent of the Berry phase. It is associated with the symmetry of the Bloch modes at the band-edges. When the modes at both extremities of the same n^{th} band (i.e. at the edge and center of the Brillouin zone) have the same symmetries, $\theta_n^{Zak} = 0$ for the given band. On the contrary when a band has edge modes with opposite symmetries, $\theta_n^{Zak} = \pi$ [120].
We can characterize the topological properties of an acoustic multilayered device with the Zak phase.

3.1.3 Principle of band inversion in nanoacoustic multilayered structures

We consider acoustic DBRs made of GaAs/AlAs. For a designated acoustic frequency, the total acoustic path length of the unit cell is set to half a phonon wavelength. Therefore, the unit cell thickness must comply to

$$\frac{d_{GaAs}}{v_{GaAs}} + \frac{d_{AlAs}}{v_{AlAs}} = \frac{1}{2f_0^{ac}}, \tag{3.2}$$

where $d_{GaAs/AlAs}$ is the total thickness of GaAs/AlAs in the unit cell and $v_{GaAs/AlAs}$ is the speed of sound in the material. We define a parameter $\delta \in [-1, 1]$ to determine the relative thickness of AlAs and GaAs in the unit cell. The thicknesses of the two layers are then given by:

$$\begin{aligned} d_{GaAs} &= \frac{\lambda_{GaAs}}{4}(1+\delta) \quad \text{and} \\ d_{AlAs} &= \frac{\lambda_{AlAs}}{4}(1-\delta). \end{aligned} \tag{3.3}$$

When $\delta = 0$, it corresponds to the case of a superlattice made of ($\lambda/4$, $\lambda/4$) GaAs/AlAs layers. When $\delta = 1$ the unit cell is purely made of GaAs, and when $\delta = -1$ it is purely made of AlAs. We define a centro-symmetric unit-cell around AlAs, i.e., the GaAs layer in the unit cell is equally distributed around the AlAs layer as following: $\frac{\lambda_{GaAs}}{8}(1+\delta)$, $\frac{\lambda_{AlAs}}{4}(1-\delta)$, $\frac{\lambda_{GaAs}}{8}(1+\delta)$.
Figure 3.2 displays the acoustic dispersion relations for superlattices complying to equation 3.2, with $f_0^{ac} \sim 9$ GHz. The thicknesses of the layers are defined using equation 3.3 for three different values of δ associated to the three panels in Fig.3.2. We observe that for values of δ with opposite signs, the band diagrams are comparable. In the case of $\delta = 0$, the second band gap, indicated by a red box, is closed. Note that by only varying δ, the bandgap stays centered around the same frequency. Moreover, we focus on the second bandgap, but all the bandgaps are affected by changing δ. Only the first bandgap remains open for all values of δ except when $\delta = \pm 1$. The behavior of the other bandgaps will be discussed in section 3.2.1.

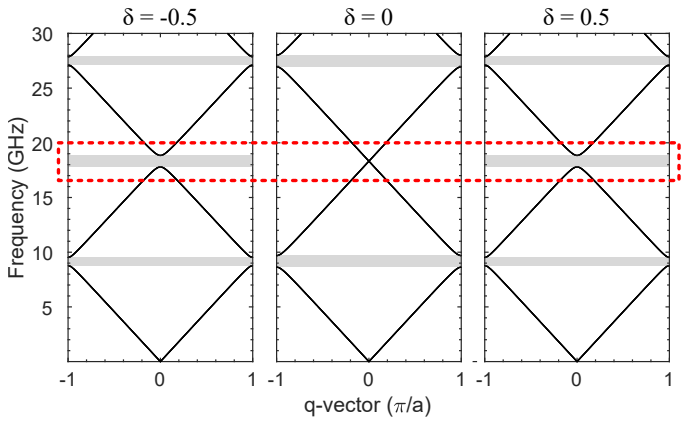

Figure 3.2: Acoustic dispersion relation of superlattices with $\delta = \pm 0.5$ and $\delta = 0$. The grey rectangles mark the positions of the acoustic bandgaps. The red box indicates the bandgap opening and closing by varying δ.

Let us focus on the second band gap at ∼18 GHz, at the center of the Brillouin zone. When varying δ continuously over [-1, 1], the width of the acoustic bandgap changes. In Fig.3.3, the lines indicate the frequency of the band-edge modes enclosing the bandgap. The interval between the two band-edges corresponds to the span of the acoustic bandgap. The mode symmetries, symmetric (orange line) and anti-symmetric (blue line), are defined with respect to the center of the unit cell. The acoustic displacement pattern inside the unit cell is represented as insets for the two band-edge modes when $\delta < 0$ and $\delta > 0$. When $\delta < 0$, the displacement of the lower edge-mode is symmetric with respect to the center of the unit cell and the upper edge-mode is anti-symmetric. At $\delta = 0$ the bandgap closes. When $\delta > 0$, the symmetries of the edge modes undergo an inversion. In the case of the second bandgap, this transition is characterized by the Zak phase changing from 0 to π [130].

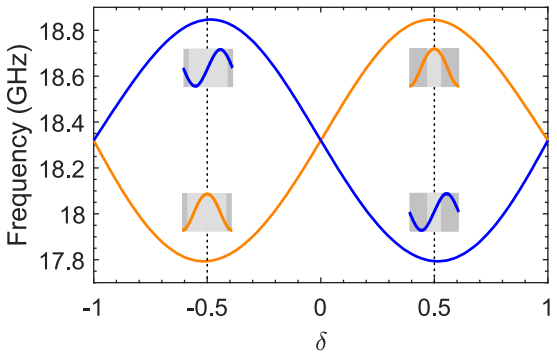

Figure 3.3: Band inversion of the acoustic bandgap at the center of the Brillouin zone around 18.3 GHz. The frequency of the band-edges (orange and blue) bounding the bandgap is plotted as a function of the parameter δ. A sign change in δ marks the transition between the topological phases of a superlattice. For $\delta < 0$ the Bloch mode at the lower (upper) band-edge has a symmetric (anti-symmetric) displacement pattern with respect to the centers of the unit cell, these symmetries exchange for $\delta > 0$. The band-edge modes are illustrated in the insets. The mode symmetries are indicated with orange (symmetric) and blue (anti-symmetric) lines.

We look at two specific cases marked by vertical lines in Fig.3.3, at $\delta = \pm 0.5$. The acoustic dispersion relations of those two cases are plotted in Fig.3.4, with a schematic of the unit cell on top. When $\delta = -0.5$, the modes at the center and at the edge of the Brillouin zone for the second band are both symmetric. Therefore, the Zak phase attributed to the band is zero. On the contrary, when $\delta = +0.5$, the mode at the center of the Brillouin zone for the second band is symmetric while the mode at the edge of the Brillouin zone is anti-symmetric, resulting in the Zak phase equal to π [120]. By changing the relative thickness of GaAs and Alas in the unit cell, we can modify the topological properties of the superlattice.

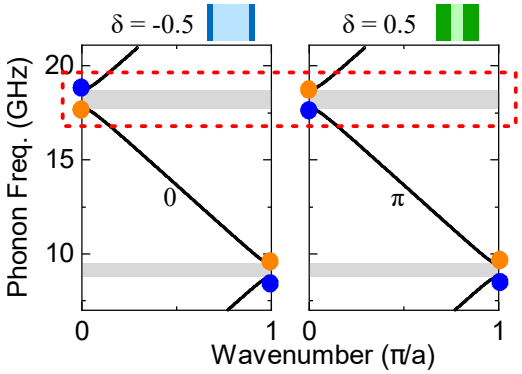

Figure 3.4: Acoustic dispersion relation of two superlattices with $\delta = -0.5$ and $\delta = 0.5$. The schematics of the unit cells of each superlattice are represented in insets. The two dispersion relations present inverted Bloch mode symmetries around the bandgap at the Brillouin zone center. The red box indicates the bandgap over which the band inversion takes place. The mode symmetries are indicated with orange (symmetric) and blue (anti-symmetric) dots. The Zak phase of the second band is indicated.

3.1.4 Interface states

To get a confined mode at a given frequency f_{ac} in a Fabry-Perot resonator, two DBRs with bandgaps centered around f_{ac} are concatenated with a spacer of length $p\lambda_{ac}/2$ in between. We define $r = e^{i\phi(f)}$ the complex reflection coefficient of a semi infinite DBR, where $\phi(f)$ is the reflection phase of the system. To achieve a stationary wave, the reflection phases of both DBRs (ϕ_{top} and ϕ_{bottom}) and the phases acquired through the spacer must add up to a multiple of 2π [130]:

$$\phi_{top} + \phi_{bottom} + \phi_{spacer} = 2m\pi, \quad m \in \mathbb{Z}. \tag{3.4}$$

In the case where there is no spacer, this relation would give:

$$\phi_{top} + \phi_{bottom} = 2m\pi, \quad m \in \mathbb{Z}. \tag{3.5}$$

We take advantage of the relationship between the reflection properties and the topological properties of the superlattices to predict the existence of an interface state [124, 126]. It has been demonstrated that the reflection phase $\phi(f)$ in the second bandgap is connected to the Zak phase [120]. The sign of the reflection phase for the first Brillouin zone center acoustic bandgap is given by:

$$sgn(\phi) = e^{i(\theta_0^{Zak} + \theta_1^{Zak})}. \tag{3.6}$$

We consider the two cases presented in Fig.3.4. They feature two different unit cells with $\delta = \pm 0.5$ and the corresponding Zak phases. When $\delta < 0$, $sgn(\phi) = -1$, whereas $sgn(\phi) = 1$ when $\delta > 0$. Therefore, by concatenating these two superlattices equation 3.5 is respected, resulting in the presence of an interface state between the DBRs [125]. Figure 3.5**a** displays the simulated reflectivity for a topological acoustic resonator designed at f_{ac} ∼18 GHz. The structure is formed by two concatenated DBRs embedded in GaAs. Each DBR is made of 16 unit cells with $\delta_{top} = -0.5$ and $\delta_{bottom} = 0.5$, with a bandgap centered around f_{ac} ∼18 GHz. In Fig.3.5**a**, there is a dip in the reflectivity

bandgap, featuring the confined topological interface mode in the middle of the bandgap at the zone center of the Brillouin zone. The spatial displacement $|u(z)|^2$ of the topological acoustic interface state at ∼18 GHz is represented on Fig.3.5**b** together with the complete structure. The amplitude of the displacement is maximum at the interface and decays evanescently in the DBRs.

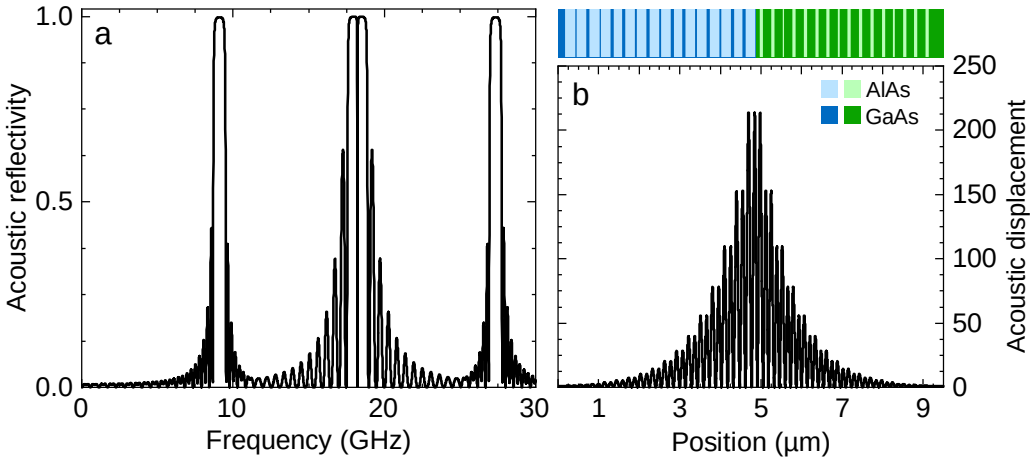

Figure 3.5: **a** Simulated acoustic reflectivity for a topological resonator formed by two concatenated DBRs with $\delta = -0.5$ and $\delta = 0.5$ embedded in GaAs. The topological interface mode appears as a dip in the bandgap at ∼18 GHz. **b** The spatial displacement pattern $|u(z)|^2$ of the topological interface state at ∼18 GHz presents a maximum at the interface between the two DBRs. The fields decay evanescently away from the interface. The complete heterostructure is represented at the top. The dark (light) colors represent GaAs (AlAs). Green and blue are to differentiate both DBRs.

3.2 High-order bandgap engineering

As we discussed above, for the second bandgap the symmetry of the displacement pattern with respect to the centers of the unit cell at the lower and upper band-edges reverses when δ crosses zero. The inversion of symmetry of the modes around the bandgap also occurs at higher bandgaps. Thus, interface states can be generated by applying the method presented in the previous section 3.1.4. Versatile topological devices can be engineered where we could create high-frequencies interface states in a broad frequency range and hybrid structures combining superlattices designed for different acoustic frequencies.

3.2.1 Generalization of the band inversion principle

The evolution of the first, second, third and fourth bandgaps as a function of δ (relative thickness ratio of GaAs/AlAs) are plotted on Fig.3.6. The orange lines indicate modes which are symmetric with respect to the center of the unit cell, while the blue lines indicate anti-symmetric modes. When varying δ, there are changes in the width of the bandgaps. For certain values of δ the bandgaps close and the modes surrounding the bandgaps undergo inversion of symmetry when they reopen. The number of nodes is

related to the order of the bandgap. The first bandgap (panel **d**) opens and closes only once. It reaches a maximum of amplitude at $\delta = 0$. At the third bandgap, the band-edge modes change symmetry twice (panel **b**). At the fourth bandgap the symmetry of the modes changes thrice (panel **a**). In general, for the n^{th} bandgap, there are $(n-1)$ inversions of symmetries.

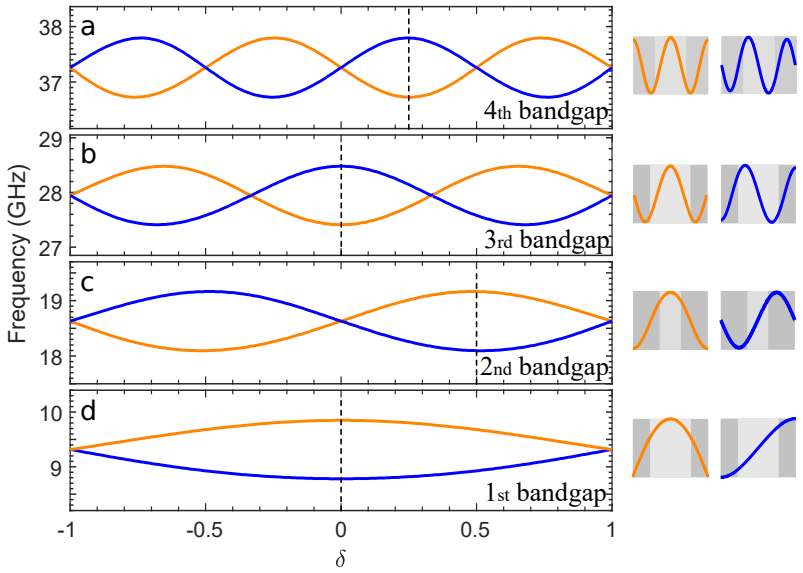

Figure 3.6: Band inversion of the acoustic bandgap around **a** 9.3 GHz, **b** 18.6 GHz, **c** 28 GHz and **d** 37.3 GHz. The frequency of the band-edges bounding the bandgap is plotted as a function of the parameter δ. The mode symmetries are indicated with orange (symmetric) and blue (anti-symmetric) lines. The acoustic displacements $|u(z)|^2$ of the edge modes are plotted in the unit cells for the different bandgaps. The thickness ratio of GaAs/AlAs is indicated by the vertical dashed line in each case.

3.2.2 Interface states at higher bandgap order

Fundamentally, an interface state appears when concatenating two DBRs with opposite reflection phase signs. For the n^{th} bandgap, the sign of the reflection phase is given by [120]:

$$sgn(\phi) = (-1)^n(-1)^l \times \exp\left(i\sum_{m=0}^{n-1}\theta_m^{Zak}\right), \tag{3.7}$$

where l is the number of closed bandgaps below the n^{th} bandgap. Therefore, for the n^{th} bandgap, there is an interface state at the condition that $\sum_{m=0}^{n-1}\theta_m^{Zak} = 0 + 2p\pi, p \in \mathbb{N}$ for one DBR and $\sum_{m=0}^{n-1}\theta_m^{Zak} = \pi + 2p\pi, p \in \mathbb{N}$ for the other one.
The generation of an interface state at the n^{th} bandgap between two DBRs with different topological properties results in the combination of two DBRs with opposite mode symmetries around the n^{th} bandgap. The creation of an interface state at the n^{th} bandgap does not necessarily imply the generation of an interface state in other bandgaps.
Panels **a** to **c** of Fig.3.7 display reflectivity spectra which are obtained by combining two DBRs with different values of δ. In each case, the amplitude of the third bandgap of the corresponding superlattice is maximized. The values of δ are marked on the respective

top panel with vertical dashed lines. In panels **a** and **c**, the two DBRs have inverted symmetry around the bandgap. In the acoustic reflectivity spectra there is a dip centered in the high reflectivity region featuring the interface state. Whereas, in panel **b**, the two DBRs have the same symmetry around the bandgap. Thus, the structure acts as a standard DBR and the reflectivity spectrum presents only a high reflectivity region. In general terms, for the third bandgap, there are two alternatives to generate an interface state. That is, a DBR with δ in the second opening of the bandgap ($\delta \in [-0.33, 0.33]$) can be concatenated with a DBR either having $\delta < 0.33$ (Fig.3.7**a**) or $\delta > 0.33$ (Fig.3.7**c**).

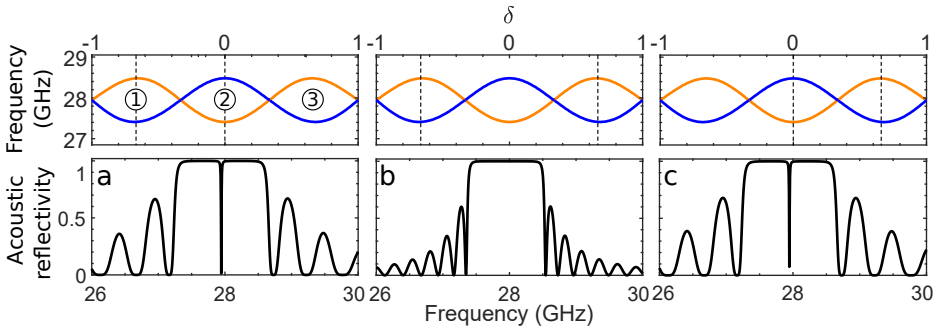

Figure 3.7: Top panel: Band inversion of the third acoustic bandgap around 28 GHz. **a,b, c** Calculated acoustic reflectivity spectra. The values of δ selected for the two concatenated DBRs are marked by dashed lines on the corresponding top panel.

In the case of the fourth bandgap, Fig.3.8 displays the acoustic reflectivity spectra of six possible combinations between two DBRs with different values of δ. Again, the amplitude of the bandgap is maximized for all cases, resulting in high reflectivity regions centered around ∼28 GHz. The different δ used for the design of the unit cells are marked by vertical dashed lines in the bandgap. In cases **b** and **e**, the two DBRs which are concatenated have the same symmetry (both modes at the bottom band are symmetric in panel **b**, while they are anti-symmetric in panel **e**). Thus, the acoustic reflectivity spectra present high reflectivity regions like a standard DBR. On the contrary, for panels **a**, **c**, **d** and **f** the two DBRs which are concatenated have inverted symmetries. Therefore, an interface state is generated. Generally, an inversion of symmetry of the modes around the n^{th} bandgap takes place when going from an odd to an even opening of the bandgap (or vice-versa). Consequently, to generate an interface state, it is needed to concatenate two DBRs corresponding to superlattices with an even and an odd opening of the bandgap (for example panel **a** in Fig.3.7 and panel **c** of Fig. 3.8).

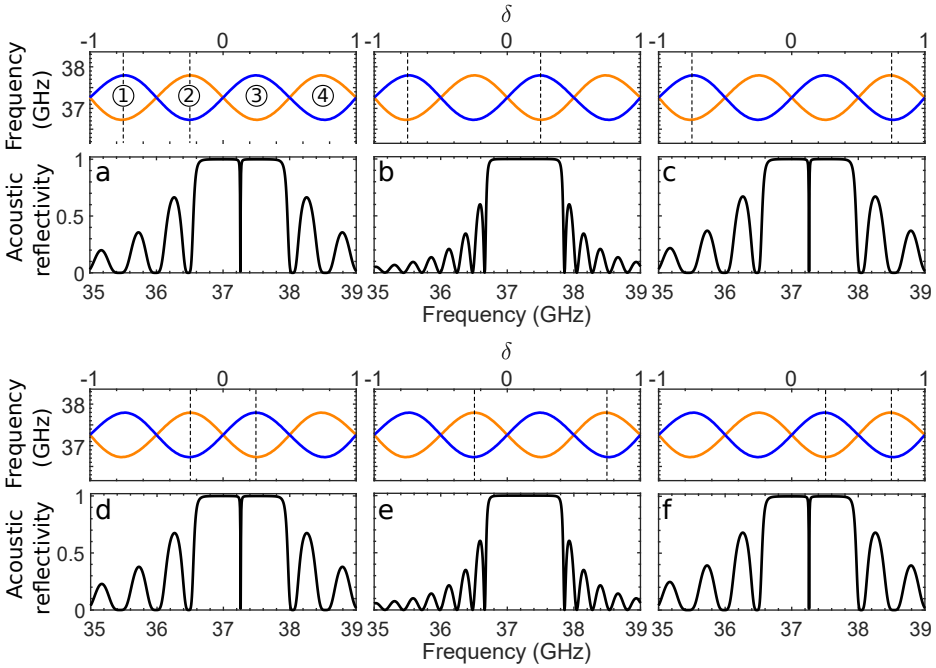

Figure 3.8: **a-f** Calculated acoustic reflectivity spectra. Top panel: Band inversion of the fourth acoustic bandgap around 37.3 GHz. The values of δ selected for the two concatenated DBRs are marked by dashed lines on the corresponding top panel.

3.2.3 Robustness against disorder

The band inversion principle exploited here to build topological resonators preserves the center of the bandgap by varying δ. In this section, we numerically show that the robustness of the interface mode applies to all bandgap orders when introducing a particular kind of noise in the layer thickness. We compare the topological interface state generated in the third bandgap presented in panel **c** of Fig.3.7 to a Fabry-Perot cavity formed by non-centrosymmetric unit cells of GaAs/AlAs with $\delta = 0.66$ surrounding a spacer of thickness λ and embedded in a GaAs background. We implement the noise using a flat distribution of random number with an amplitude $\Delta\delta/\delta$ ranging from zero (unperturbed system) to 0.5 (0.999 being the local bandgap which can almost completely close due to fluctuations). The results for the topological (blue) and the Fabry-Perot (orange) resonators are presented in panels **a** and **b** of Fig.3.9. The acoustic frequencies of the interface state generated at the third bandgap of the two systems are compared in panel **a** of Fig.3.9. When introducing the local fluctuations in the layer thickness, the resonance of the topological resonator stays fixed at the bandgap center, whereas the mode of the Fabry-Perot resonator fluctuates away from the center. Figure 3.9**b** compares the acoustic quality factors of the two structures. Both quality factors decrease by a factor 10 when the fluctuations increase. This effect can be explained by the reduction in the width of the bandgap, resulting in the growth of the evanescent decay length of the confined mode and thus in the enhancement of the leakages through the DBRs into the background [51]. The quality factor of the Fabry-Perot resonator decreases faster for small noise fluctuations.
Likewise, we compare the topological interface state generated in the fourth bandgap,

presented in panel **c** of Fig.3.8, to a Fabry-Perot cavity formed by non-centrosymmetric unit cells of GaAs/AlAs with $\delta = 0.75$ surrounding a spacer of thickness $\lambda/2$ and embedded in a GaAs background. The results for the topological (blue) and the Fabry-Perot (orange) resonators are presented in panels **c** and **d** of Fig.3.9. The acoustic frequencies of the interface state generated at the fourth bandgap of the two systems are compared in panel **c** of Fig.3.9. The behavior is similar to the case of the third bandgap: the frequency is clamped at the bandgap center for the topological structure and fluctuates for the Fabry-Perot resonator. The acoustic quality factor of the two structures, shown in panel **d** of Fig.3.9, decreases by more than an order of magnitude. The quality factor of the topological interface state at the fourth bandgap is more sensitive to fluctuations than in the case of the third bandgap. These results show that the robustness characteristic of topological devices, protecting the acoustic resonance against disorder, also operates at high-orders of the bandgap.

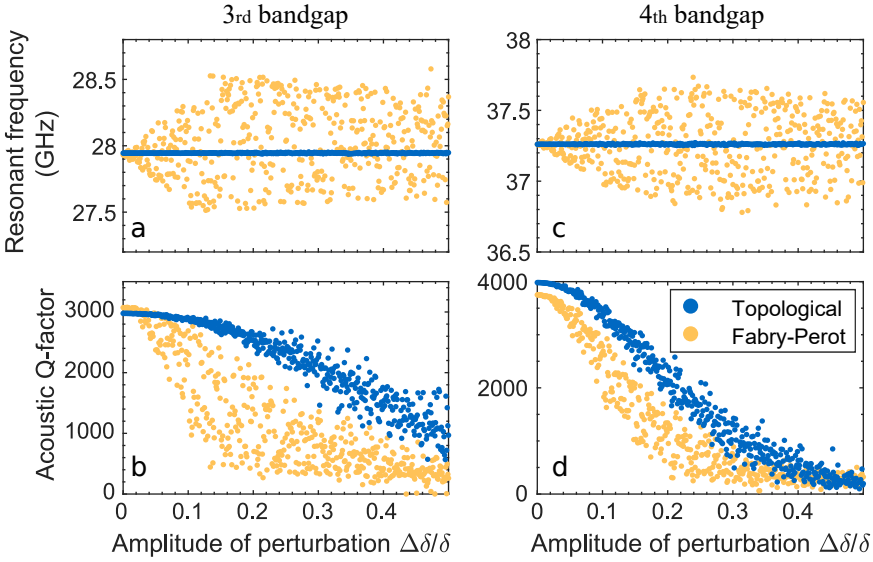

Figure 3.9: **a** Resonant frequency in the third bandgap under random perturbations. We choose random variations with a uniform distribution of width $\Delta\delta/\delta$. The acoustic resonance frequency stays trapped at the bandgap center for the topological mode (orange) but undergoes variations for the Fabry–Perot case (blue). **b** Acoustic quality factor under random perturbations. For both types of resonators, the acoustic quality factor drops by a factor of ten. Likewise **c** and **d** for the fourth bandgap, respectively.

3.2.4 Multimode engineering

In the previous section we showed that we can engineer the interface states at the n^{th} bandgap in topological acoustic resonators by carefully choosing the appropriate material ratio in both juxtaposed DBRs. In this section, we present designs of topological acoustic resonators realized for various ratios of GaAs/AlAs in the two unit cells determining the topological structure.

By varying δ, we simultaneously alter the bandgap amplitudes at all the orders. However, the closing and reopening of the bandgaps is not coincident for all bandgap orders. As δ is changing, we can reach different combinations of bandgap symmetries and thus engineer the formation of interface states. It is then possible to address the generation of

multimode interface states, with the only constraint that all the bandgaps are modified simultaneously by δ.
Figure 3.10 presents conditions to generate interface states in the second and fourth bandgap. Panel **b** shows the unit cells at the interface. In that case, we chose $\delta = \pm 0.33$. Panel **a** reproduces the band inversion from Fig.3.6. The values of δ chosen for the top and bottom DBR are marked by vertical dashed lines. The symmetries of the modes around the bandgap are marked by blue (anti-symmetric) and orange (symmetric) dots. As an inset, the symmetries of the band in the two DBRs are plotted together. In that case, we observe that there is an inversion of symmetry at the second and fourth bandgaps. At the particular value of δ chosen here, the third bandgap is closed. In the calculated acoustic reflectivity spectra (panel **c**) the closed bandgap appears as a minimum in reflectivity, while the interface states due to the inversion of symmetry are the dips centered in the high reflectivity regions at ∼18 GHz and ∼37 GHz.

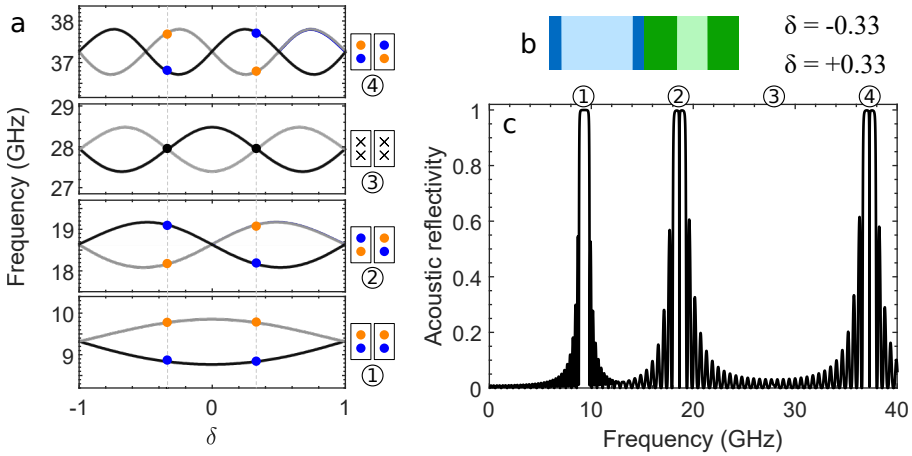

Figure 3.10: **a** Band inversion of the acoustic bandgaps. The dots show the bandgaps opening and symmetries at the given δ. Inset: Symmetry of the two concatenated DBRs. There is inversion for the second and fourth bandgaps, while the third bandgap is closed. **b** Schematic of the unit cells at the interface between the two DBRs. **c** Simulated acoustic reflectivity spectra for two topological resonators formed by two concatenated DBRs embedded in GaAs with **a** $\delta_{top} = -0.33$ and $\delta_{bottom} = +0.33$

Figure 3.11 presents conditions to generate interface states in the third and fourth bandgaps simultaneously. The structure is designed with $\delta_{top/bottom} = -0.15/-0.85$ for the top and bottom DBRs. In comparison to the previous case, the four bandgaps are open for both superlattices (see panel **a**), resulting in four high reflectivity regions in the reflectivity spectrum plotted in panel **c**. In the third and fourth bandgaps, there are interface states indicated by dips in the high reflectivity regions of the reflectivity spectrum. They are induced by the inversion of symmetry of the modes around the third and fourth bandgaps, as shown in panel **a**. On the contrary, there is no interface mode in the first and second bandgaps because they have the same band-edge symmetries for both superlattices.
Note that the mode is not centered in the third bandgap as we can see in panel **c** of Fig.3.11. Two conditions to generate an interface state between two acoustic DBRs centered in the bandgap are: *i)* common bandgap must have equal central frequency and *ii)* same bandwidth. The first one is necessary for topological robustness. The

second condition results in similar evanescent decay lengths into both DBRs. In case δ is not symmetric with respect to an inversion point, the interface state generated is not centered in the bandgap, as we can see in Fig.3.11 and 3.12 at the third and second bandgaps, respectively.

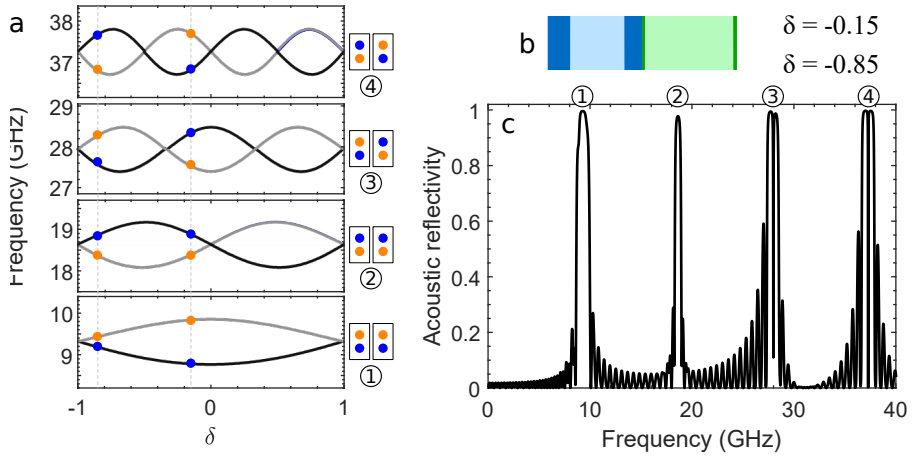

Figure 3.11: **a** Band inversion of the acoustic bandgaps. The dots show the bandgaps opening and symmetries at the given δ. Inset: Symmetry of the two concatenated DBRs. There is inversion for the third and fourth bandgaps. **b** Schematic of the unit cells at the interface between the two DBRs. **c** Simulated acoustic reflectivity spectra for two topological resonators formed by two concatenated DBRs embedded in GaAs with **a** $\delta_{top} = -0.15$ and $\delta_{bottom} = -0.85$

Figure 3.12 presents conditions to generate interface states in the third and fourth bandgaps with $\delta_{top/bottom} = -0.8/+0.2$. On panel **a**, the two DBRs have inverted symmetry at the second and third bandgaps. Even though they fall into different openings of the fourth bandgap, both have the same symmetry.

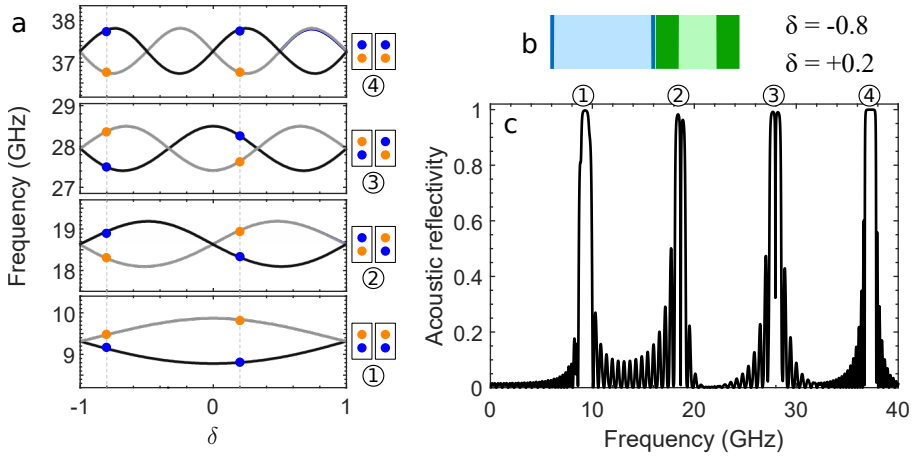

Figure 3.12: **a** Band inversion of the acoustic bandgaps. The dots show the bandgaps opening and symmetries at the given δ. Inset: Symmetry of the two concatenated DBRs. There is inversion for the second and third bandgaps, while the third bandgap is closed. **b** Schematic of the unit cells at the interface between the two DBRs. **c** Simulated acoustic reflectivity spectra for two topological resonators formed by two concatenated DBRs embedded in GaAs with **a** $\delta_{top} = -0.8$ and $\delta_{bottom} = +0.2$

Figure 3.13 presents conditions to generate interface states in the third and fourth

bandgaps with $\delta_{top/bottom} = +0.4/+0.6$. There is very little difference between the unit cells of the two superlattices as shown in panel **b**. However, the modes at the fourth bandgap have inverted symmetry. All the other bandgaps fall in the same openings. Therefore, the acoustic reflectivity spectrum (panel **c**) presents four high reflectivity regions, with only one interface mode in the fourth bandgap.
Note that there is no inversion of the band symmetry and it is impossible to create an interface state at the first bandgap because the topological phase of the lower band around the first bandgap (at the zone edge of the Brillouin zone) does not switch with the variation of δ.

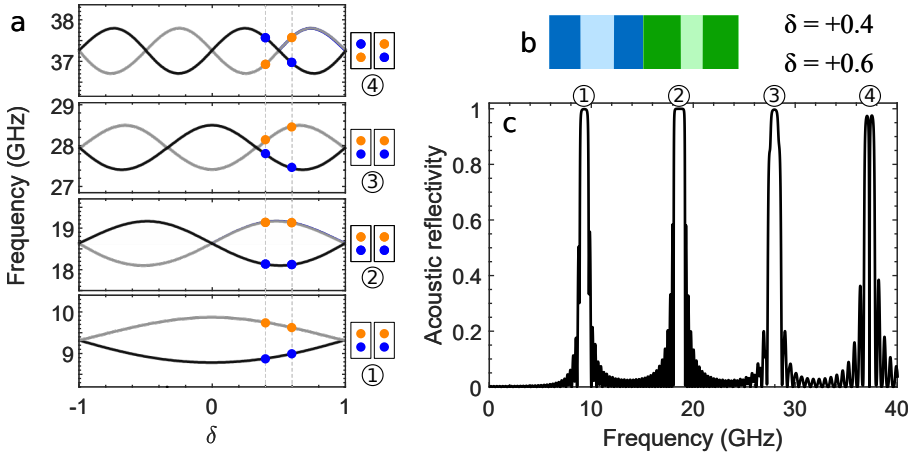

Figure 3.13: **a** Band inversion of the acoustic bandgaps. The dots show the bandgaps opening and symmetries at the given δ. Inset: Symmetry of the two concatenated DBRs. There is inversion only for the fourth bandgap. **b** Schematic of the unit cells at the interface between the two DBRs. **c** Simulated acoustic reflectivity spectra for two topological resonators formed by two concatenated DBRs embedded in GaAs with **a** $\delta_{top} = +0.4$ and $\delta_{bottom} = +0.6$

3.2.5 Hybrid topological resonators

To generate an interface state at a given acoustic frequency between two DBRs, it is required they have bandgaps with overlapping frequency ranges. So far, we created interface modes in a given bandgap by concatenating two DBRs designed at the same acoustic frequency. In this section, we generate an interface state between two DBRs designed at different fundamental frequencies, resulting in bandgaps of different orders sharing the same frequency range.
The band inversion of the two superlattices are plotted in panels **a** and **b** of Fig.3.14. The first superlattice S1 (panel **a**) is designed to have a fundamental bandgap centered around 9.3 GHz, while the second superlattice (S2) is designed at 14 GHz (panel **b**). This results in the third bandgap of S1 centered at the same frequency as the second bandgap of S2. However, none of the lower order bandgaps have matching frequencies. Panel **c** presents the acoustic reflectivity spectra of the two DBRs associated to the band structures in panels **a** and **b**. The reflectivities are calculated for values of δ where all the bandgaps are open. The high reflectivity regions only overlap around 28 GHz. Hence, it is possible to generate an interface state at 28 GHz. Panels **d** to **g** of Fig.3.14 present calculated acoustic reflectivity spectra for four different combinations of DBRs.

The values of δ utilized are identified on the band inversion figures with vertical dashed lines. The labels indicate the corresponding acoustic reflectivity spectrum. For panel **d**,**e** and **f**, there is an interface state at 28 GHz. The only difference between the cases **d** and **f** is the thickness ratio used to design the unit cell of the DBR S1. In spite of this difference, the symmetries around the third bandgaps of S1 are the same in both cases. In these two cases, all the bandgaps at lower frequencies are open, resulting in three high reflectivity regions. For panel **e**, since the second bandgap of S1 is closed, there are only two high-reflectivity regions at lower frequencies. For the three cases, there is a dip in the reflectivity at 28 GHz featuring the interface state. For case **g**, all the bandgaps are open, resulting in five high-reflectivity regions. However, there is no interface state. It is important to mention that the rule to create an interface state by band inversion does not apply for bandgaps of different orders. In the case presented in Fig.3.14 an interface state is generated when the modes surrounding the bandgap of interest have same symmetries in both superlattices. We can generalize that when one bandgap is even and the other one is odd, an interface state is generated if both have similar symmetries. On the contrary, if two odd or even bandgaps are concatenated, both need to have inverted symmetries to generate an interface state. This is because, the difference in phases of the reflection coefficient does not only depends on the sum of the Zak phases anymore but also on the order of the bandgap.

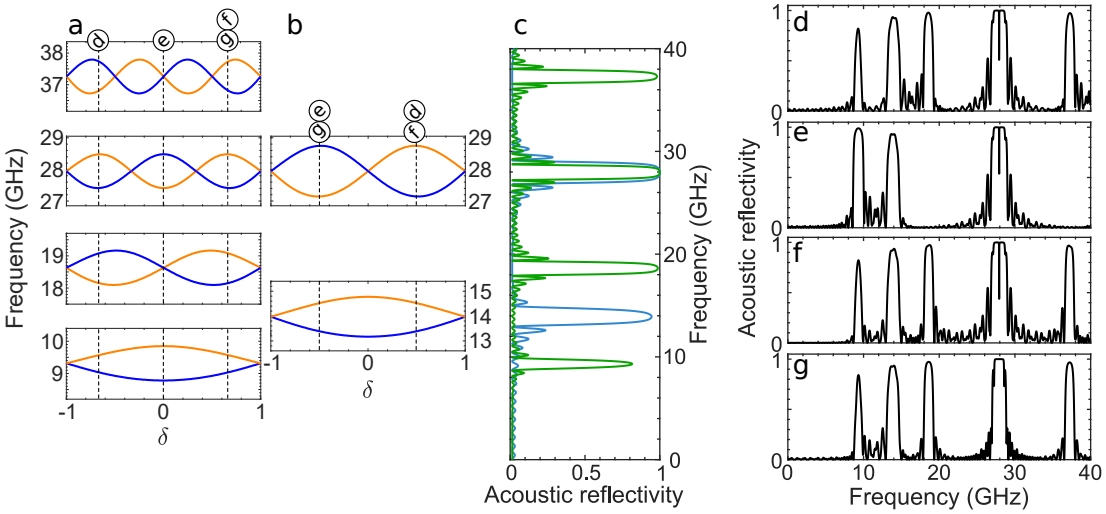

Figure 3.14: Hybrid topological acoustic resonator. **a, b** Band inversion of the acoustic bandgaps associated with the two concatenated DBRs. The third bandgap of the superlattice **a** and the second bandgap of the superlattice **b** share the same central frequency. **c** Simulated acoustic reflectivity of the two DBRs. The green line (blue) corresponds to the band inversion diagram displayed in panel **a** (panel **b**, respectively). **d, e, f, g** Simulated acoustic reflectivity spectra for different concatenated DBR embedded in GaAs. δ of the corresponding DBRs is marked by dashed lines on panel **a** and **b**.

Note that the presence of an interface mode at a frequency f_0 is not determinant of an interface mode at $2f_0$. Here, the sixth and fourth bandgaps of the superlattices S1 and S2 (respectively) would be closed at 56 GHz for the chosen values of δ. However, at 84 GHz, the bandgaps (corresponding to the ninth and sixth orders, respectively) are open with identical symmetries, leading to an interface state. The possibility to create an interface state in a bandgap at different orders gives the opportunity to explore a

full class of hybrid topological resonators which would be difficult to study in optics or electronics due to the dispersion relations.

3.3 Simultaneous confinement of light and sound by band inversion

3.3.1 Simultaneous band-inversion

As we have seen in Chapter 1, in GaAs/AlAs the optical and acoustic fields are superimposed in a multilayer system. Moreover, a Fabry-Perot resonator designed to confine an acoustic mode at ∼18 GHz also confines an optical mode around 900 nm. Likewise, the principle of band inversion in the acoustic domain also occurs in the optical domain. For a superlattice designed to have the second bandgap centered around the acoustic frequency $f_{ac} = 18$ GHz, there is a simultaneous inversion of the mode symmetries for both the acoustic displacement and the optical field when δ crosses zero. Similarly to the acoustic band-dispersion, the lower band-edge mode of the optical bandgap at ∼1.34 eV is symmetric when $\delta < 0$ and anti-symmetric when $\delta > 0$. Whereas the upper band-edge mode is anti-symmetric when $\delta < 0$ and symmetric when $\delta > 0$. This results in both cases having different Zak phases. In Fig.3.15, similarly to Fig.3.4, the edge-modes at the band gap at the zone center of the Brillouin zone invert their symmetries when the sign of δ changes.

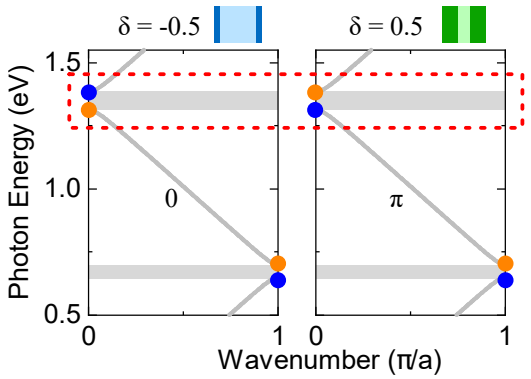

Figure 3.15: Optical dispersion relation of two superlattices with $\delta = -0.5$ and $\delta = 0.5$. The schematic of the unit cells of each superlattice is represented in insets. The two dispersion relations present inverted Bloch mode symmetries around the bandgap at the Brillouin zone center. The dashed red box indicates the bandgap over which the band inversion takes place. The mode symmetries are indicated with orange (symmetric) and blue (anti-symmetric) dots. The Zak phase of the second band is indicated.

Therefore, by concatenating two DBRs with inverted bandgaps, we engineer an optophononic topological cavity, simultaneously confining phonons and photons. Figure 3.16 displays the acoustic displacement $|u(z)|^2$ and optical field $|E(z)|^2$ for a topological optophononic resonator formed by 14 (16) GaAs/$Al_{0.95}Ga_{0.05}$As centro-symmetric unit cells with $\delta_{top} = -0.5$ ($\delta_{bottom} = +0.5$) at the top (bottom). The structure is surrounded by a GaAs substrate on one side and air on the other side. The superlattices are designed to have the interface state at the center bandgap at 18 GHz in the acoustic domain and

1.34 eV in the optical domain. Both the optical field and the acoustic displacement are colocalized and present a maximum of amplitude at the interface between the two DBRs. This structure will be experimentally studied in a following section.

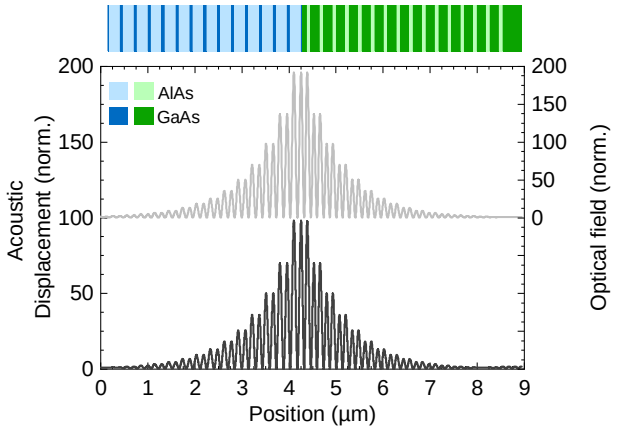

Figure 3.16: The spatial displacement pattern $|u(z)|^2$ (black) and optical profile $|E(z)|^2$ (grey) of the topological interface state at 18.12 GHz/1.34 eV are colocalized and present a maximum at the interface between the two DBRs. Both fields decay evanescently away from the interface. The complete heterostructure is represented at the top.

3.3.2 Topological engineering of the interface states and interactions

Until section 3.3 we were discussing only acoustic topological interface states. However, there is a simultaneous band inversion for the acoustic and optical dispersion relation at ∼18 GHz and ∼900 nm, respectively. The resulting colocalized optical and acoustic states offer the possibility of studying the topology of the interactions.
In this section, we theoretically compare four topological structures and a standard Fabry-Perot resonator. We consider topological structures made of two concatenated DBRs presenting inverted bands and centrosymmetric unit cells. We engineer the interface state by changing two parameters: the sign of δ, and the DBR inversion centers which coincide with the origin of the unit cells. This means that the materials of the layers forming a centrosymmetric unit cell are swapped. By combining those parameters, we can consider different topological combinations (see Table 3.1). The different configurations are displayed in the table as a function of $\delta_{top/bottom}$ and the central material of the unit cell. Due to the symmetry of the structure, the table has a diagonal symmetry, resulting in only six different topological structures. The diagonal, with the cases shaded in grey, corresponds to symmetric cases, where the top and bottom DBRs are identical. The simulations of the Brillouin cross-section presented in this section are performed using the transfer matrix method and a photoelastic model, assuming $p = 1$ in Ga-rich layers and $p = 0$ in Al-rich layers. The laser wavelength is considered at the optical resonance. The acoustic resonators are made from two DBRs where each DBR consists of 16 periods, surrounded by GaAs. Here we present only the five cases wich are indicated in the table by the corresponding letter in Fig.3.17.

	AlAs $\delta_{top} < 0$	GaAs $\delta_{top} < 0$	AlAs $\delta_{top} > 0$	GaAs $\delta_{top} > 0$
AlAs $\delta_{bottom} < 0$				
GaAs $\delta_{bottom} < 0$	**c**			
AlAs $\delta_{bottom} > 0$	**a**		**e**	
GaAs $\delta_{bottom} > 0$		**b**	**d**	

Table 3.1: Table with the different combinations of two parameters: the sign of δ, and the materials of the layers forming a centrosymmetric unit cell. The table has a diagonal symmetry. The grey shaded cases are symmetric cases, where the top and bottom DBRs are identical.

Panels **a** to **d** of Fig.3.17 present four topological structures and panel **e** presents the Fabry-Perot resonator. On the left, there are schematics of the unit cells of each DBR, parametrized by δ_{top} and δ_{bottom}. Dark (light) colors represent GaAs (AlAs). The case presented in panel **a** of Fig.3.17 is the same as in Fig.3.5, where $\delta_{top} < 0$ and $\delta_{bottom} > 0$ and all the unit cells are centered around AlAs. The presence of interface modes at the center of the acoustic and optical bandgaps, at a frequency of 18.2 GHz and an optical wavelength of 920 nm (1.36 eV), is evidenced in the first and second columns, respectively. The third column displays the acoustic displacement $|u(z)|^2$ (black) and the optical intensity $|E(z)|^2$ (grey) of the topological interface modes. They exhibit a perfect mode overlap, with a maximum of intensity at the interface between the two DBRs. The last column plots the value of the integrand of the overlap integral for the photoelastic interaction $|E(z)|^2 p(z)(\partial u(\omega, z)/\partial t)$. The Brillouin cross-section and the optical Q-factor are written as an inset. The Brillouin cross-section is defined by the overlap integral:

$$\sigma(\omega) = \int |E(z)|^2 p(z) \frac{\partial u(\omega, z)}{\partial t} dz \tag{3.8}$$

The cross-section is determined by two conditions: (i) the overlap between the antinodes of the opto-phononic field $|E(z)|^2(\partial u(\omega, z)/\partial z)$ and the maxima of the photoelastic constant distribution $p(z)$ (ii) the relative sign of the opto-phononic antinodes in the regions where the photoelastic constant is non-zero. It is important to note that the antinodes with the maximum amplitude at the interface between the two DBRs is the main contributor to the overall cross-section. The integrand features signals composed either of double peaks (thick lines) or single peaks (thin lines). We can analyze the integrand by splitting it into quadrants (left/right DBR, positive/negative amplitude contributions).

The integrand shown in panel **a** of Fig.3.17 presents signals with positive amplitude composed of single peaks in one DBR and double peaks in the other. Only one DBR contributes with single peaks of negative amplitude. Practically, the peaks with negative amplitude compensate for half of the positive double peaks producing an overall signal with single peaked contributions of positive amplitude from both the DBRs.

In panel **b** of Fig.3.17, $\delta_{top} < 0$ and $\delta_{bottom} > 0$ and all the unit cells are centered around

GaAs. The concatenation of the two inverted DBRs results in the colocalized interface modes at the center of the acoustic and optical bandgap, 18.23 GHz and 920 nm, respectively. In that case the integrand is similar to the previous case in Fig.3.17**a**, resulting in an overall signal with positive single peaks.
In panel **c** of Fig.3.17, $\delta_{top/bottom} < 0$ with the top DBR centered on AlAs and the bottom DBR centered on GaAs. The interface modes in the acoustic and optical bandgap appear slightly off-centered at 18.18 GHz and 922.06 nm, respectively. The acoustic displacement $|u(z)|^2$ (black) and the optical intensity $|E(z)|^2$ (grey) of the topological interface modes are also colocalized. However, in contrast to cases **a** and **b**, the fields are not symmetric in both DBRs. The integrand shows only one DBR with positive double peaks, while it is formed by negative single peaks in both DBRs.
In panel **d** of Fig.3.17, $\delta_{top/bottom} > 0$ with the top DBR centered on AlAs and the bottom DBR centered on GaAs. This case presents colocalized interface modes in the acoustic and optical bandgap, at 18.26 GHz and 917.9 nm, respectively. The acoustic and optical fields, as well as the integrand show similar features as in case **c** of Fig.3.17.
Panel **e** of Fig.3.17 presents the case of a Fabry-Perot resonator made of $\lambda/4$ GaAs, $3\lambda/4$ AlAs DBRs enclosing a $\lambda/2$ GaAs spacer. The simulated reflectivities evidence an acoustic and an optical interface state at 18.2 GHz and 920 nm, respectively. The integrand presents only positive single peaks over the full structure.

We compare the Brillouin cross-section of the different structures to determine their Brillouin efficiency. Based on the profile of the integrand, we can divide the topological structures into two categories. First, cases **a** and **b** have an integrand which is positive in average. This gives an overall large Brillouin cross-section σ. The main difference between those two cases, is that in case **a**, the unit cells are centered around AlAs and in case **b** they are centered around GaAs. It suggests that the interface is formed by GaAs in case **a**, which contributes more to the Brillouin cross-section. Second, cases **c** and **d** have the positive and negative peaks of the integrand compensating each other, resulting in an overall small Brillouin cross-section σ.
The maximum cross-section ($\sigma = 2939$) is obtained in the case of the Fabry-Perot resonator presented in panel **e** of Fig.3.17. It is noteworthy that the topological resonator presented in case **a** has a cross-section $\sigma = 2841$ in the same range, almost matching the performance of a trivial resonator. The Brillouin cross-section would profit from the robustness intrinsic to the topological interface modes.

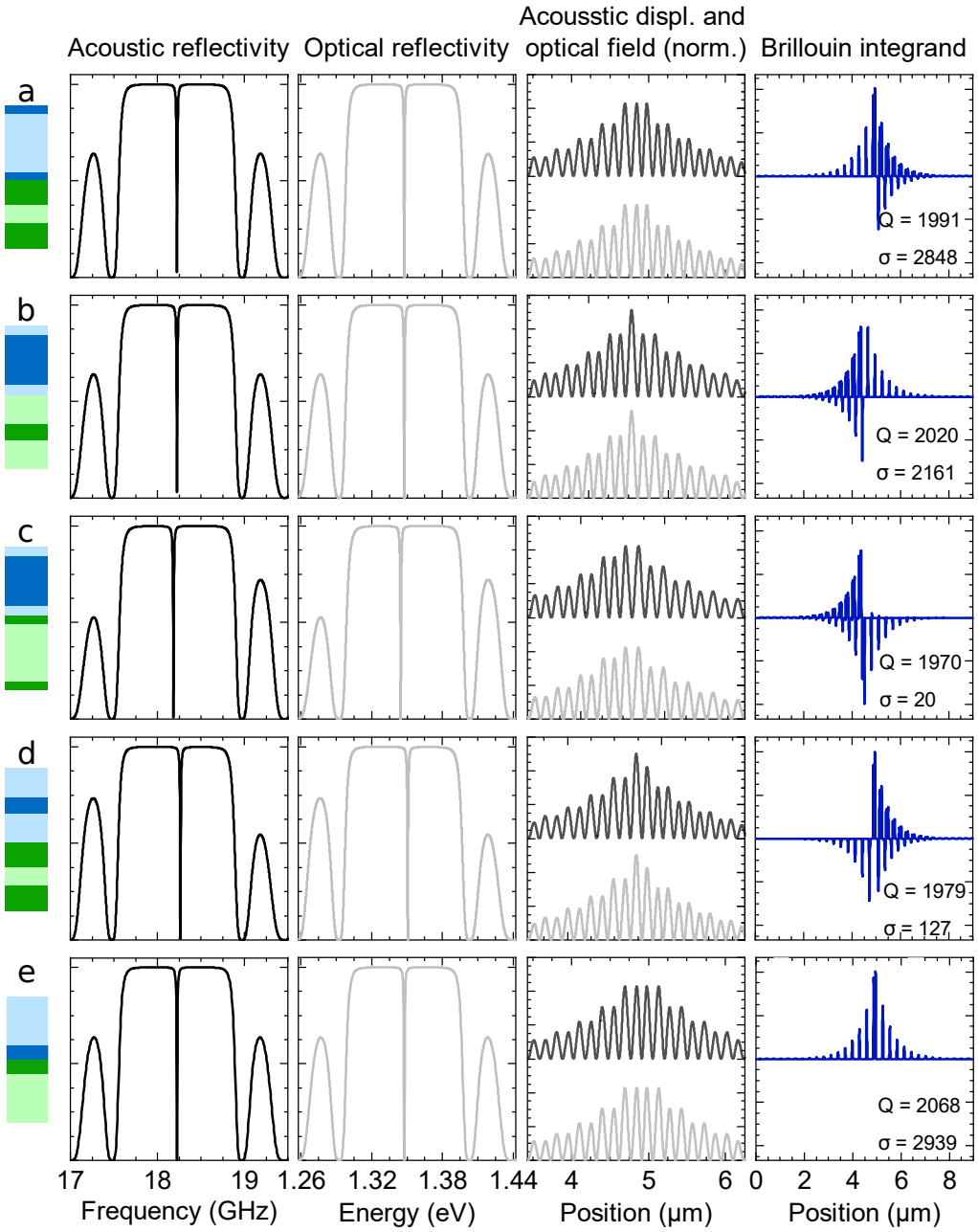

Figure 3.17: Comparison between different topological structures and a Fabry–Perot resonator. The structures are designed to confine an acoustic mode at ∼18.2 GHz and an optical mode at ∼1.36 eV (920 nm). Schematic of the unit cells at the interface are displayed on the left. Dark (light) colors represent GaAs (AlAs). For each structure, the simulated acoustic and optical reflectivities are plotted (first and second columns, respectively) showing an interface state around the middle of the bandgap . The spatial displacement pattern $|u(z)|^2$ (black) and the optical intensity profile $|E(z)|^2$ (grey) are displayed in the third column. They show a maximum at the interface between the two DBRs indicating colocalized topological interface states. The last panels display the integrand of the Brillouin cross-section.

3.4 Experimental measurements of the interface states

We experimentally validated some of the concepts discussed previously by experimentally studying a sample designed with the band inversion principle. The sample is engineered to simultaneously present an acoustic and an optical topological interface state as presented in section 1.4. The sample is composed of two concatenated DBRs to confine simultaneously an acoustic interface mode at 18.3 GHz and an optical interface mode at ∼920 nm. The top and bottom DBRs are charaterized by $\delta_{top/bottom} = \pm 0.5$. The DBRs are formed by 14 (16) periods of 65.1 nm/231.1 nm (195.5 nm/77.0 nm) $GaAs/Al_{0.95}Ga_{0.05}As$ layers for the top (bottom).
We experimentally evidenced the presence of an acoustic interface state in a topological acoustic resonator by making measurements in the time domain with a pump-probe experimental setup. The process of coherent phonon generation and detection in pump-probe spectroscopy is described in section 2.3. The complete experimental setup is depicted in reference [86]. We used a titanium:sapphire laser (Spectra Physics Tsunami) producing 3.4 ps long pulses at an 80 MHz repetition rate. A polarizing beam splitter splits the laser beam into pump and probe with powers of 3.2 and 1 mW, respectively. The pump beam passes through an acousto-optical modulator for synchronous detection, while the probe beam passes through a mechanical delay line to control the relative arrival time of the pump and probe on the sample. Both beams merge again at a polarizing beam splitter and are focused onto the sample with the same microscope objective with $20x$ magnification into a spot of 5.5 µm in a collinear geometry. Using a cross-polarization scheme, the reflected probe (modulated by the presence of phonons) is measured with a photodetector. A lock-in amplifier extracts differential reflectivity time traces.

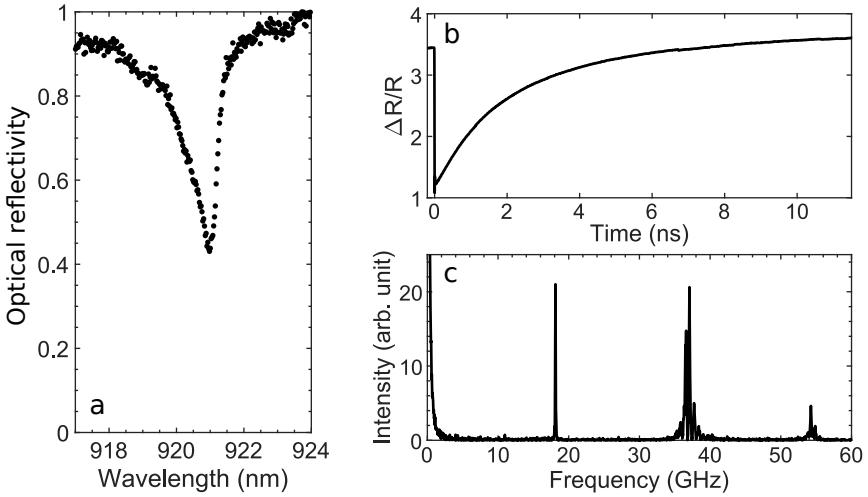

Figure 3.18: **a** Measured optical reflectivity spectrum. The dip at 921 nm features the optical interface state. **b** Time trace of the optical reflectivity obtained on a topological optophononic resonator. **c** Phononic spectrum obtained after Fourier transforming the reflectivity time trace. The peaks at 18 GHz and 54 GHz correspond to the fundamental and third harmonics of the interface state, respectively.

We measured the optical interface state with an optical reflectivity measurement.

The spectrum is obtained by illuminating the samples with a broadband source in a wavelength range over the cavity mode in a home-built reflectometer. The obtained spectrum is plotted in panel **a** of Fig.3.18. The dip at 921 nm corresponds to the optical interface mode in the first bandgap.
Panel **b** of Fig.3.18 displays the time dependent optical reflectivity of the probe beam. The fast change in reflectivity at 0 ns corresponds to the pump and probe impinging the sample together inducing a blueshift of the optical cavity mode. After 0 ns, the slope corresponds to the optical mode returning to equilibrium. After Fourier transforming the time trace, we obtain the spectrum shown in panel **c**. The peak at 18 GHz corresponds to the interface state of the designed aocustic topological resonator. The peaks at 54 GHz corresponds to the third acoustic harmonic for which there is also a band inversion around the bandgap. The broad peak at 37 GHz is the Brillouin mode of GaAs.

3.5 Conclusions

In this chapter, we theoretically presented a method to generate an acoustic interface state in a topological resonator, based on the band inversion principle. By changing the thickness ratio of GaAs and AlAs in the unit cell the symmetries of the modes around the bandgap change. An interface state is generated when two superlattices with inverted symmetries are concatenated. We extended this principle to create interface states in high-order bandgaps. By carefully adjusting the layer thicknesses in the unit cell we could generate multiple topological acoustic interface states robust against disorder in a broad frequency range. In addition, we simulated hybrid structures where interface states are created by combining two superlattices presenting bandgaps of different orders centered around the same frequency. We could then explore topological structures which are difficult to study in electronics or in optics due to the dispersion relations. The modes would be accessible in a Brillouin or pump-probe experiment.
Moreover, we showed that for superlattices designed at acoustic frequencies $\sim$18 GHz and optical wavelength $\sim$900 nm the inversion of symmetries of the edge-modes simultaneously occurs both in the optical and acoustic domains. This results in a simultaneous confinement of light and sound with colocalized optical and acoustic states.
We simulated a panel of topological optophononic resonators with different combinations of concatenated superlattices. We numerically discussed the Brillouin efficiency of those resonators and compared them with a Fabry-Perot resonator. We obtained a topological device comparable to a Fabry-Perot resonator in both quality factor and Brillouin efficiency. We experimentally evidenced the acoustic interface state in that sample with a pump-probe experiment and the optical interface state with a reflectivity experiment. In Chapter 4, we will study this sample in a Brillouin spectroscopy experiment. The topological devices with large cross-section presented in this chapter would also be adapted for measurements in a Brillouin spectroscopy experiment.

Main contributions:

- Topological interface nanoacoustic state engineering at high-order bandgaps
- Engineering of hybrid topological states, combining nanoacoustic superlattices with bandgaps of different orders
- Simultaneous confinement of NIR light and GHz sound in topological interface states

Chapter 4

Brillouin spectroscopy in planar multilayered optophononic microcavities

Brillouin spectroscopy is a non-invasive technique to investigate the mechanical properties of bulk materials and nanoscale systems. Brillouin spectra provide information about thermodynamic and acoustic properties of the studied system. The technique is used for a wide range of applications including geosciences, biology or fundamental physics [59, 60, 131].
In Brillouin spectroscopy, the frequency shift between the incident beam and the scattered signal induced by interactions between light and the mechanical waves in the medium is relatively small (up to a few GHz). In addition, the intensity of light inelastically scattered by acoustic phonons is approximately nine orders of magnitude weaker than the intensity of the elastic scattering [132]. Therefore, it is necessary to have a spectrometer which provides high resolution and effective extinction of the elastic scattering.
A significant step forward in Brillouin spectroscopy appeared with the development of the multi-pass Fabry-Perot interferometer (FPI) by Sandercock [133, 134]. It consists of a tunable Fabry-Perot interferometer in tandem with a monochromator. The scattered light passes multiple times through the FPI before entering the monochromator. Hence, the resolution and filtering rely on the finesse of the Fabry-Perot and the number of passages through it. Despite the high resolution spectra achieved, this technique requires long integration times due to the low intensity of the signal [84, 132].
In recent years, Brillouin spectroscopy has been widely developed in terms of measuring Brillouin frequency shifts in the range of 0.1 GHz to 1 THz with ultra-high resolution of 0.1 GHz [59, 64, 66–69]. Advanced Brillouin spectrometers are based on the virtually imaged phase array (VIPA) equipped with notch filters and on the scanning multiple pass tandem Fabry-Perot interferometers (TFPI). Motivated by the fact that Brillouin scattering offers the possibility to probe the mechanical properties of tissues and cells without contact, progress was made in Brillouin spectroscopy [60, 61, 135].
However, the performance of the developed techniques highly depends on the optimization of the optics and detectors to work at a fixed wavelength and frequency shift. This

intricate alignment limits the application of such Brillouin spectrometers in accessing the confined acoustic modes in tunable optophononic cavities, and novel schemes need to be developed [136].
Standard Raman spectroscopy techniques are used to study optical phonons with frequencies in the THz range, which are spectrally far from the laser line. Although these techniques are usually compatible with excitation sources over a broad optical wavelength range, the stray-light rejection is insufficient to observe Brillouin modes with frequencies as low as a few tens of GHz. Spectral filtering is also unsuitable due to the small spectral shift between the Brillouin signal and the laser. Thus, experimental techniques have been developed to access the acoustic modes of tunable optophononic cavities with Brillouin spectroscopy [31, 64]. In particular we are interested in experimental techniques based on the double optical resonance (DOR) of optical cavities [97, 136, 137]. Under this condition, the spatial filtering of the Brillouin signal with a single-mode fiber is achieved by exploiting the in-plane dispersion relation of the optical cavity. In addition, the Brillouin signal is enhanced by the optical cavity. Such setups are tunable and allow access to a wide range of acoustic frequencies.
In this chapter, we first discuss Brillouin spectroscopy experimental schemes based on the DOR condition. Then, we introduce a DOR-based Brillouin spectroscopy scheme to measure longitudinal acoustic phonons in the 20 GHz to 300 GHz range without optical wavelength restriction in planar optophononic cavities. The experimental scheme is based on the spatial filtering with a single-mode fiber permitted by the angular offset between the incoming laser and scattered signal. In addition, we use a tandem of an etalon and a double spectrometer to spectrally filter out the remains of the laser and increase the resolution of the spectra. We carried out experiments on two samples presenting topological acoustic interface modes. First, we tested the technique on a sample presenting an acoustic mode at 300 GHz. Finally, we further exploit the technique by measuring a more challenging sample with an acoustic mode at 18 GHz.

4.1 Double optical resonance-based experimental setup

In this chapter we present the DOR which we briefly described in Chapter 2. Due to their difference in energy, the incident and scattered beams are resonant with the optical cavity at different angles of incidence [46, 90, 97, 138]. As a consequence, the Brillouin signal can be spatially filtered. By appropriately tuning the angle of incidence of the incident laser θ_{in}, the Brillouin signal is scattered with normal incidence to the surface of the sample. At high frequencies, the angle of incidence is large, resulting in a better laser rejection than at lower frequencies. Due to the index of refraction of the cavity, the angle between the incident field and the Brillouin field is small inside the sample, resulting in an approximate backscattering configuration.

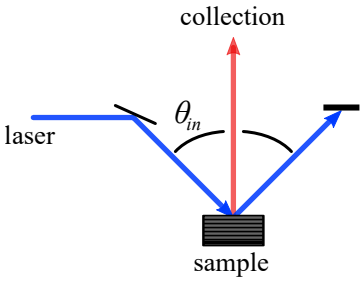

Figure 4.1: Experimental setup based on the DOR. The laser (blue) is incident on the sample with an angle θ_{in} while the Stokes Brillouin signal (red) is scattered at normal incidence.

Figure 4.1 displays a basic experimental setup based on DOR where the Stokes Brillouin signal (red) is collected at normal incidence and the reflected laser beam (blue) is blocked. Several works exploring the DOR in optical cavities to measure Brillouin signal were presented in references [97, 136, 137, 139]. DOR-based experimental setups enable enable the measurement of Brillouin modes which are otherwise inaccessible [97, 137]. By carefully tuning the angle of incidence of the laser defined as θ_{in}, the DOR condition can be modified to measure different Brillouin modes. It is possible to selectively enhance and collect the signal at a given frequency range. Fig.4.2, adapted from reference [137], shows two Brillouin spectra measured with different DOR conditions. The black spectrum is obtained by optimizing θ_{in} to access signals at 350 GHz scattered at normal incidence, while for the red spectrum, θ_{in} is optimized so the Brillouin modes at 700 GHz is scattered at normal incidence, resulting in a fundamental mode measured with low intensity. The laser rejection strongly depends on the angle of incidence of the laser.

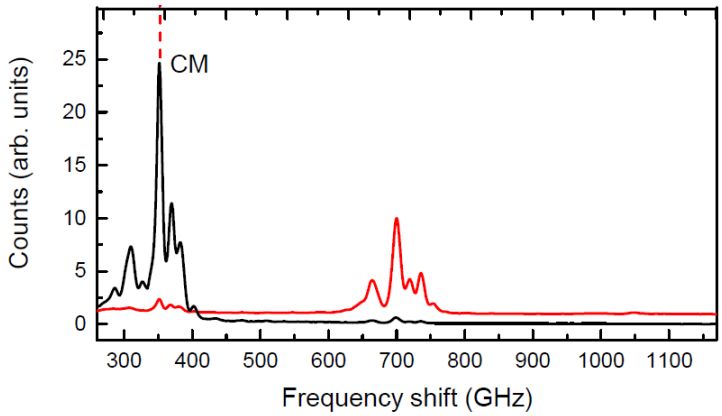

Figure 4.2: Brillouin spectra measured on an adiabatic cavity with a DOR-based experimental setup, reproduced from reference [137]. The black and red curves are measured with the DOR condition optimized for signals at 350 GHz and 700 GHz respectively.

A similar approach to the one presented in this chapter has already been addressed in reference [136]. The method exploits the DOR condition in the DBR-based optical cavity to enhance Brillouin scattering and filter the reflected laser. The incident laser is tuned with θ_{in} to remain in DOR while the signal is collected at normal incidence. In the collection path, a small aperture is used to filter out the Brillouin signal from the

reflected laser. In addition, there is a tandem of a gas-pressure controlled FPI and a triple spectrometer to access broadband acoustic frequencies [64]. With this technique, the spectra have a high resolution of 0.3 GHz in the few tens to few hundred GHz range. However, for modes at lower acoustic frequencies, the DOR condition still results in insufficient stray-light rejection.
In the following section, we propose an experimental setup based on the spatial filtering with a single-mode fiber permitted by the DOR condition to measure Brillouin signals in optophononic planar cavities in a large range of acoustic frequencies.

4.2 Spatial filtering by coupling to an optical fiber

To increase the signal to noise ratio we implemented a single-mode fiber in the collection path to spatially filter the Brillouin signal.

4.2.1 Experimental setup

Fig.4.3 displays a schematic of the developed experimental scheme. A collimated laser beam from a tunable continuous wave (cw) Ti:Sapphire laser (M2 SolsTis) operating at the wavelength in resonance with the fundamental optical cavity mode of the studied sample is used as an excitation source. First, the laser is coupled in and out of a single-mode fiber to obtain a beam with a well-defined Gaussian shape. The excitation laser beam passes through a mirror M mounted on a translation stage which allows controlling the path of the incident beam and thus the angle of incidence θ_{in}. The incident laser is focused on the sample with a spot diameter of 10 µm using a plano-convex lens (focal length, $f = 13$ mm). The sample is placed at room pressure and room temperature. The same lens is used to collect the scattered signal from the sample. The Brillouin signal is collected by a single-mode fiber (Thorlabs 780HP, core diameter 4.5 µm) with an input port consisting of an 11.17 mm focal length fiber coupler and NA of 0.13. The single-mode fiber allows us to spatially filter the Brillouin signal to attenuate stray-light elastically scattered in the setup and reject the reflected excitation laser. The signal emerges from the fiber through a collimator before passing through a removable etalon filter. Finally, it is analyzed with a double-stage spectrometer in additive mode (HRD 2 Jobin Yvon).

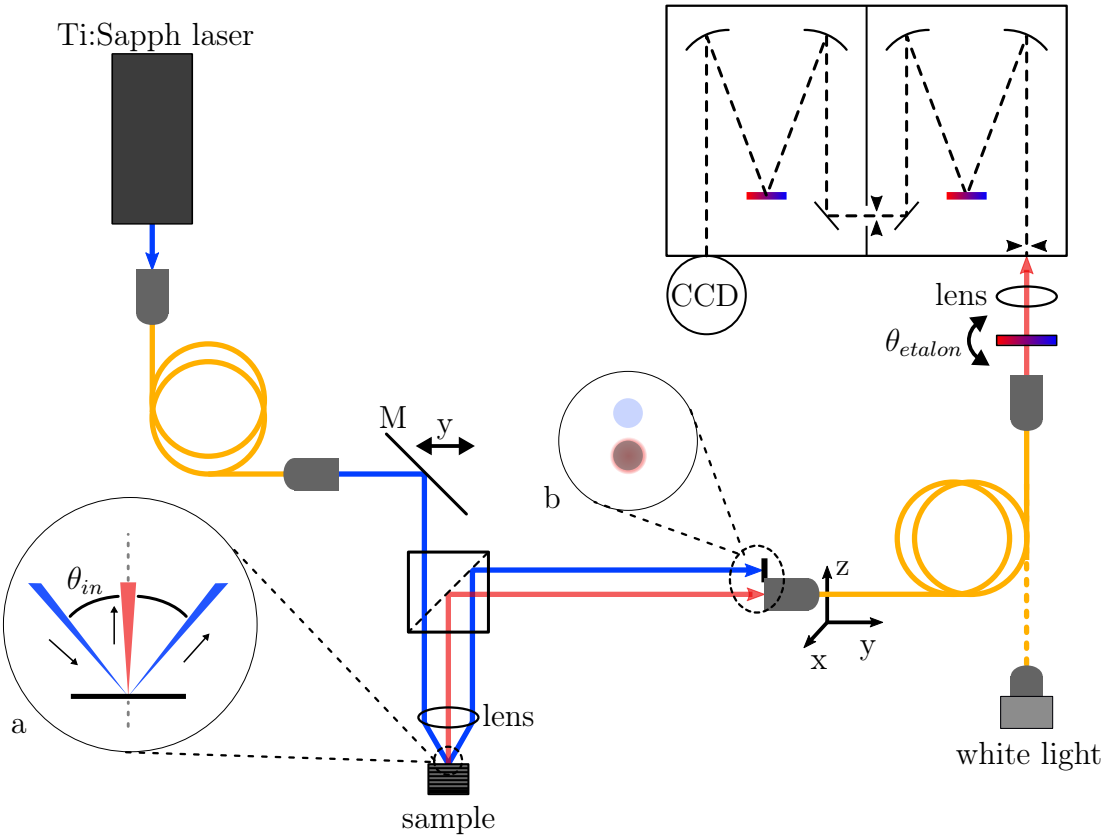

Figure 4.3: Schematic of the Brillouin spectroscopy setup. A tunable cw Ti:Sapphire laser excites the sample with an angle of incidence θ_{in}. The Brillouin signal is scattered at normal incidence through the same lens and collected into a single-mode fiber, which allows us to spatially filter out the laser. Then, it is sent into a double grating spectrometer through a tunable etalon. **a** Zoom-in on the excitation scheme on the sample. The Brillouin signal (red) is scattered with a Gaussian shape. **b** Schematic of the collection into the fiber.

The setup is designed in an approximated backscattering geometry with near-normal excitation. The measurements are performed in DOR condition to enhance the Brillouin scattering signal [90, 97, 99, 100]. We tune θ_{in} and the collection angle so that both beams remain in resonance with the cavity mode. The collection along the surface normal of the Brillouin signal resulting from the Stokes process is optimized by tuning θ_{in} of the laser away from the surface normal (see panel **a** of Fig.4.3). On the contrary, the configuration would be reversed in the case of anti-Stokes Brillouin scattering. For an incoming beam at normal incident, the anti-Stokes signal would be scattered with an angle θ. The double grating spectrometer is a combination of two monochromator chambers connected through an intermediate slit in additive mode (1200g/mm ruled grating). The slit between the two chambers allows us to choose the measured optical wavelength range and is used to lower the amount of stray-light generated inside the first chamber from the remaining excitation laser. The signal is then detected by a liquid nitrogen-cooled charge-coupled device (CCD) at the exit of the spectrometer (LN 100BR Detector Excelon Princeton instruments). The spectrometer provides an experimental resolution of 7 GHz which is measured as full width at half maximum (FWHM) of the laser source. We align the fiber port at the collection by mimicking the spatial

mode of the Brillouin signal with the reflected excitation laser. That is, the movable mirror M is placed such that the laser reaches the sample at normal incidence and the reflected laser is coupled into the collection fiber, as shown in panel **a** of Fig.4.4. Then, mirror M is displaced such that the laser is again incident with an angle θ_{in} for the spectroscopy measurement, resulting in Stokes Brillouin signal scattered at normal incidence (see Fig.4.4**b**). For Brillouin emission at normal incidence, the scattered signal has a Gaussian shape. Therefore, the overlap of the scattering pattern with the fiber NA results in a large collection efficiency (see panel **b** of Fig.4.3).

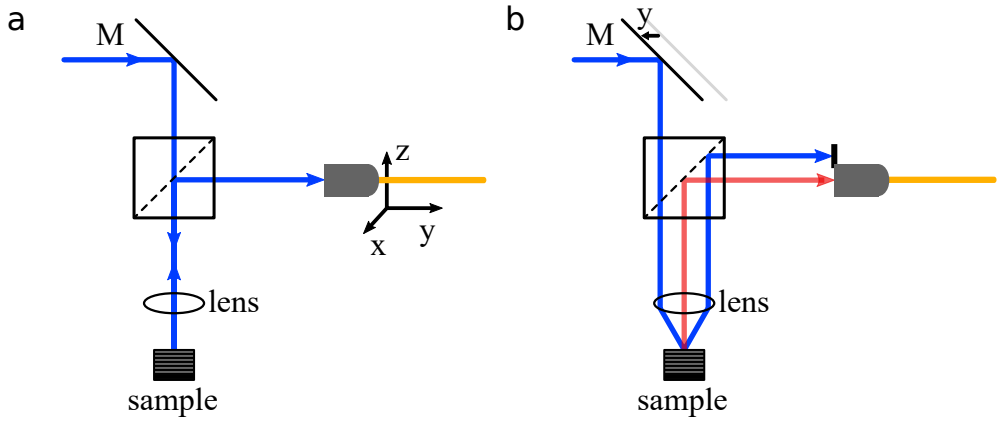

Figure 4.4: Schematic of the alignment process. **a** The reflected laser at normal incidence is coupled into the collection fiber. **b** Mirror M is displaced to couple the resonant Brillouin scattering into the collection fiber.

4.2.2 Measurements on a hybrid optophononic resonator

We employed the technique described in the previous section to study a sample designed with the band inversion principle described in Chapter 3. The sample studied in this section is a topological acoustic planar cavity presenting an acoustic interface mode at 300 GHz embedded into an optical Fabry-Pérot cavity. The sample was grown by molecular beam epitaxy on a (001) GaAs substrate by the team of Aristide Lemaître in the C2N facilities. It is grown with a spatial gradient which leads to position-dependent resonance wavelengths. The sample is made of two optical DBRs enclosing an optical spacer with an optical path-length of 2.5λ at a resonant optical wavelength of around 910 nm. The optical spacer is composed of two concatenated acoustic DBRs with different topological phases. The top (bottom) optical DBR is made of 14(18) periods of 65.1 nm/76.3 nm $Al_{0.95}Ga_{0.05}As/Al_{0.1}Ga_{0.9}As$. The acoustic top (bottom) DBR is formed by 16 periods (each) of 8.7 nm/8.4 nm (7.5 nm/10.0 nm) GaAs/AlAs layers, see Fig.4.5.

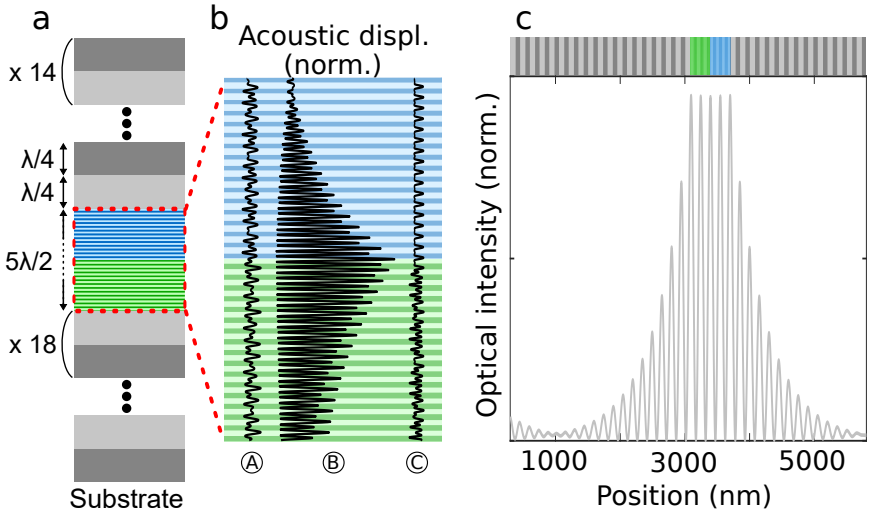

Figure 4.5: **a** Schematic of the sample. A topological acoustic resonator is embedded in an optical Fabry-Pérot cavity. Two acoustic DBRs with $\delta_{top} = -0.1$ and $\delta_{bottom} = 0.1$ are concatenated. Dark (light) colors represent GaAs (AlAs). **b** Spatial displacement pattern $|u(z)|^2$ of the topological state at 260 GHz, 300 GHz and 335 GHz in the acoustic structure (A, B and C, respectively). **c** Optical profile $|E(z)|^2$ of the confined optical mode in the full structure.

We measured the optical reflectivity as a function of the mirror M position, see panel **a** of Fig.4.6. We experimentally obtained the dispersion relation of the cavity. For each reflectivity measurement, the coupling at the collection is optimized. The Brillouin shift of 300 GHz acoustic phonons corresponds to a wavelength difference of ∼0.8 nm between the laser and the scattered signal wavelengths (green arrow). For an excitation angle $\theta_{in} = 13°$ (i.e. a 3 mm displacement of the mirror), the Brillouin signal at 300 GHz is scattered at near-normal incidence. Under this condition, the Brillouin signal is scattered with a Gaussian shape defined by the optical mode. At this angle, the optical cavity mode is centered around 910 nm, with FWHM of ∼0.4 nm, giving a Q-factor of ∼2300.

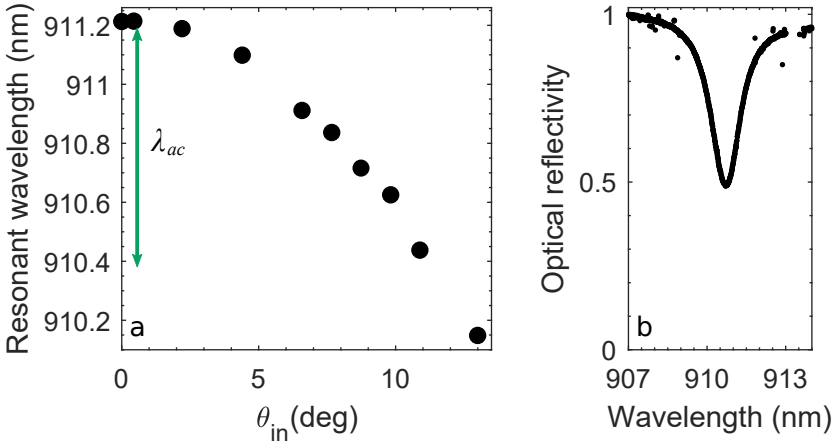

Figure 4.6: **a** Measured in-plane dispersion relation when moving the mirror M. The vertical green arrow show the acoustic shift between the laser and Brillouin scattering for 300 GHz phonons. **b** optical reflectivity spectrum measured for an incident angle $\theta_{in} = 7°$, which corresponds to a 2 mm displacement of the mirror.

The sample is resonantly excited with a laser tuned at 909.45 nm with an incident power of 16 mW measured before the lens. The spatial gradient of the sample under study enables us to maximize the coupling of the scattering signal with the optical cavity by changing the sample position. The combination of θ_{in} and sample position is set to obtain the maximal spectral coupling of the excitation and scattered Brillouin signal with the optical cavity mode. Fig.4.7 presents the experimental Stokes Brillouin signal acquired with the fiber filtering technique described above without inserting an etalon in the collection path. The integration time is 8 s. The peak at 300 GHz corresponds to the first interface mode between the two acoustic DBRs. The two peaks at ∼260 GHz and 335 GHz correspond to modes propagating in the acoustic DBRs, as shown in Fig.4.5 [31]. The peaks at lower frequencies <250 GHz correspond to acoustic modes propagating in the full optical structure.The peak at 37 GHZ is related to the Brillouin mode arising due to the scattering from the GaAs substrate. The peak at low frequency <20 GHz is due to laser light diffracted by the edge of the slit inside the spectrometer.

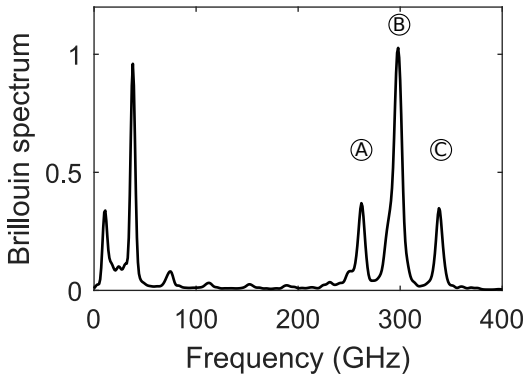

Figure 4.7: Brillouin spectrum of a hybrid topological optophononic cavity measured in DOR condition with θ_{in} optimized to enhance the mode at 300 GHz. The peak at 300 GHz corresponds to the interface mode between the two acoustic DBRs.

4.3 Spectral filtering by an etalon filter

To increase the resolution of the Brillouin spectra and to further improve the laser filtering, we implemented an etalon filter in the collection path.

4.3.1 Experimental technique

In the collection path, in front of the spectrometer, we can now insert an etalon (see Fig.4.3). It has two primary purposes in our experiment: first, it increases the spectral resolution beyond the resolution of the double spectrometer. Second, it improves the rejection of scattered laser light [64, 136].
Before entering a double-grating spectrometer through a slit, the fiber-coupled signal passes through a free-space removable etalon. Our setup consists of a double spectrometer and a simple etalon in tandem which permits us to reconstruct a Brillouin spectrum with high spectral resolution compared to using a single spectrometer. The etalon is

mounted on a motorized rotation stage on a magnetic base and can be easily inserted or removed. We rotate the etalon to vary the angle of incidence of the collected beam and thus tune the transmission modes of the etalon. The Brillouin spectrum is a reconstruction from a series of measurements where the modes of the etalon are tuned over the full wavelength range. The broadband white light source is used to get the position of the transmission lines of the etalon (see Fig.4.3).
The etalon has a linewidth of 2 GHz and a free spectral range (FSR) of 60 GHz at a peak transmission of 83%. Panel **a** of Fig.4.8 shows a transmission spectrum of the etalon at normal incidence acquired using a broadband white light source. The position of each transmission line is extracted and marked with a blue dot. By rotating the etalon with respect to the beam, the transmission lines move and span all the frequencies to cover the FSR (see panel **b** of Fig.4.8, blue dots). To cover the full FSR, the rotation angle of the etalon θ_{etalon} goes from normal incidence to $\theta_{etalon} = 1.8°$ with a step of 0.02°. The position of the transmission lines follows a parabola whit the change in θ_{etalon}, in a similar way to that of the dispersion relation of an optical Fabry-Perot cavity. For each transmission line in the spectrometer window, there is a corresponding parabola. However, the displacement of the transmission line is limited by the resolution of the spectrometer and pixel size of the detector. Hence, the displacement of the transmission lines progresses in a stepwise fashion. To smooth this behavior and increase the resolution, each transmission line displacement is fitted with a parabola (see panel **b** of Fig.4.8, red lines).

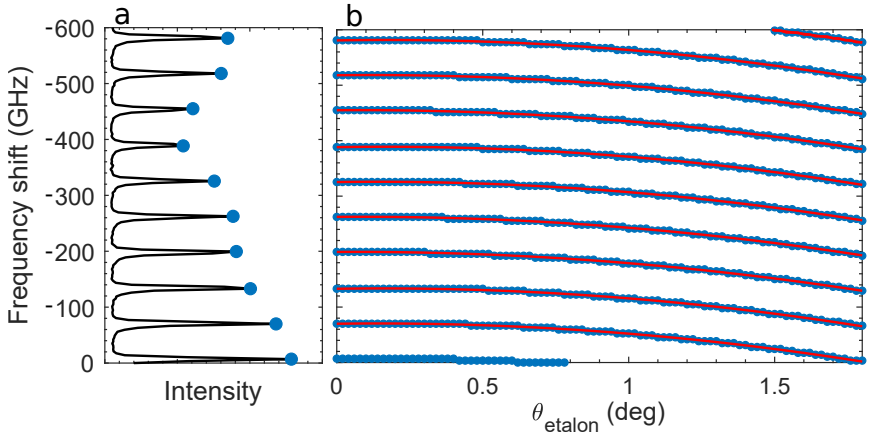

Figure 4.8: **a** Transmission line spectrum measured using broadband white light at normal incidence. Displacement of the etalon transmission lines (blue dots) as a function of θ_{etalon} fitted with parabola (red lines).

Once the displacement pattern of the transmission lines of the etalon is known, the Brillouin scattering signal is acquired in a similar way. Thus, for each position of the transmission lines, a Brillouin spectrum is acquired through the etalon. Panel **a** of Fig.4.9 shows a Brillouin spectrum acquired through the etalon at normal incidence (black line) superimposed with the transmission lines of the etalon (dashed grey). Panel **b** of Fig.4.9 displays the Brillouin spectra acquired for each angle θ_{etalon}. As soon as they match with the transmission line of the etalon, Brillouin peaks appear in the measured spectra. Note that the strongest peaks are not entirely rejected between two

transmission lines of the etalon, particularly the Brillouin peaks at 40 GHz and 300 GHz and intense stray-light close to the laser line.
When the transmission line of the etalon coincides with the laser line, the laser rejection is not as efficient. Therefore the background intensity increases and we can see parasitic peaks appearing corresponding to $\theta_{etalon} \sim 0.75°$ in panel **b** of Fig.4.9.

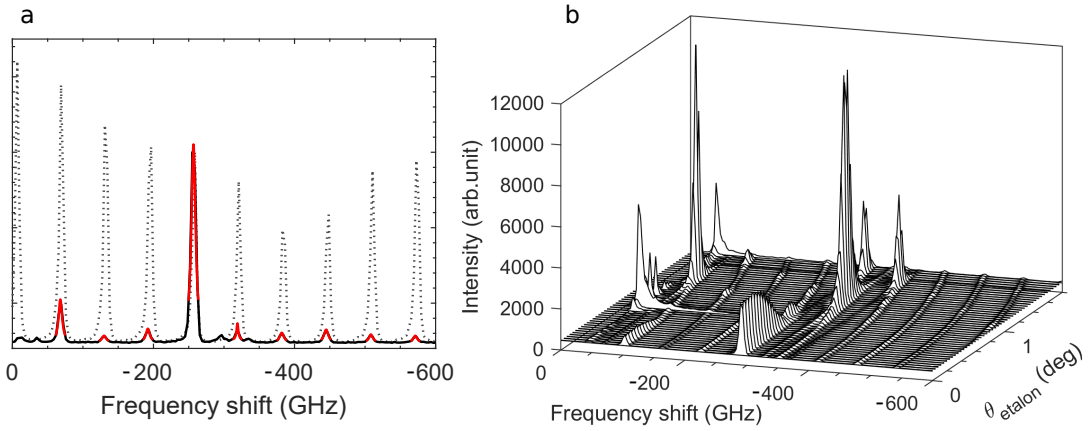

Figure 4.9: **a** Data analysis using an etalon (dashed grey) Transmission line spectrum measured using broadband white light at normal incidence. (black) Brillouin signal acquired through the etalon at normal incidence. (red) Lorentzian fit of the Brillouin spectrum. **b** Brillouin signal acquired through the etalon as a function of θ_{etalon}.

The last step to obtain a reconstructed Brillouin spectrum is to process the acquired data. The Brillouin spectra acquired through the etalon are fitted with Lorentzian centered at each transmission line of the etalon (see red lines in Fig.4.9**a**). It allows us to reduce the stray-light due to the laser reflection on the sample and the optics. Then, the Lorentzian fits are integrated into areas with a window of 17 GHz centered on the transmission lines. Each integral is then associated with a position of the transmission line at a given angle. Therefore, for each transmission line, we can associate a piece of the Brillouin spectrum. By concatenating all the pieces, we are able to reconstruct a complete Brillouin spectrum, with higher resolution and laser filtering. This technique is mainly limited by the stability of the signal over time. An intense stray-light would increase the noise of the measurements making the processing of the data and the fitting with Lorentzian curves difficult. Thus, the technique strongly relies on filtering the signal with the single-mode fiber. Despite the limitations, the resolutions and stability are sufficient to measure Brillouin spectra with frequencies in the few tens to few hundred of GHz range.
The acquisition time over the full FSR ranges from 10 to 20 minutes. It depends on the step-size, the duration of rotation of the mount, and the integration time for each spectrum which is of a few seconds.

4.3.2 Measurements on a hybrid optophononic resonator

The results presented here are obtained from the same sample as in section 4.2.2. The sample is a topological acoustic planar cavity presenting a confined acoustic mode at 300 GHz embedded into an optical Fabry-Pérot cavity.
Figure 4.10 is a comparison between the spectrum obtained with only the fiber filtering (grey dashed line) presented in Fig.4.7, with a spectrum obtained after reconstruction of the etalon measurements (black dots) and a calculated Brillouin cross-section using a photoelastic model and transfer matrix method for the structure embedded in GaAs. The spectra measured with the etalon are obtained by integrating 0.3 s at each angle of incidence of the etalon. The calculated spectrum (red solid line) in Fig.4.10 is convoluted with a Gaussian function with a linewidth of 2 GHz to account for the linewidth of the etalon to match the resolution of the experimental spectrum. The measured acoustic modes with small oscillations in the experimental spectrum are consistent with the calculations. The peak at 37 GHz also agrees well with our calculations. The weak peak with a blue cross on top is a parasitic line from the laser. When the laser line is transmitted through a transmission line of the etalon, the laser rejection is insufficient. Therefore, parasitic lines corresponding to the increase of the background appear with a spacing corresponding to the FSR of the etalon. The intensity of the background reduces with the distance to the laser line, resulting in only one visible parasitic line.
At high frequencies, the etalon mainly contributes to increasing the resolution. The improvement of the resolution is visible for the peak at $\sim$255 GHz where we are able to resolve the shoulder of the peak. At lower frequencies $\sim$ 40 GHz, the primary role of the etalon is the laser-filtering in order to obtain a better signal:background ratio (SBR). Without the etalon, the signal:background ratio is 24, while it is 162 with etalon. It results in an almost sevenfold improvement.

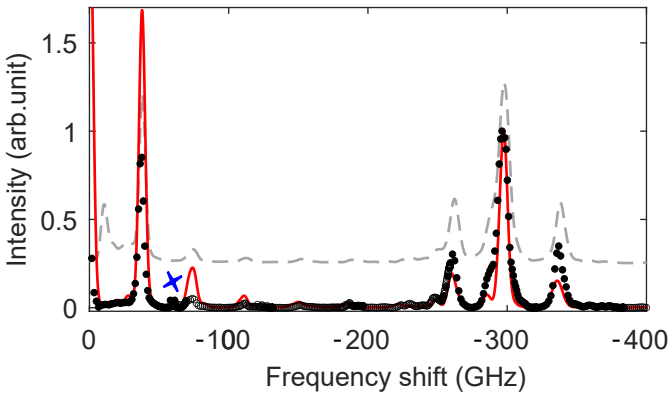

Figure 4.10: Brillouin spectra. The calculated (red solid) and experimental (black symbols) Brillouin spectrum with the etalon. The Brillouin spectrum measured without etalon (grey dashed line) is shown with an offset of 0.25 for comparison. The peak at 60 GHz marked with a blue cross is parasitic light from the laser.

4.4 Unveiling the 5−100 GHz range

We further exploit the experimental setup presented above by working with low acoustic frequency in the tens of GHz range. We present the modification of the setup we implemented to optimize the detection in DOR.

4.4.1 Angular filtering adjustments

Generally, for an incoming beam with an incident angle θ_{in}, the Stokes signal is scattered with an angular offset θ from the incident beam, with $\theta \leq \theta_{in}$. For phonons in the 18 GHz range, the energy shift is significantly smaller than in the previous case. Therefore, while keeping $\theta_{in} = 13°$ constant, the outgoing signal has $\vec{k}_{//} \neq 0$ and is scattered with an angle ($\theta < \theta_{in}$). Hence, the Brillouin signal is scattered with an annular shape, as represented in panel **a** of Fig.4.11.

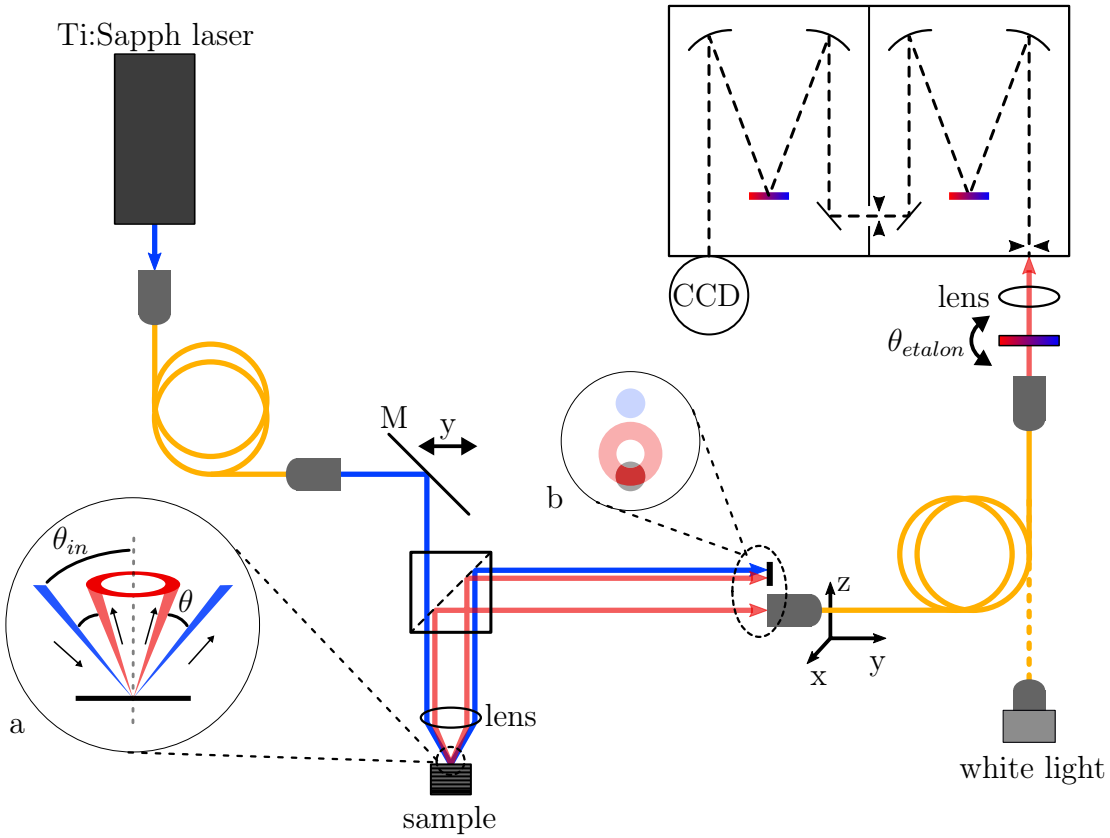

Figure 4.11: Schematic of the Brillouin spectroscopy setup. A tunable cw Ti:Sapphire laser excites the sample with an angle of incidence θ_{in}. The Brillouin signal is scattered with an angular shift θ through the same lens and collected into a single-mode fiber, which allows us to spatially filter out the laser. Then, it is sent into a double-grating spectrometer through a tunable etalon. **a** Zoom-in on the excitation scheme on the sample. The Brillouin signal (red) is scattered with a ring-like shape. **b** Schematic of the collection into the fiber. Only a part of the Brillouin annular shape is collected.

As a result of the annular shape induced by the small angular offset $\theta < \theta_{in}$, the distance between the reflected laser beam and the collected Brillouin signal can be maximized. The scattered signal is collected on the opposite of the reflected laser beam, thus on the same side of the normal as the incoming laser beam (see experimental setup in Fig.4.11). This results in a better rejection of the reflected laser beam. In this configuration, the angular filtering selects a circular section from the annular Brillouin radiation pattern (see inset **b**) with a NA$= 0.13 \times 11.17/13 = 0.11$. For the experimental quality factor and angle of incidence, we estimate a maximum Brillouin collection efficiency of 14% inside the fiber, which corresponds to the percentage of the ring selected with the collection fiber. Similarly to the previous case, the collection fiber is aligned by mimicking the spatial mode of the Brillouin signal with the reflected excitation laser. The laser is injected under an angle of incidence $\theta - \theta_{in}$ and the reflected laser is coupled into the collection fiber (see panel **a** of Fig.4.12). Then, by translating the mirror M back such that the laser is again incident at $\theta_{in} = 13°$, we collect Stokes Brillouin signal with an angle $\theta_{in} - \theta$ (see panel **b** of Fig.4.12). A careful pre-alignment of the objective lens and mirror M ensures that the laser focus maintains its position on the sample while translating mirror M.

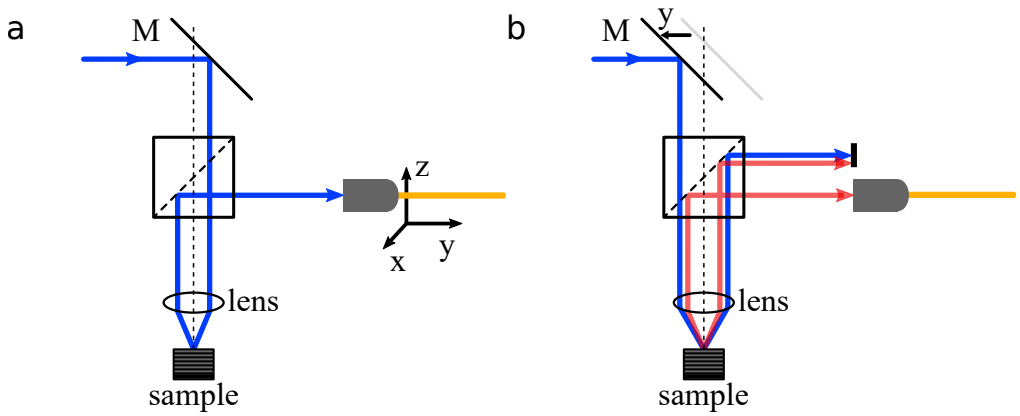

Figure 4.12: Schematic of the alignment process. **a** The reflected laser coupled into the collection fiber for laser incident at $\theta - \theta_{in}$. **b** Mirror M is displaced to couple the resonant Brillouin scattering into the collection fiber.

Note that, in order to realize the DOR condition, we tune θ_{in} by displacing the mirror M. For ∼18 GHz phonons, it is also possible to rotate the sample, keeping the mirror M at the zero-position. Consequently, both the incident laser and the scattered Brillouin signal would pass close to the center of the lens, avoiding chromatic aberrations. This configuration is shown in Fig.4.13.

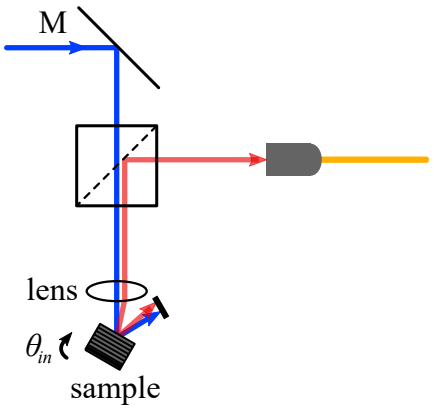

Figure 4.13: Schematic of the DOR-based setup with the sample rotated. The resonant Stokes Brillouin scattering is coupled into the collection fiber.

4.4.2 Experimental results on a topological optophononic cavity.

The sample studied in this section is a topological optophononic cavity presenting colocalized optical and acoustic interface modes. The design of this sample is discussed in section 3.3. The sample is composed of two DBRs concatenated to confine simultaneously an acoustic interface mode at 18.3 GHz and an optical interface mode at ∼920 nm. The DBRs are formed by 14 (16) periods of 65.1 nm/231.1 nm (195.5 nm/77.0 nm) GaAs/$Al_{0.95}Ga_{0.05}As$ layers for the top (bottom). The schematic of the structure is displayed in panel **c** of Fig.4.14. The quality factor of the optical cavity is around 2300. Fig.4.14**a** displays the measured dispersion relation of the optical cavity. The Brillouin shift of 18.3 GHz acoustic phonons associated with a difference in optical wavelength of

$\sim$0.05 nm is identified with a green arrow in the dispersion relation. Due to the small angular shift induced by the wavelength detuning, the scattered signal is no longer collected at normal incidence to satisfy the DOR condition in the case where $\theta_{in} = 13°$. Panel **b** of Fig.4.14 shows the acoustic reflectivity for $\theta_{in} = 2.3°$. For the Brillouin spectroscopy measurements, the sample is resonantly excited at a laser wavelength of 924.72 nm, with an excitation power of 6.3 mW. The excitation laser is kept with the same angle of incidence, $\theta_{in} = 13°$. As a consequence, the Brillouin signal is scattered with an annular shape as shown in Fig.4.3**a**. The signal is collected with $\vec{k}_{//}$ in the opposite direction from the reflected laser, increasing the distance between the reflected laser and the signal collected into the fiber. This enables better fiber-based angular filtering. Even though the Brillouin signal is scattered with an annular shape, only a small part of the ring is collected. The experimental Brillouin spectrum presented here is obtained with the experimental configuration represented in Fig.4.13. The transmission lines of the etalon are scanned over the full FSR using a step of 0.01°.

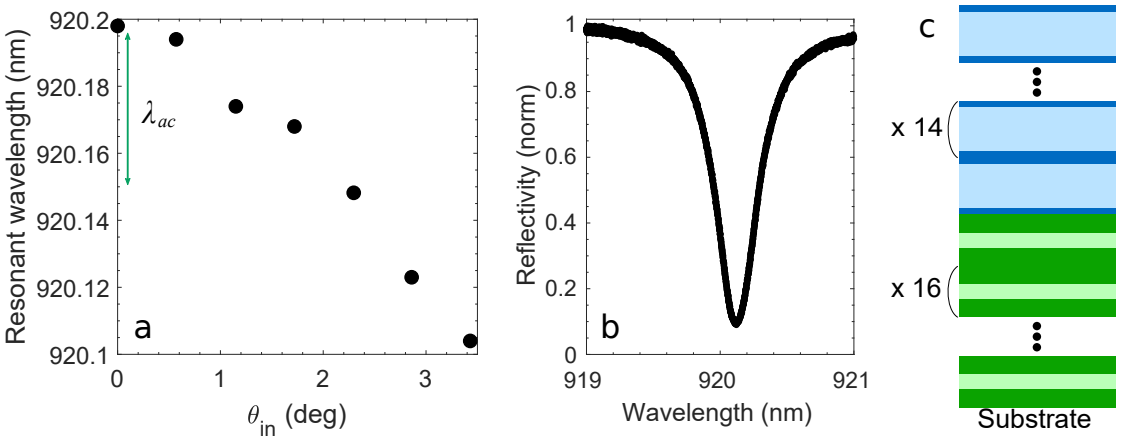

Figure 4.14: **a** Measured in-plane dispersion relation when moving the mirror M. The green arrow indicates the wavelength shift induced by acoustic phonons at 18.3 GHz. **b** Optical reflectivity spectrum measured with an objective lens with $f = 100$ mm. for an incident angle $\theta_{in} = 2.3°$. **c** Schematic of the sample. Two GaAs/AlAs DBRs with $\delta_{top} = -0.5$ and $\delta_{bottom} = 0.5$ are concatenated. The topological resonator simultaneously confine light and sound at the interface.

Fig.4.15 displays the measured Stokes Brillouin spectrum without and with etalon in the collection path (grey dashed line and black dots, respectively), together with the calculated spectrum convoluted with a Gaussian of 2 GHz linewidth (red solid line). The spectrum without etalon is obtained after integrating 10 s, while each spectrum measured with the etalon is obtained by integrating 4 s. The peak at 18.3 GHz is the first interface mode we observe in DOR condition. The peaks at 56 and 90 GHz correspond to the third and fifth harmonic of the acoustic interface mode. The acoustic displacement at the interface for the three acoustic harmonics is displayed in an inset in Fig.4.15. Similarly to the previous sample, the peak at 37 GHz is related to the Brillouin mode of the GaAs substrate. Likewise, the parasitic line coming from the increase of the background when the laser line crosses the transmission line of the etalon is identified at 60 GHz with a blue cross on top. The calculated spectrum obtained for the structure is in complete agreement with the experimental result. For the Brillouin spectrum acquired

without etalon (grey dashed line), the peak at 18.3 GHz is already visible due to the efficiency of the fiber-filtering scheme. However, the peak is slightly shifted due to the presence of the laser background. In addition, an intense peak appears close to the laser line at a frequency < 10 GHz. This peak is due to laser light diffracted by the edge of the slit inside the spectrometer. When we insert the etalon in the collection path, the laser filtering before entering the spectrometer is improved. Therefore, the background and the peak at low frequency disappear, improving the contrast of the mode at 18.3 GHz. The SBR for the peak at 18.3 GHz resulting in SBR = 0.65 without and SBR = 2.53 with etalon, i.e., in a fourfold improvement.

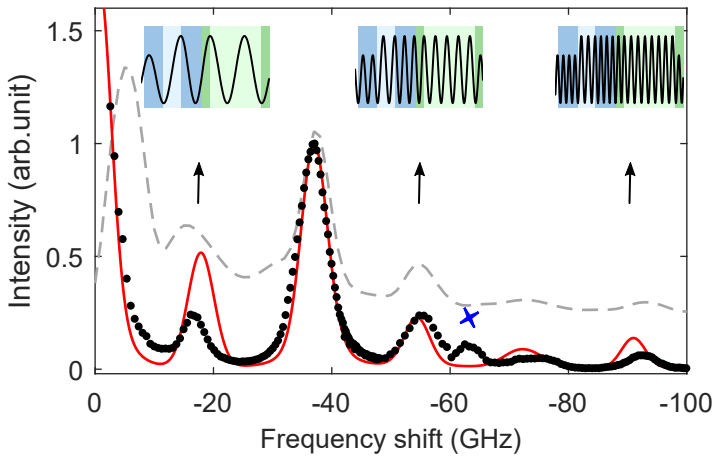

Figure 4.15: The experimental Brillouin spectra without (grey dashed line with an offset of 0.25) and with etalon (black symbols) along with the calculated spectrum (red solid). The peak at 63 GHz marked with a blue cross is parasitic light from the laser. Inset: The acoustic displacement for the 1^{st}, 3^{rd} and 5^{th} harmonic at the interface.

4.5 Conclusions

We experimentally evidenced the presence of acoustic interface states in topological cavities by means of Brillouin spectroscopy. The technique developed enables access to acoustic modes ranging from 18 to 300 GHz. We benefit from the double optical resonance in multilayer optical cavities to filter out the laser with a single-mode fiber and improve the signal-over-noise ratio. This technique shows its full potential at lower acoustic frequencies. In that case, both the laser and the Brillouin signal are tuned with an angle of incidence. In this way, we can achieve better filtering of the signal. Moreover, the use of an etalon before the spectrometer enables to extinguish most of remaining stray-light and to increase the resolution of the Brillouin spectra to a resolution of $\sim$2 GHz adapted to our experiment. The use of the etalon improves the extinction ratio by a factor of seven at 40 GHz and a factor of four at 18.3 GHz.
The signal/noise ratio could be further improved by using annular apertures similar to the work presented in reference [136]. Moreover the resolution could be enhanced by changing the traditional Fabry-Perot etalon at the collection with a notch filter, a gas-pressure controlled Fabry-Perot interferometer or a Michelson interferometer [64, 140]. In addition, the reconstruction of the Brillouin spectrum could be optimized by

always integrating the signal convoluted with the white light spectrum around the fixed position of the Brillouin peaks.
The high resolution and filtering obtained with this method could also be valuable to probe any change in the density of acoustic modes by probing the phonon sideband of quantum emitters coupled to an acoustic cavity. Hence, the proposed experimental scheme provides an accessible and versatile platform for exploring cavity optomechanics and phonon lasing at broadband acoustic frequencies.
This approach could also be applied to filter out the signal in forward Brillouin scattering. However, this method is limited to measurements on planar cavities due to the strong modification of the optical dispersion relation of the cavity in three-dimensional objects. Moreover, there is a limitation imposed by the light diffraction by micrometric sized objects. An experimental method based on the diffraction pattern mismatch between the reflected laser and Brillouin scattering to study micropillar resonators is presented by Esmann et al. in reference [31]. This technique enables measuring high frequency acoustic modes of 3D micropillars ($\sim$ 300 GHz). In the next chapter, we develop an experimental strategy to access 18 GHz confined acoustic modes in micropillars with Brillouin spectroscopy based on polarization filtering.

Main contributions:

- Implementation of spatial filtering with a single-mode fiber in DOR-based Brillouin spectroscopy setup to measure 10-500 GHz phonons
- Measurement of confined acoustic modes at 18 GHz in planar optophononic cavities with Brillouin spectroscopy

Chapter 5

Optophononic Fabry-Perot resonators based on 3D micropillars

By means of Brillouin spectroscopy adapted to planar systems, we have studied the confinement of high-frequency longitudinal acoustic phonons in one-dimensional GaAs/AlAs multilayered devices. The same planar structures can be etched into three-dimensional structures with lateral sizes of a few micrometers. These micropillar resonators can work both in the optical and acoustic regime resulting in a promising platform to study optomechanics at high frequencies [30, 50]. In this chapter, we present a method to measure Brillouin scattering signal at frequencies of a few tens of GHz in these optophononic micropillars. A method for measuring Brillouin scattering signal at frequencies ∼300 GHz in micropillars has already been presented in reference [31]. The technique is based on the diffraction pattern mismatch between the reflected laser and Brillouin scattering to filter the signal. However, the laser rejection is not sufficient for lower frequencies. So far, measurement of confined acoustic modes at frequencies ∼20 GHz in micropillars has only been achieved through pump-probe measurements [30, 65]. We propose an experimental scheme based on the control of polarization of the Brillouin scattering signal to access the confined acoustic mode with frequencies in the 20 GHz range in micropillars. The polarization control in spontaneous Brillouin scattering has seldom been explored in polarization-sensitive devices. Only recently, the control of the polarization state in stimulated Brillouin scattering has been reported in birefringent photonic crystal fibers, polarization maintaining fibers, and nanofibers [114, 141, 142].

In this chapter, we show how we can control the polarization selection rules of spontaneous Brillouin scattering in micropillar resonators with elliptical cross-sections. The principle we exploit here is similar to birefringent materials for which light can suffer an energy-dependent rotation of polarization determined by the thickness of the material [143, 144]. In the case of micropillars, the rotation of polarization is determined by the ellipticity of the cross-section.

We experimentally and theoretically explore the polarization dependence of Brillouin scattering, to reach a situation where the Brillouin signal and the reflected laser have different polarization states. In this way, almost background-free spontaneous Brillouin scattering spectra can be efficiently measured in a cross-polarization scheme.

The optical properties of micropillars with elliptical cross-sections have already been

extensively studied [145, 146]. First, we introduce the optical properties of GaAlAs micropillars with circular and elliptical cross-sections. Then, we discuss how we could bend the Brillouin scattering selection rules in polarization-sensitive devices. Finally, we present experimental results and simulations obtained by optimizing different parameters, such as the laser wavelength, the ellipticity of the cross-section and the polarization state of the laser.

5.1 3D optical confinement in micropillars with circular cross-sections

In this section, we present a theoretical model to describe the three-dimensional confinement of light in Fabry-Perot micropillars. This model allows us to explain the mechanics of three-dimensional optical confinement in cylindrical resonators with a circular cross-section. This model is fully explained in reference [147].

5.1.1 Guided optical modes in micropillars with circular cross-sections

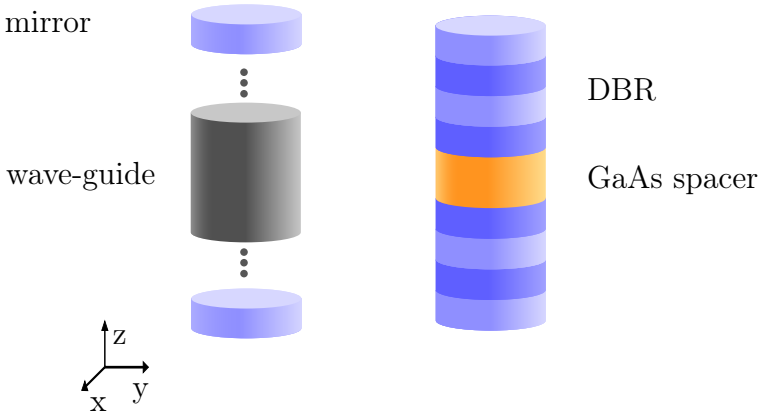

Figure 5.1: **a** Infinite waveguide with a cylindrical cross-section. We then insert two mirrors at the end of the cylindrical structure. **b** Schematic diagram of a micropillar.

First, let us consider an infinite dielectric GaAs waveguide with a circular cross-section. To obtain the confined optical modes, the Maxwell equations are solved in a cylindrical basis. The expansion in circular coordinates is given by:

$$\left(\frac{\partial^2}{\partial r^2}+\frac{1}{r}\frac{\partial}{\partial r}+\frac{1}{r^2}\frac{\partial}{\partial \phi^2}+(k^2-\beta^2)\right)\begin{Bmatrix}E_z\\H_z\end{Bmatrix}=0, \tag{5.1}$$

where k is the wavevector and β is the propagation constant along the cylinder axis. The solutions for the components of the electric and magnetic fields are given by the Bessel functions [147]. For each mode of frequency ω, we can then associate an effective refractive index of the guided mode $n_{eff}=\frac{\beta c}{\omega}$, where c is the speed of light in vacuum. By applying appropriate boundary conditions, one can determine the set of discrete

modes propagating in the waveguide.
We introduce the 3D confinement by "cutting" the waveguide and adding perfect metallic mirrors at both ends separated by the distance L. The interferences between counter-propagating waves, with the same phase and spatial profile, reflected on the mirrors produce a confined mode in between the two mirrors. The resonance condition is the one of a Fabry-Perot cavity, that can be expressed as

$$\omega_c = \frac{p\pi c}{n_{eff}L}, \tag{5.2}$$

where p is an integer number characterizing the longitudinal order of the confined mode. For Fabry-Perot micropillars where the metallic mirrors are replaced by distributed Bragg reflectors, the above description is still valid because the transverse spatial profiles are the same in GaAs and in AlAs waveguides. In the lateral direction, the confinement is thus similar to what was previously discussed. In the vertical direction, the confinement is controlled by the Fabry-Perot cavity as discussed in Chapter 1. The optical modes decay along the z direction. The energy of the confined mode depends on the radius of the micropillar, increasing when the radius decreases [50, 147].

Note that the micropillars discussed in this chapter simultaneously confine light and sound with acoustic frequencies ∼18 GHz. The colocalization of the acoustic and optical fields in the vertical direction is discussed in Chapter 1. The confinement of the optical field in the lateral direction is due to the difference between the optical indices of the micropillar and vacuum. Similarly, the radial confinement of the acoustic fields is due to the difference in acoustic impedances between both media [50, 148].

5.1.2 Optical response

We are interested in the optical response of a pillar microcavity. In particular we are interested in the reflected field. The total reflected field can be interpreted as an interference between the input light reflected on top of the micropillar and the light that entered the cavity and is emerging from the top mirror. It is described by the reflection coefficient [149]:

$$r = 1 - 2\eta_{top}\frac{1}{1 - 2i\frac{\omega-\omega_c}{\kappa}} \tag{5.3}$$

where ω is the energy of the incident beam, ω_c is the energy of the cavity mode, κ is the cavity damping rate including the sidewall losses κ_s and leakage from the top and bottom DBRs $\kappa_{t/b}$ ($\kappa = \kappa_s + \kappa_t + \kappa_b$) [150]. The output coupling through the top DBR is defined by $\eta_{top} = \kappa_{top}/\kappa$. We assume a perfect input coupling, i.e., all the light is injected inside the cavity. Since the reflectivity is a complex number, both the phase and amplitude of the reflected beam are modified by the reflection from the micropillar. Experimentally, we only measure the amplitude of the reflectivity coefficient:

$$R = |r|^2 = \left|1 - 2\eta_{top}\frac{1}{1 - 2i\frac{\omega-\omega_c}{\kappa}}\right|^2. \tag{5.4}$$

The minimum of reflectivity is reached when the wavelength of the input light is equal to the cavity resonant wavelength ($\omega = \omega_c$). The minimum is then given by: $R_{min} = |1 - 2\eta_{top}|^2$.
We experimentally measured the reflectivity of a micropillar with circular cross-section using a home-built reflectometer. The spectrum is obtained by scanning a continuous wave laser (M2 SolsTiS) over a wavelength range covering the cavity mode. Panel **a** of Fig.5.2 shows the measured reflectivity on a Fabry-Perot micropillar with a circular cross-section of diameter of 2.4 µm. The measured reflectivity (dots) is fitted with the equation 5.4 (solid line). The minimum of reflectivity is obtained at $\lambda = 899.94$ nm.

The micropillars used for the experiments are etched out of a planar optophononic cavity by optical lithography and inductively coupled plasma etching. A SEM image of a micropillar with a circular cross-section is displayed in panel **c** of Fig.5.2. The sample under study is grown on a (001)-oriented GaAs substrate by molecular-beam epitaxy. It consists of an optophononic cavity made of two DBRs enclosing a resonant spacer with an optical path length of $\lambda/2$ at a resonance wavelength of around $\lambda \sim 900$ nm. The top (bottom) optical DBR is formed by 25 (29) periods of $Ga_{0.9}Al_{0.1}As/Ga_{0.05}Al_{0.95}As$ $(\lambda/4, \lambda/4)$ bilayers, see panel **b** of Fig.5.2. They act as an optical resonator for near-infrared photons and as an acoustic resonator for longitudinal acoustic phonons around 18 GHz, as described in section 1.4. The micropillars confine an optical mode with typical Q-factors ∼11 000. The samples were fabricated in the clean room facilities of C2N, involving the group of Aristide Lemaître for the growth and the group of Isabelle Sagnes for the etching.

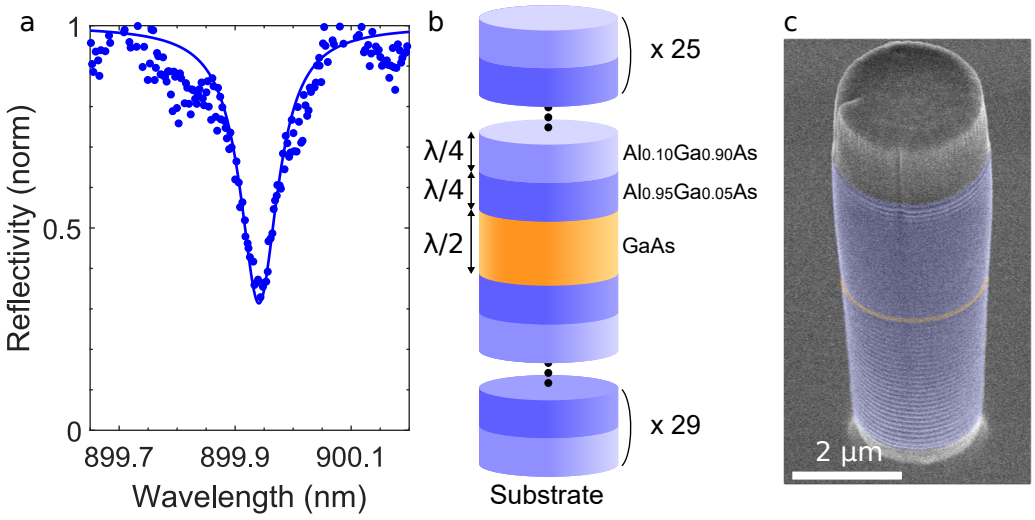

Figure 5.2: **a** Measured (dot) and fitted (solid line) optical reflectivity of a micropillar with circular cross-section of diameter of 2.4 µm. **b** Schematic of the vertical layer structure of the micropillar with two DBRs enclosing a resonant spacer. **c** SEM image of a micropillar with a circular cross-section.

5.2 3D optical confinement in micropillars with elliptical cross-sections

We introduce micropillars with elliptical cross-sections to mimic birefringent materials that scatter light with an energy-dependent change of polarization. Thus, we can control the polarization of the reflected beam.

5.2.1 Guided optical modes in micropillars with elliptical cross-sections

To describe the confined modes in GaAs micropillars with an elliptical cross-section, we first solve the vector Helmholtz wave equation obtained from Maxwell's equations for a waveguide in elliptic coordinates. The development is fully explained in references [151] and [152]. The coordinates are described by ξ and ϕ as depicted in Fig.5.3. We can introduce the elliptic coordinates:

$$\begin{aligned} x &= \rho \cosh(\xi) \cos(\phi), \\ y &= \rho \sinh(\xi) \sin(\phi), \end{aligned} \tag{5.5}$$

where ρ depends on the eccentricity of the ellipse e_c as $\rho = e_c a = \sqrt{a^2 - b^2}$, with $a = \rho\cosh(\xi)$ and $b = \rho\sinh(\xi)$. a and b describe the semimajor and semiminor axes of the ellipse.

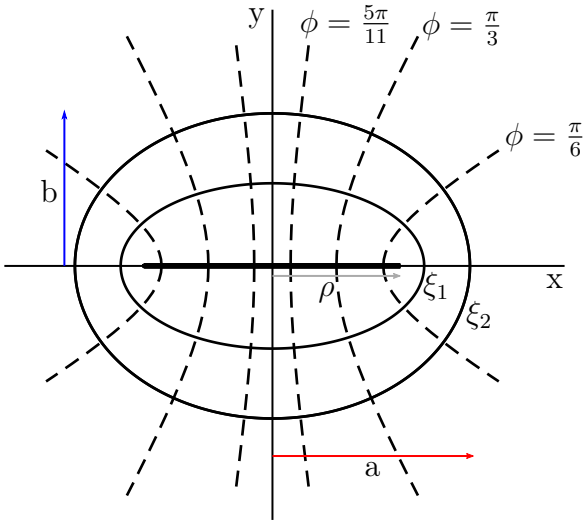

Figure 5.3: Elliptic coordinates.

In the case of a field propagating with a wavevector k along the z direction, the expansion of the wave equation in elliptic coordinates is given by

$$\left(\frac{1}{\rho'(\xi,\phi)}\left(\frac{\partial^2}{\partial\xi^2} + \frac{\partial^2}{\partial\phi^2}\right) + (k^2 - \beta^2)\right)\begin{Bmatrix} E_z \\ H_z \end{Bmatrix} = 0, \tag{5.6}$$

where β is the propagation constant along the cylinder axis. The differential area element in elliptic coordinates is defined by $\rho'(\xi,\phi) = \frac{\rho^2}{2}(\cosh(2\xi) - \cos(2\phi))$. The solutions for

both E_z and H_z can be expressed with the Mathieu functions, which consist of angular and radial parts. Inside the waveguide, the solutions of the angular part are expressed as a function of the angular Mathieu cosine and sine functions, noted $ce_m(\phi;q)$ and $se_m(\phi;q)$, respectively. They are elliptic analogs of the sine and cosine functions that are the angular solutions in systems with circular symmetry. The radial solutions are given by the modified/radial Mathieu even and odd functions, $Ce_m(\xi;q)$ and $Se_m(\xi;q)$ respectively. When the cross-section tends to be circular, the Mathieu functions can be expanded into a series of Bessel functions. The fields inside the waveguide are:

$$\begin{aligned} E_z(\xi,\phi) &= \sum_{m=0}^{\infty} a_m Se_m(\xi;q) se_m(\phi;q), \\ H_z(\xi,\phi) &= \sum_{m=0}^{\infty} b_m Ce_m(\xi;q) ce_m(\phi;q), \end{aligned} \tag{5.7}$$

where a_m/b_m are coefficients to be determined. The solutions depend on $q = (k^2 - \beta^2)\rho^2/4$, which depends on the eccentricity of the waveguide. When the eccentricity increases, that is, when the ellipse flattens, the splitting between the even and odd modes increases. In the case of elliptical micropillars, this leads to the presence of two fundamental optical modes for which the splitting depends on the eccentricity.
The description of guided modes in a waveguide with an elliptical cross-section is defined as a function of the eccentricity of the ellipse. In the case of micropillars, the cross-section is usually described in terms of ellipticity.

5.2.2 Polarization response of an elliptical micropillar cavity

The eccentricity of a micropillar cavity induces a splitting of the fundamental optical cavity mode into two optical modes with orthogonal linear polarizations $|H\rangle$ and $|V\rangle$ aligned with the minor/major axis of the ellipse, as shown in Fig.5.4, whose energies are $\omega_{c,H}$ and $\omega_{c,V}$, respectively.
We define the ellipticity of a micropillar as $e = \sqrt{\frac{m}{n}} - 1$ (not to be confused with the eccentricity) [145], where m and n are the major and minor axis lengths of the elliptical cross-section. Figure 5.4 shows an SEM image of a micropillar with an elliptical cross-section where the two axes are indicated. The reflectivity coefficient depends on the considered axis, yielding:

$$r_H = 1 - 2\eta_{top,H} \frac{1}{1 - 2i\frac{\omega - \omega_{c,H}}{\kappa_H}} \tag{5.8}$$

$$r_V = 1 - 2\eta_{top,V} \frac{1}{1 - 2i\frac{\omega - \omega_{c,V}}{\kappa_V}} \tag{5.9}$$

If one considers an incoming laser beam with polarization amplitudes $b_{in,H}$ and $b_{in,V}$ along $|H\rangle$ and $|V\rangle$, respectively, the input polarization state is defined as:

$$|\psi_{in}\rangle = \frac{1}{\sqrt{|b_{in,H}|^2 + |b_{in,V}|^2}} (b_{in,H}|H\rangle + b_{in,V}|V\rangle \tag{5.10}$$

The associated intracavity field as:

$$|\psi_{cav}\rangle = \frac{1}{\sqrt{|a_H|^2 + |a_V|^2}}(a_H|H\rangle + a_V|V\rangle \tag{5.11}$$

And the reflected field as:

$$|\psi_{refl}\rangle = \frac{1}{\sqrt{|b_{refl,H}|^2 + |b_{refl,V}|^2}}(b_{refl,H}|H\rangle + b_{refl,V}|V\rangle \tag{5.12}$$

In equations 5.10 to 5.12, $b_{in,H/V}$, $a_{H/V}$ and $b_{refl,H/V}$ are the polarization dependent amplitudes of the incoming, intracavity and reflected laser fields, respectively. In equation 5.11, the intracavity field $a_{H/V} \propto b_{in,H/V}\frac{1}{1-2i\frac{\omega-\omega_{c,H/V}}{\kappa_{H/V}}}$ where ω is the input energy, $\omega_{c,H/V}$ are the polarization-dependent cavity resonant energies and $\kappa_{H/V}$ are the polarization-dependent overall cavity damping rates [150, 153]. The reflected fields in equations 5.12 are obtained using the standard input-output equations $b_{refl,H/V} = b_{in,H/V} + \sqrt{\kappa_{t,H/V}} \times a_{H/V}$ [153, 154]. $b_{refl,H/V}$ represents the reflected field as an interference between the input light directly reflected by the top DBR and the light emerging from the cavity in the $|H\rangle/|V\rangle$ polarization states, respectively.

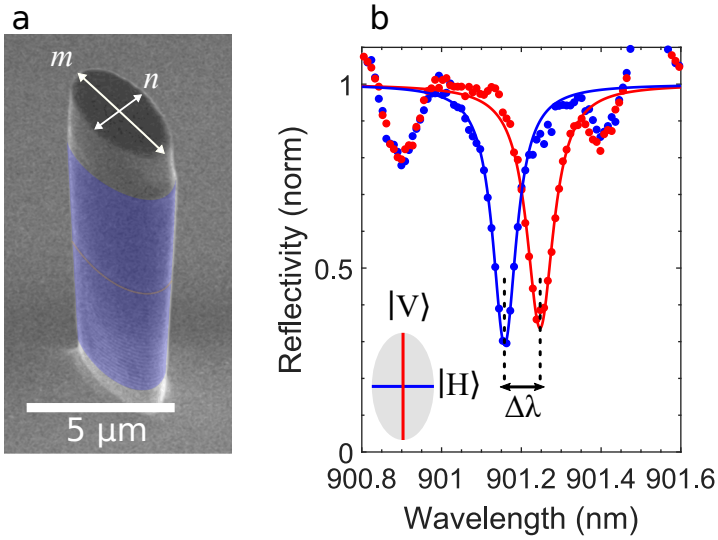

Figure 5.4: **a** SEM image of an elliptical micropillar. m and n are the major and minor axis of the structure, respectively. **b** Measured (dots) and fitted (solid line) optical reflectivity of an elliptical pillar with ellipticity $e = 0.29$, with $m = 4$ µm. Inset, the two fundamental optical eigenmodes are of orthogonal linear polarizations $|V\rangle$ and $|H\rangle$, polarized along the two axes of the cross-section. The blue (red) line corresponds to $|H\rangle$ ($|V\rangle$).

We experimentally measured the polarization-resolved reflectivity of a micropillar with an elliptical cross-section using a home-built reflectometer. The micropillar is made of two DBRs enclosing a resonant spacer with an optical path length of $\lambda/2$ at a resonance wavelength of around $\lambda \sim 900$ nm. The top (bottom) optical DBR is formed by 25 (29) periods of $Ga_{0.9}Al_{0.1}As/Ga_{0.05}Al_{0.95}As$ $(\lambda/4, \lambda/4)$ bilayers. The spectra are obtained by illuminating the micropillar with a broadband light source. The polarization

of the incident beam is controlled by a quarter and a half waveplates. Panel **b** of Fig.5.4 displays the measured reflectivity spectra (dots) of a micropillar with an elliptical cross-section with $e = 0.29$ and $m = 4$ µm. The blue and red spectra are acquired with the incident beam H- and V-polarized along the minor and major axes of the micropillar, respectively. The minima of reflectivity are obtained at $\lambda_H = 901.158$ nm and $\lambda_V = 901.247$ nm and have optical quality factors ∼12000 and ∼11000, respectively. The two optical modes have a wavelength shift $\Delta\lambda = 0.89$ nm. The spectra are fitted with equations 5.8 and 5.9 (solid line).

5.2.3 Polarization state of the reflected beam

Representation of the polarization on the Poincaré sphere

An electromagnetic plane wave can be described by the projection of its electric field on the horizontal/vertical (H/V) basis. The resultant complex numbers E_H and E_V indicate the amplitude and phase of the electromagnetic wave. The choice of the basis is arbitrary, and it is possible to choose a diagonal/anti-diagonal or left/right basis. Here, we choose it to be aligned with the minor and major axes of the elliptical pillar. The polarization state of the electric field can be represented on the Poincaré sphere [155]. We use it to represent the polarization state of the reflected beam and the Brillouin scattering signal. It allows us to represent any coherent or incoherent superposition of polarization states. Pure polarization states are vectors pointing from the center to the surface of the sphere. For incoherent superposition of polarizations, the vector does not reach the surface of the sphere [156]. Linearly polarized states correspond to the "equator" of the sphere, while circular left and right polarization states correspond to the "South" and "North" poles of the sphere. Orthogonal states of polarization, as $|H\rangle$ and $|V\rangle$ or $|D\rangle$ and $|A\rangle$, are opposite vectors.

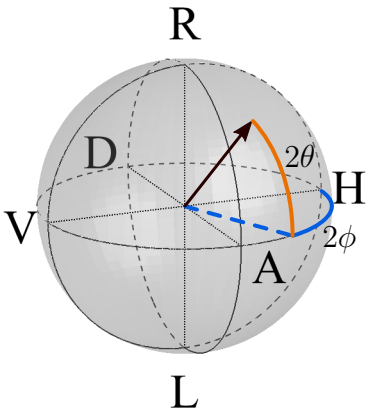

Figure 5.5: Pure polarization state represented on a Poincaré sphere. θ is the ellipticity angle and ϕ is the orientation angle. V, H, D, A, L, R represent the vertical, horizontal, diagonal, anti-diagonal, left and right polarization states, respectively.

We define the Stokes parameters to describe the polarization state of the optical field. They are the projection of the electromagnetic field on the HV, DA and LR axes

on the Poincaré sphere. In the H/V basis, the Stokes parameters are [157, 158]:

$$\begin{aligned} S_{HV} &= \frac{|E_H|^2 - |E_V|^2}{I} \\ S_{DA} &= \frac{2Re(E_H E_V^*)}{I} \\ S_{RL} &= \frac{-2Im(E_H E_V^*)}{I} \end{aligned} \tag{5.13}$$

The normalization parameter I is the total intensity, $I = |E_H|^2 + |E_V|^2$. The polarization state is characterized by two angles θ and ϕ, represented on the Poincaré sphere. The ellipticity of the polarization state is defined by θ. For $\theta = 0°$ we obtain a linear state, while for $\theta = 45°$ we obtain a circular state. ϕ defines the orientation of the polarization state, where $\phi = 0°, 45°$ and $90°$ correspond to $|H\rangle$, $|D\rangle$ and $|V\rangle$, respectively.

Simulations using the Jones Matrices formalism

The polarization state of the reflected beam is simulated using the Jones matrices formalism [157]. The calculation of the polarization state is based on the experimental scheme. The input polarization state is initialized with a vertical linear polarizer. Then, a quarter and a half waveplates control the polarization state of the incident beam on the micropillar. The polarization state of the incident beam in the H/V basis is given by:

$$|\psi_{in}\rangle = M(-\theta_2)W_{\lambda/2}M(\theta_2) \times M(-\theta_1)W_{\lambda/4}M(\theta_1) \times P_V \times |\psi_0\rangle, \tag{5.14}$$

where $|\psi_0\rangle$ is a random polarization. The Jones matrices of the waveplates ($W_{\lambda/2}$ and $W_{\lambda/4}$), the polarizer (P_V) and the rotation matrix ($M(\theta)$) are given in Appendix B. The polarization of the reflected beam is given by:

$$|\psi_{refl}\rangle = M_{sample} \times |\psi_{in}\rangle \tag{5.15}$$

To simulate the spectrum of light with rotation of polarization, we measure in the orthogonal basis:

$$|\psi_{meas}\rangle = P_H \times M(\theta_1)W_{\lambda/4}M(-\theta_1) \times M(\theta_2)W_{\lambda/2}M(-\theta_2) \times |\psi_{refl}\rangle. \tag{5.16}$$

Polarization rotation of the reflected laser

We consider a diagonal incident field $|\psi_{in}\rangle = \frac{1}{\sqrt{2}}(|H\rangle + |V\rangle) = |D\rangle$ and detect $|\langle\psi_{det}|\psi_{refl}\rangle|^2$. We measure the antidiagonal component of the signal, $|\psi_{det}\rangle = |\overline{\psi_{in}}\rangle = |A\rangle$, collecting the light in a cross-polarized scheme. The collected signal corresponds to light with a polarization component along $|A\rangle$, i.e., that has undergone a rotation of polarization.

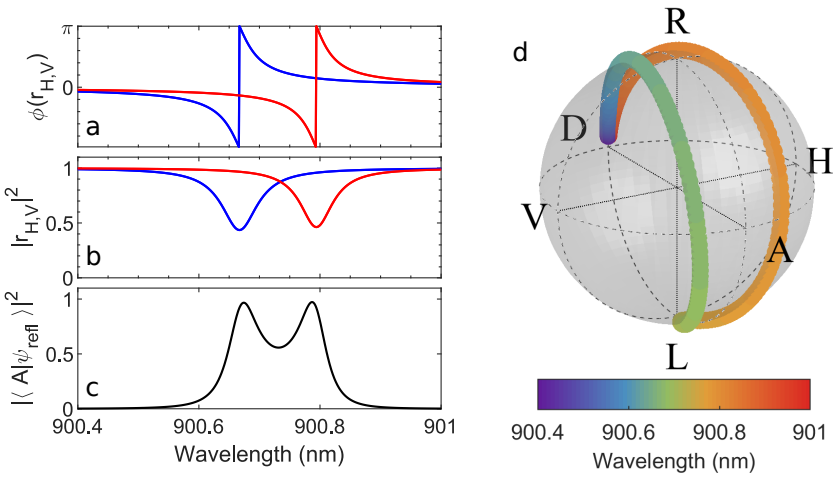

Figure 5.6: **a, b** Calculated phase and amplitude, respectively, of the H (blue) and V (red) optical modes. **c** Intensity of the reflected field projected along $|A\rangle$ as a function of wavelength. **d** Poincaré sphere displaying the calculated wavelength-dependent polarization state $|\psi_{refl}\rangle$ of the reflected laser.

The calculated amplitudes and phases of the reflection coefficients for the H- and V-polarized optical cavities of a micropillar with $e = 0.41$ are plotted in panels **a** and **b** of Fig.5.6. When the wavelength is swept across the cavity modes, there is a phase shift of the H mode centered on its resonant wavelength, followed by a phase shift of the V mode. For a laser tuned in the optical modes, the components of the fields projected on $|H\rangle$ and $|V\rangle$ will get reflected with different reflectivity coefficients r_H and r_V inducing a rotation of polarization of the reflected state. When the wavelength of the incoming laser is far-detuned from the cavity modes, the beam cannot enter the cavity and therefore, there is no cavity-induced polarization rotation, resulting in the rotated signal being nearly zero. Panel **d** of Fig.5.6 shows the polarization state of the reflected field as a function of wavelength on a Poincaré sphere. We observe a wavelength-dependent rotation of polarization of the reflected field with a trajectory covering the full sphere, starting from $|D\rangle$ when the laser is outside the cavity modes. The spectrum on panel **c** of Fig.5.6 displays the intensity of the reflected field projected along $|A\rangle$ as a function of wavelength $|\langle A|\psi_{refl}\rangle|^2$, which corresponds to the rotation of polarization of the reflected field. The two amplitude maxima correspond to wavelengths for which the polarization of the reflected laser is the closest to anti-diagonal.

5.2.4 Incidence of the micropillar ellipticity on the optical properties

Optical mode splitting

As mentioned in Sect.5.2.1, the cross-section ellipticity of the micropillars controls the splitting between the H and V-polarized optical modes. By changing the ratio between the two axes, m and n, of the micropillar we can engineer the splitting between both optical modes. Figure 5.7 shows the measured mode splitting of the micropillar with different ellipticities ($e = \sqrt{m/n} - 1$), with the major axis length kept constant. The splitting between the two optical modes is proportional to the micropillar ellipticity.

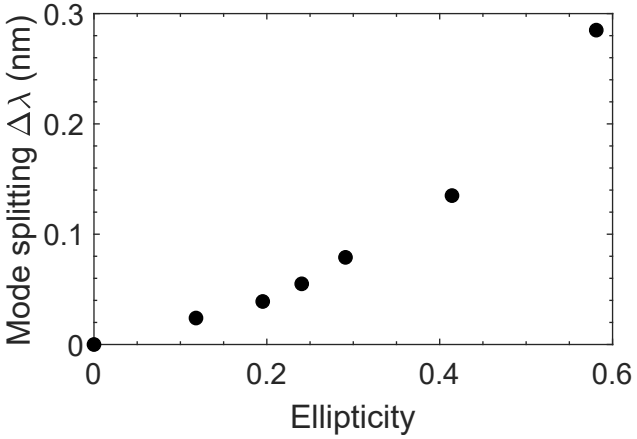

Figure 5.7: Measured evolution of the optical mode splitting as a function of the ellipticity. The major axis length is kept constant $m = 4$ µm, and only the minor axis length is varying from 1.6 µm to 4 µm.

Polarization state of the reflected beam

We theoretically demonstrate that by changing the mode splitting, the rotation of polarization encountered by the reflected beam for diagonal incident polarization ($|\psi_{in}\rangle = |D\rangle$) is modified. Figure 5.8 displays the calculated reflectivity amplitudes (middle panel) and phases (top panel) for optical modes with a splitting going from 0.005 nm (panel **a**) to 0.60 nm (panel **f**). The bottom panel shows the spectra of the reflected laser projected on the anti-diagonal axis $|\langle A|\psi_{refl}\rangle|^2$, i.e., the reflected laser with rotation of polarization . For cases **a** to **c**, the spectra with rotation of polarization show single peaks, corresponding to the maximum rotation of polarization toward $|A\rangle$, equally detuned from the H and V optical cavity modes. The maximum intensity centered between the two optical modes can be explained by the fact that we obtain both equal amplitudes for r_H and r_V, and opposite phases. In the particular case of panel **c** of Fig.5.8, the polarization is maximally rotated to the anti-diagonal state. When the mode splitting is smaller (panels **a** and **b**), the polarization of the reflected beam does not reach anti-diagonal when it is equally detuned from both modes, hence the lower amplitude.
For the cases with higher ellipticity (panels **d** to **f**), $\Delta\phi = |\phi(r_H) - \phi(r_V)|$ decreases for a wavelength equally detuned from the H and V-polarized cavity modes. Therefore, between the two optical modes the polarization state of the reflected laser tends to turn back to diagonal. As a result, the spectra of the reflected field with rotation of polarization present two peaks centered on the resonant wavelength and with linewidths similar to those of the optical cavity modes. The Poincaré sphere in panel **g** displays the polarization state of the reflected beam for a wavelength centered between the two optical modes as a function of the mode splitting. We can clearly see that, when the mode splitting increases, the polarization state of the central wavelength goes around the Poincaré sphere following the $DRAL$ meridian and crossing $|A\rangle$ when $\Delta\lambda \approx 0.055$ nm.

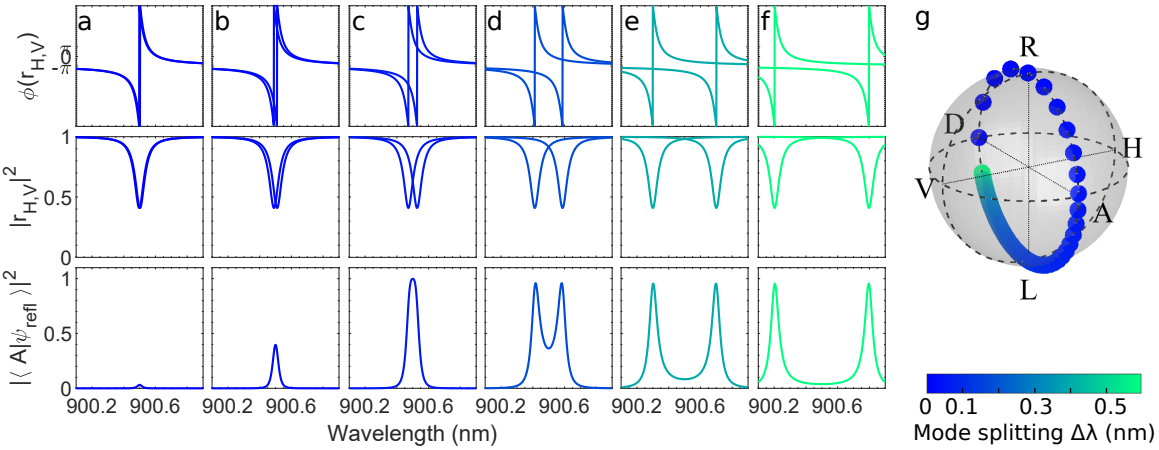

Figure 5.8: Top panel: Simulated reflectivity phase of the H and V optical modes as a function of the mode splitting $\Delta\lambda$. Middle panel: Simulated reflectivity amplitude of the H and V optical modes as a function of the mode splitting. Bottom panel: Calculated spectra of the reflected laser with rotation of polarization. The incident laser is polarized along $|D\rangle$, while the detection is along $|A\rangle$. The mode splitting increases from **a** to **f**. **g** Polarization state of the reflected beam plotted on a Poincaré sphere when equally detuned from both optical modes.

We experimentally measured the influence of ellipticity on the polarization state of the reflected beam. We studied a sample consisting of arrays of GaAs/AlAs micropillars with different elliptical cross-sections (see panel **a** of Fig.5.9). The micropillars are made from Fabry-Perot cavities with two DBRs enclosing a resonant spacer with an optical path length of $\lambda/2$. The structure is described in section 5.1.2.

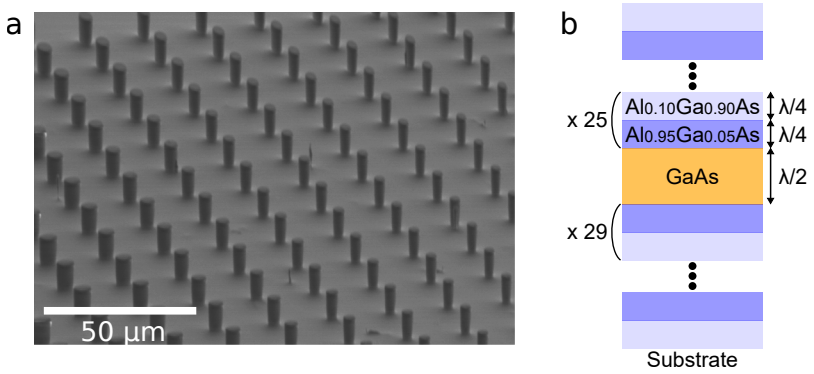

Figure 5.9: **a** SEM image of an array of micropillars with various sizes and ellipticities. **b** Schematic of the vertical layer structure of the micropillar with two DBRs enclosing a resonant spacer.

We measured the projection of the reflected field $|\psi_{refl}\rangle$ on the anti-diagonal polarization axis $|\langle A|\psi_{refl}\rangle|^2$ for three micropillars presenting ellipticities $e = 0.29$, $e = 0.41$ and $e = 0.58$ with $m = 4$ µm kept constant, i.e. corresponding to the minor axis length $n = 2.4$ µm, $n = 2$ µm and $n = 1.6$ µm, as shown in panels **a**, **b** and **c** of Fig.5.10, respectively. We observe two peaks in the spectra of the reflected beam with rotation of polarization when the ellipticity increases. Moreover, even though m is constant, we observe a blue-shift of the V-polarized mode when the ellipticity increases. This is due

to the decrease in the mean radius of the pillar [152].
The bottom panel of Fig.5.10 displays the calculated polarization state of the reflected beam $|\psi_{refl}\rangle$ as a function of wavelength. Similarly to Fig.5.8, the polarization state of the reflected field goes around the Poincaré sphere when the mode splitting increases. Thus, by engineering the ellipticity of the micropillar we can control the polarization state of the reflected laser.

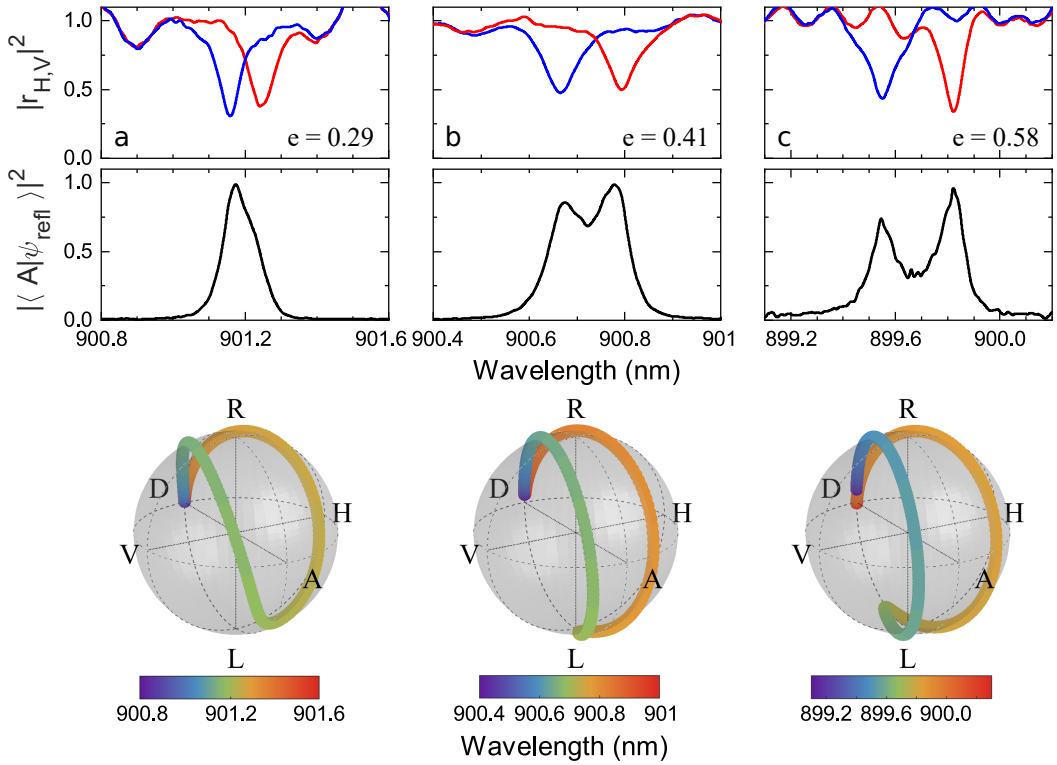

Figure 5.10: Top panel: Experimental reflectivity spectra of an elliptical micropillar of ellipticity (**a**) e =0.29, (**b**) e =0.4 and (**c**) e =0.58, with m = 4 µm. The blue (red) spectrum is measured with a linear polarization aligned with the minor (major) axis of the elliptical pillar cross-section. Two clear optical modes are observed at different central wavelengths. Middle panel: Spectrum of the reflected laser with rotation of polarization for the three ellipticity respectively. The incident laser is polarized along $|D\rangle$, while the detection is along $|A\rangle$. Bottom panel: Poincaré sphere displaying the calculated wavelength-dependent polarization state $|\psi_{refl}\rangle$ of the reflected laser.

5.3 Controlling the Brillouin scattering polarization with elliptical micropillars

Performing a similar analysis to the one presented for the reflected beam, the polarization state of the Raman scattering field can be expressed as:

$$|\psi_B\rangle = \frac{1}{\sqrt{|b_{B,H}|^2 + |b_{B,V}|^2}}(b_{B,H}|H\rangle + b_{B,V}|V\rangle, \tag{5.17}$$

where $b_{B,H/V}$ is the reflectivity coefficient for Brillouin scattering. The Brillouin scattering field, which is generated inside the GaAs spacer, has the same polarization state as

the intracavity field $|\psi_{cav}\rangle$ but at a different frequency ω_B. Therefore, the polarization of Brillouin scattering depends on both intracavity field polarization generated by the incident beam and on the Brillouin frequency:

$$b_{B,H/V} \propto a_{H/V} \times \frac{1}{1-2i\frac{\omega_B-\omega_{c,H/V}}{\kappa_{H/V}}}, \tag{5.18}$$

where $a_{H,V} \propto b_{in,H/V}\frac{1}{1-2i\frac{\omega_{in}-\omega_{c,H/V}}{\kappa_{H/V}}}$ is defined in section 5.2.2. The first term of $b_{B,H/V}$ depends on the input polarization state and energy through the intracavity amplitude $a_{H/V}$. The second term depends on the detuning between the energy of the Brillouin scattering mode with the optical modes. Similarly to the reflectivity of the micropillar, we can assign a Jones matrix to the Brillouin scattering. The polarization states of Brillouin scattering are simulated considering Brillouin scattering as a source inside the cavity spacer:

$$|\psi_B\rangle = \begin{bmatrix} b_{B,H} & 0 \\ 0 & b_{B,V} \end{bmatrix} \times |\psi_{in}\rangle \tag{5.19}$$

Similarly to the polarization state of the reflected laser, depending on the ellipticity of the micropillar and the laser wavelength, the polarization state of the Brillouin signal scattered from the micropillar depends on these same parameters. Moreover, due to the frequency shift of the Brillouin scattering from the laser line, both signals experience different degrees of polarization rotation, resulting in $|\psi_{in}\rangle \neq |\psi_{refl}\rangle \neq |\psi_B\rangle$. In addition, the Brillouin scattering signals of the different acoustic modes also have different polarization states. Therefore, the polarization state of the Brillouin signal in a micropillar with an elliptical cross-section is no longer determined only by the intrinsic selection rules of the material as defined in section 2.1.3 ($|\psi_{in}\rangle = |\psi_{refl}\rangle = |\psi_B\rangle$ for GaAs), but can be controlled by the micropillar geometry. The different polarization states of the reflected laser and Brillouin scattered from the micropillar allow for the discrimination of the Brillouin signal from the reflected laser by polarization filtering.

5.4 Brillouin scattering experimental results on elliptical micropillars

5.4.1 Experimental scheme

In this section we measure Brillouin spectra on 3D micropillar cavities. The 3D confinement breaks up the optical dispersion relation of the cavity into discretized modes, restricting the use of the Brillouin scattering spectroscopy technique based on angular filtering that we presented in Chapter 4. In addition, the stray-light due to the wavelength-scale object is more intense than in a planar cavity. The Brillouin spectroscopy setup is in backscattering configuration, with both the incident and reflected beams at normal incidence on the sample. As a result, the reflected beam and the Brillouin signal spatially overlap. We implement an alternative filtering of the Brillouin signal based on polarization.

The sample is placed in a vacuum chamber at room temperature to avoid oxidation of the Al on the sides of the micropillar. A schematic of the cross-polarized experimental setup is presented in Fig.5.11. A collimated laser beam from a tunable continuous wave (CW) Ti:Sapphire laser (M2 SolsTis) is used as the excitation source. The incident beam polarization is initialized with a polarizer. A second polarizer is placed in the collection path in a cross-polarized scheme. A quarter-waveplate and a half-waveplate ($\lambda/4$ and $\lambda/2$) control the incident polarization state on the sample $|\psi_{in}\rangle$. The incident laser beam is focused onto the sample with a spot diameter of approximately 2.2 µm using a NA = 0.7 objective lens placed inside the vacuum chamber of the cryostat. We collect the reflected signal through the same objective and waveplates. A second set of waveplates, placed in front of the polarizer in the collection path, allows us to choose the polarization basis for the collection, while the second polarizer acts as an analyzer.

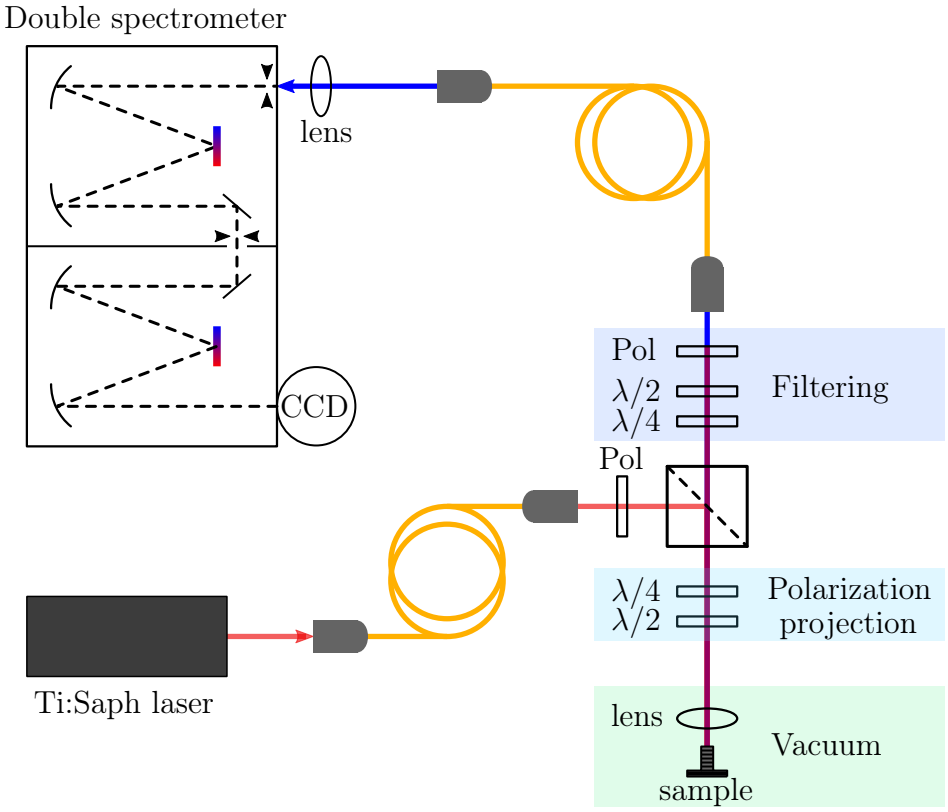

Figure 5.11: Cross-polarized experimental setup. A laser generates a continuous wave laser beam. The beam is coupled into a single mode fiber. The collimated beam at the output of the fiber passes through a polarizer (Pol) to initialize the polarization being sent onto the onto the sample by a beam splitter. Then, the beam passes through a quarter and a half waveplates ($\lambda/4$, $\lambda/2$) to project the polarization to the H/V basis. The beam is focused on the sample with an objective lens inside the vacuum chamber. The reflected beam and the Brillouin signal pass through the same objective and waveplates. A second set of waveplates and polarizer after the beam splitter allow us to collect in any polarization basis. The beam is coupled into a fiber and sent into a double chamber spectrometer. The dashed line represents the path of the beam inside the spectrometer.

To observe the rotation of polarization of the reflected beam, the incident beam polarization is set to $|D\rangle$ and collection is set to $|A\rangle$. The Brillouin signal emerging

from the sample is collected through the same objective and waveplates.
The second set of waveplates in front of the polarizer in the collection path allows us to extinguish the laser before the remainder of the light is coupled into a single mode fiber when performing Brillouin scattering measurements. The transmission of the polarizer in the collection path is 86% at the wavelength of interest 900 nm. The extinction ratio of the reflected excitation laser measured on a micropillar of $e = 0.41$ is 45:1 when Stokes and anti-Stokes are coupled to the V and H optical modes and 78:1 when only Stokes is coupled to a cavity mode, measured before the collection fiber. The use of a single mode fiber increases the purity of the signal through spatial filtering [154]. The Brillouin signal is finally analyzed with a double spectrometer operating in additive mode. The Brillouin spectra presented below are typically obtained with an incident laser power of 50 µW, with integration times in the range of 0.1 s to 5 s.

5.4.2 Polarization rotation-enabled optical filtering

To discriminate the Brillouin signal from the reflected laser, we exploit the difference in rotation of polarization between the reflected laser beam and Brillouin scattering which implies $|\psi_{in}\rangle \neq |\psi_{refl}\rangle \neq |\psi_B\rangle$. Detecting the Brillouin scattered signal requires to filter out the laser light. We achieve this filtering by detecting in a cross-polarization geometry ensuring that $\langle\psi_{det}|\psi_{refl}\rangle = 0$. That is:

$$|\psi_{det}\rangle = |\overline{\psi_{refl}}\rangle = \frac{1}{\sqrt{|b_{refl,H}|^2 + |b_{refl,V}|^2}}(b^*_{refl,V}|H\rangle + b^*_{refl,H}|V\rangle). \tag{5.20}$$

Due to the wavelength-dependence of $|\psi_{refl}\rangle$, the cross-polarized scheme ensuring that $\langle\psi_{det}|\psi_{refl}\rangle = 0$ is wavelength-dependent as shown in panels **b** to **d** of Fig.5.12. Indeed, the conditions to obtain cross-polarization vary with the wavelength to which the excitation laser is tuned to obtain the Brillouin spectra. Panels **b** to **d** display the reflectivity spectra obtained after filtering the reflected laser in Brillouin experiments for three different laser wavelengths. The spectra correspond to $|\langle\overline{\psi_{refl}}(\omega_{laser})|\psi_{refl}(\omega)\rangle|^2$, where ω_{laser} is the energy of the incident laser used to acquire the Brillouin spectrum. Thedashed vertical line in each spectrum marks the wavelength of the incident laser. One can observe that after filtering, the reflectivity is minimum at the excitation wavelength used to acquire Brillouin spectra. In panel **a**, the reflectivities of the H- and V-polarized optical modes are plotted for reference. The experiment is performed at low laser power to avoid thermal effects [31].

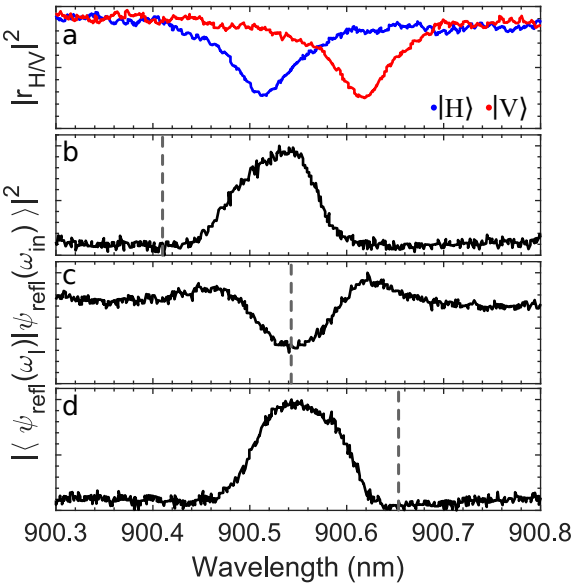

Figure 5.12: **a** Optical modes for a micropillar with $e = 0.41$ and $m = 4$ µm. The blue line is the H-polarized mode and the red line is the V-polarized mode. **b-d** Reflectivity spectra acquired after filtering out the reflected laser in a Brillouin spectroscopy measurement. The dashed vertical lines indicate the wavelength of the excitation laser used for the Brillouin measurements.

Figure 5.13 shows a Brillouin spectrum acquired on a micropillar with an elliptical cross-section $e = 0.41$ with $m = 4$ µm. The laser wavelength is tuned to $\lambda = 900.542$ nm, corresponding to the reflectivity after filtering displayed in panel **c** of Fig.5.12. To acquire this spectrum, an etalon filter was inserted before the spectrometer to increase the resolution. The method for the sequential point-by-point reconstruction of the Brillouin spectrum is presented in Chapter 4. In the spectrum displayed in Fig.5.13, due to the polarization filtering, we are able to observe peaks corresponding to both Stokes and anti-Stokes next to the laser line. The peaks at ±18 GHz correspond to the fundamental confined acoustic mode in anti-Stokes and Stokes scattering. The peaks at ∼40 GHz in Stokes and anti-Stokes Brillouin scattering correspond to the Brillouin mode of GaAs.

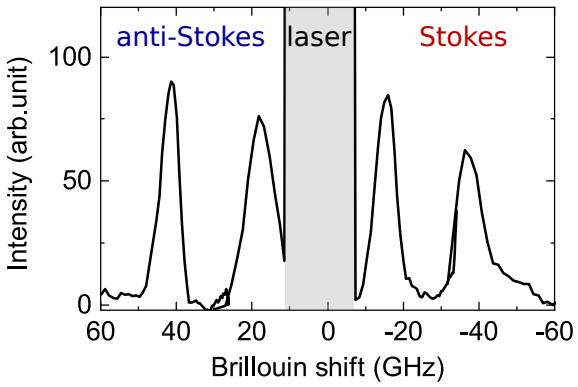

Figure 5.13: Brillouin spectrum acquired on an elliptical micropillar with $e = 0.41$ and $m = 4$ µm. The laser wavelength is $\lambda = 900.542$ nm and the incident power is 50 µW.

5.4.3 Influence of the laser wavelength on the Brillouin spectrum

In this section, we study the influence of the laser wavelength on the Brillouin spectrum. We measured multiple Brillouin spectra by varying the excitation laser wavelength across the cavity modes. The polarization of the incident beam is fixed to diagonal $|D\rangle$ for all the measurements. The polarization filtering of the signal at the collection is adjusted for each measurement to filter out the reflected laser.
The micropillar studied in this section has an ellipticity $e = 0.29$, with $m = 4$ µm. The H and V-polarized optical modes are centered at 900.158 nm and 900.247 nm, respectively (see figure 5.10**a**). The polarization states of the different Brillouin modes, as well as the reflected laser, are simulated and plotted on a Poincaré sphere for the different laser wavelengths. As a reference, the polarization state of the reflected beam as a function of wavelength is plotted on a Poincaré sphere in panel **m** of Fig.5.14, where the stars indicate the polarization state of the reflected laser for each of the measured cases.
In panel **a** of Fig.5.14 we show a simulated Brillouin spectrum of the vertical one-dimensional multilayered structure. We assume a purely photoelastic interaction [97]. For the numerical implementation, we use the transfer matrix method with nominal material properties (see Table 1) and assume a planar GaAs/AlAs Fabry-Perot cavity with a single optical mode. The vertical structure is described in section 5.1.2. The polarization is not taken into account in this model. The spectrum is convoluted with a Gaussian function resulting in a resolution of 0.025 GHz. We observe peaks at ±18 GHz, ±54 GHz and ±90 GHz corresponding to the Stokes and anti-Stokes harmonics of the acoustic modes confined in the cavity [48, 136]. Panels **b** to **h** correspond to experimental Brillouin spectra measured at excitation laser wavelengths going from 900.918 nm to 901.390 nm. The polarization-dependent optical reflectivity is included in each panel with dashed blue and red lines corresponding to $|H\rangle$ and $|V\rangle$ polarization, respectively. Panels **b** to **e** of Fig.5.14 display Brillouin spectra obtained with the laser blue-detuned from the cavity modes, at wavelengths of 900.918 nm, 901.002 nm, 901.088 nm and 901.107 nm, respectively. Those spectra present only Stokes components since the anti-Stokes components lie outside of the cavity modes and are thus not enhanced. Panels **i** to **l** of Fig.5.14 show on the same sphere the simulated polarization states of the reflected laser $|\psi_{refl}\rangle$ (black star) and of the Brillouin scattered signals $|\psi_B\rangle$ corresponding to the measured cases. In Fig.5.14**b**, where the laser is the most blue-detuned, the observed Stokes Brillouin spectrum shows that the fifth harmonic mode, at 90 GHz, is resonant with the H-polarized cavity mode. The Stokes components at high frequencies are enhanced by the presence of the optical cavity modes. We also see weak contributions at -40 GHz corresponding to the Brillouin signal originating in the GaAs substrate, and at -54 GHz. The contribution from GaAs is observable in all the spectra with various intensity depending on its coupling to the optical modes. In panel **c** of Fig.5.14, the laser is slightly red-shifted with respect to the previous case. In that case, the Stokes Brillouin mode at -54 GHz is enhanced by the H-polarized cavity mode. Even though the fifth harmonic polarization state is also different from $|\psi_{refl}(\omega_{laser})\rangle$, we are not able to see it because the laser is too blue-detuned from the V-polarized cavity. In panel **d**

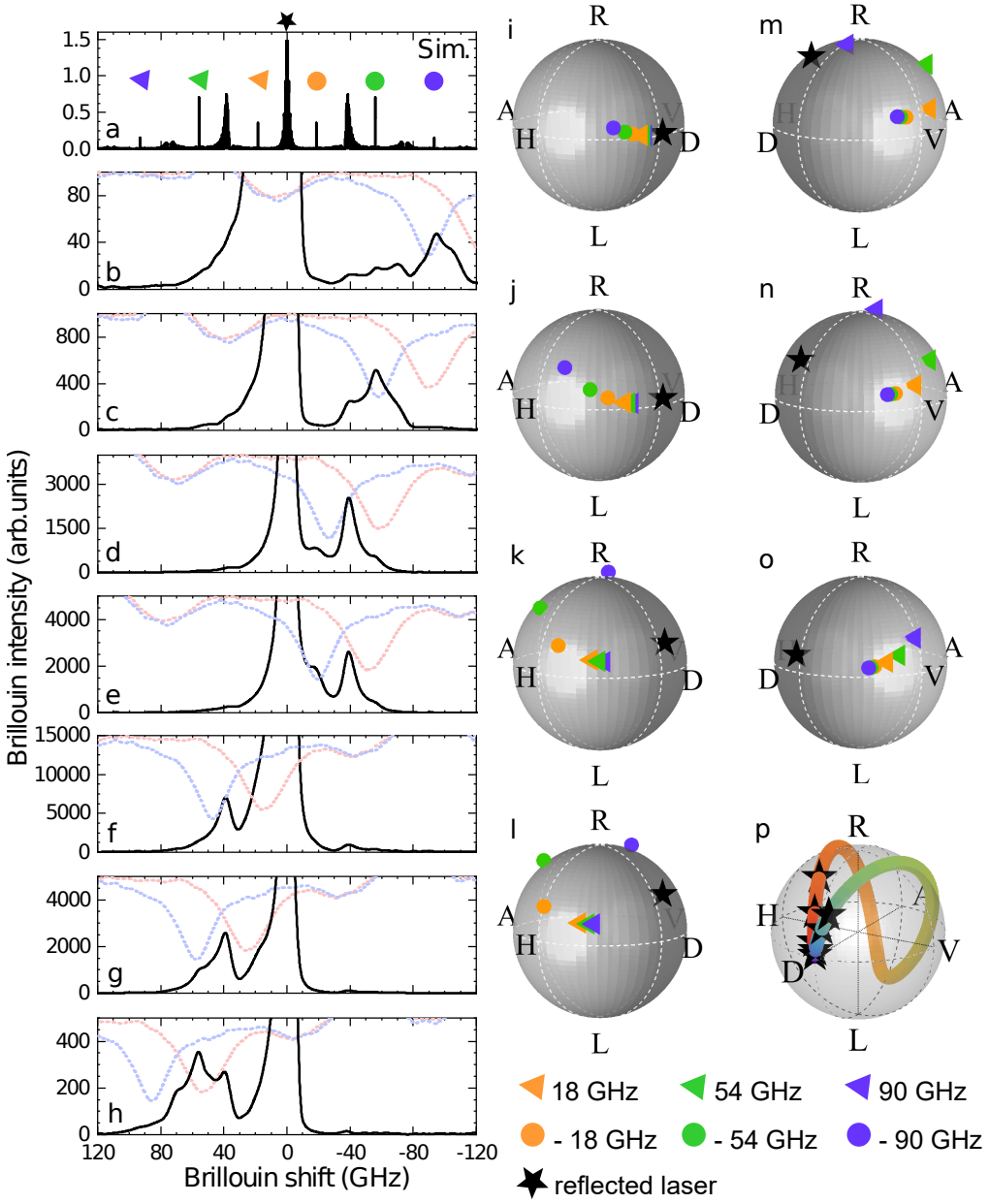

Figure 5.14: **a** Simulated Brillouin spectrum for a planar cavity with the multilayer structure shown in Fig.5.9. Experimental Brillouin spectra acquired on a micropillar with $e = 0.29$, with the excitation laser **b-e** blue-detuned from the optical modes and **f-h** red-detuned from the optical modes. The peak at ± 18 GHz corresponds to the fundamental confined acoustic mode of the resonator. The peak at ± 37 GHz corresponds to bulk Brillouin scattering from the substrate. The peak at ± 54 GHz corresponds to the third harmonic of the confined mode. The peak at ± 90 GHz corresponds to the third harmonic of the confined mode. Simulated polarization of the reflected laser and Brillouin signals plotted on Poincaré spheres, **i-l** when the laser is blue-detuned and **m-o** when the laser is red-detuned, corresponding to panels **b-h**, respectively. **p** Simulated polarization states of the reflected laser as a function of wavelength. The stars indicate the polarization states of the reflected laser for the wavelength used experimentally.

and **e** of Fig.5.14, the fundamental mode at −18 GHz is clearly observable in the Stokes Brillouin spectrum. The Stokes mode at −18 GHz is resonant with the H-polarized cavity mode and the third harmonic, at −54 GHz, is coupled to the V-polarized cavity mode.
In order to selectively measure the anti-Stokes components enhanced by the coupling to the optical cavity modes in a cross-polarized configuration, the laser is red-detuned from the optical cavity modes. Panels **f** to **h** of Fig.5.14 display Brillouin spectra obtained with a laser red-detuned from the cavity modes, at wavelengths of 901.284 nm, 901.314 nm and 901.390 nm, respectively. Panels **m** to **o** of Fig.5.14 show the simulated polarization states of the reflected laser $|\psi_{refl}\rangle$ and of the Brillouin scattered signals $|\psi_B\rangle$. These spectra present only anti-Stokes components since only they are coupled to the cavity modes.
Panels **f** and **g** of Fig.5.14 show spectra obtained with the laser red-detuned at 901.284 nm and 901.390 nm. The observed anti-Stokes Brillouin spectra show the mode at 18 GHz which is coupled to the V-polarized optical cavity, and the mode at 54 GHz coupled to the H-polarized cavity mode. However, the laser line is rather intense which prevents us from observing a clear peak at 18 GHz. The intense laser line can be due to stray-light scattered by the optical elements of the setup or by remains of the reflected laser. Note that the stray-light may not have the same polarization as the reflected laser since it does not necessarily emerge from the micropillar. Nevertheless, the peak at 40 GHz is clearly visible, as well as a weak contribution from Stokes Brillouin scattering at −40 GHz. Panel **h** of Fig.5.14 is the mirrored version of panel **c**. The anti-Stokes Brillouin mode at 54 GHz is enhanced by the V-polarized optical cavity mode. Similarly to Stokes, the anti-Stokes Brillouin signal experiences a rotation of polarization different from the reflected laser enabling its detection.
It is interesting to note that the polarization state of the Brillouin scattering depends on the optical mode to which both the laser and the Brillouin signal are mainly coupled. When the laser is blue-detuned, the different modes have polarization states on the $|H\rangle$ hemisphere, in opposition with a red-detuned laser. A Brillouin mode coupled to the H-polarized mode tends to get scattered with a polarization along $|H\rangle$, while a Brillouin mode coupled to the V-polarized mode tends to get scattered with a polarization along $|V\rangle$. In Fig.5.14, we observe that in the case of Stokes Brillouin scattering, the modes are mainly enhanced by the H-polarized mode (panels **b** to **e** of Fig.5.14), resulting in scattered signals more H-polarized (panels **i** to **l** of Fig.5.14). On the other hand, anti-Stokes Brillouin scattering is mainly V-polarized (panels **m** to **o** of Fig.5.14), due to the coupling to the V-polarized mode (panels **f** to **h** of Fig.5.14).
In this section, we discussed the excitation wavelength as a means to optimize the measurement of Brillouin spectra in an elliptical micropillar. The optimum configuration for cross-polarized filtering would be having the reflected laser and the Brillouin signal with orthogonal polarization states, i.e. in opposite poles of the Poincaré sphere. In the next section, we see how the ellipticity of the micropillar also plays an important role in the acquired Brillouin spectra.

5.4.4 Incidence of the ellipticity on the Brillouin spectrum

In this section, we theoretically and experimentally analyze the effects of changing the ellipticity of the micropillar on the scattering selection rules. In section 5.2.4, we discussed the effect of the ellipticity on the optical mode splitting and polarization state of the reflected beam. When the ellipticity increases, the splitting between the two optical modes increases. As a consequence, we have seen that the rotation of polarization of the reflected beam is strongly modified. Here, we discuss how the ellipticity impacts the Brillouin scattering polarization state.

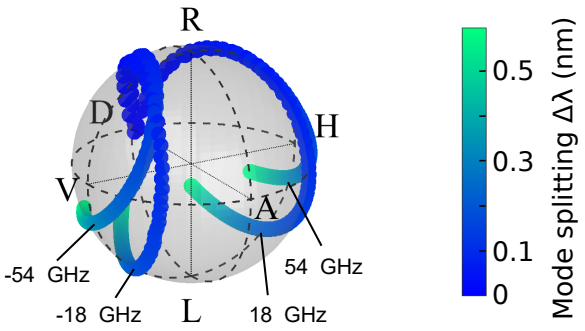

Figure 5.15: Brillouin polarization states for the fundamental and third harmonic of the confined acoustic mode as a function of the mode splitting $\Delta\lambda$ between the two optical modes in elliptical micropillars. We consider the particular case of an excitation laser polarized along $|D\rangle$ and spectrally tuned between the two optical modes. By increasing $\Delta\lambda$, the Brillouin modes describe frequency-dependent trajectories that span the Poincaré sphere.

Figure 5.15 shows the simulated polarization state of the Brillouin signal as a function of the micropillar ellipticity while keeping the excitation wavelength centered between the two optical cavity modes and the input polarization along $|D\rangle$. This set of conditions corresponds to the same excitation conditions used in Fig.5.8. We observe that, contrary to the polarization state of the reflected laser, the Brillouin polarization states are always away from the $DRAL$ meridians. Moreover, the trajectory of the Brillouin signal shows that the relation between the incident laser and signal polarization states is strongly modified, breaking the intrinsic polarization selection rules of GaAs. The accessible phonon frequency band is determined by the separation of the optical cavity modes. For zero separation, the Brillouin polarization states coincide with the excitation laser. The difference in polarization states observed between Brillouin scattering and the reflected laser enables an efficient polarization filtering protocol for non-degenerate polarization-dependent optical modes.
We experimentally studied Brillouin scattering in two micropillars with different ellipticities $e = 0.41$ and $e = 0.58$ and the major axis length fixed (figures 5.16 and 5.17 respectively), whose reflectivity spectra and spectra of the reflected beam with rotation of polarization are shown in panels **b** and **c** of Fig.5.10, respectively.
Figure 5.16 displays Brillouin spectra from a micropillar with $e = 0.41$. The H and V-polarized optical modes are centered at 900.667 nm and 900.795 nm, respectively. The spectra are acquired with the laser tuned at 900.615 nm, 900.737 nm and 900.860 nm (panel **a**,**b** and **c**, respectively). Panels **d** to **f** show on the same sphere the matching

simulated polarization states of the reflected laser $|\psi_{refl}(\omega_{laser})\rangle$ and the Brillouin scattered signals $|\psi_B\rangle$. Contrary to the Brillouin spectra presented in Fig.5.14, we are able to measure Stokes and anti-Stokes Brillouin scattering at the same time, see Fig.5.16**b**. The optical mode splitting $\Delta\lambda = 0.128$ nm is larger in that case than for $e = 0.29$, enabling us to simultaneously enhance Stokes and anti-Stokes when the laser wavelength is centered in between the two optical modes. The polarization states corresponding to this situation are plotted on the Poincaré sphere in panel **e**. We can see that the different Brillouin modes and the reflected laser have polarizations distributed all over the Poincaré sphere. Panel **a** of Fig.5.16 plots a Stokes Brillouin spectrum (with the laser blue-detuned) where the mode at -18 GHz is enhanced by the H-polarized optical mode. This configuration results in a spectrum mostly polarized along $|H\rangle$. On the opposite, panel **c** displays an enhanced anti-Stokes spectrum, with a Poincaré sphere (panel **f**) mirrored from the one in panel **d**.

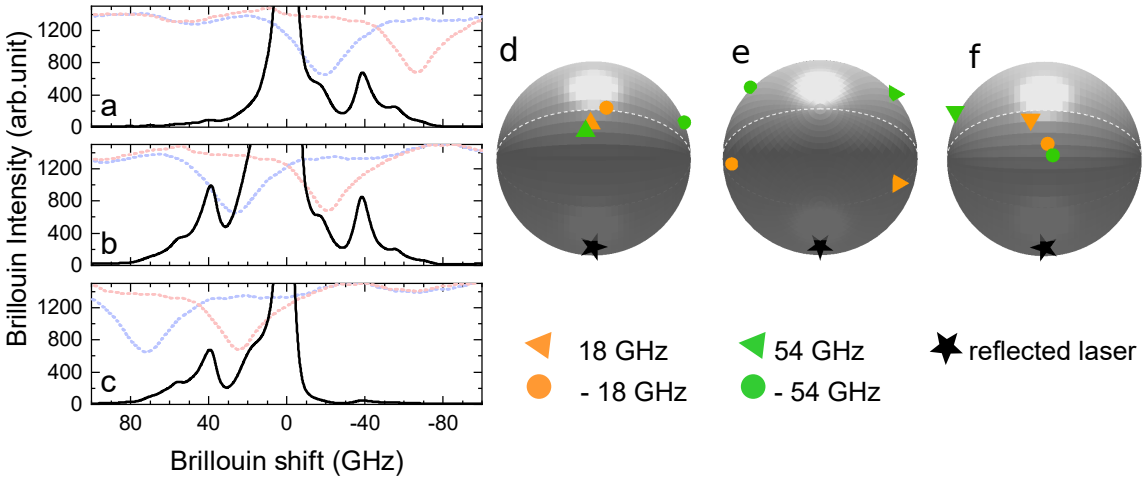

Figure 5.16: Experimental Brillouin spectra acquired on a micropillar with $e = 0.41$, with the excitation laser blue-detuned from the optical modes **a**, between the optical modes **b** and red-detuned from the optical modes **c**. The peak at ± 18 GHz corresponds to the fundamental confined acoustic mode of the resonator. The peak at ± 37 GHz corresponds to bulk Brillouin scattering from the substrate. The peak at ± 54 GHz corresponds to the third harmonic of the confined mode. **d-f** Simulated polarization of the reflected laser and Brillouin signals plotted on Poincaré spheres, using the experimental conditions of **a-c**, respectively. The Poincaré spheres are rotated such that the reflected laser state is localized at the South pole.

Figure 5.17 displays Brillouin spectra on a micropillar with $e = 0.58$. The H and V-polarized optical modes are centered at 899.550 nm and 899.823 nm, respectively. The Brillouin spectra are acquired with the laser tuned to 899.424 nm, 899.729 nm, 899.792 and 900.011 nm (panel **a**,**b**, **c** and **d**, respectively). Panels **e** to **h** show on the same sphere the matching simulated polarization states of the reflected laser, $|\psi_{refl}(\omega_{laser})\rangle$ and the Brillouin scattered signals $|\psi_B\rangle$. Here, due to the larger optical mode splitting $\Delta\lambda = 0.273$ nm we are able to simultaneously enhance the third harmonic, at ± 54 GHz, in the Stokes and anti-Stokes spectra, see panel **b**. In panel **c**, we observe the fundamental mode at -18 GHz in Stokes Brillouin scattering. The corresponding polarization states are plotted on the Poincaré sphere **g**. Both the polarization states of the -18GHz mode and of the reflected laser are on different hemispheres, resulting in a good laser filtering.

We observe that, by changing the ellipticity, we are able to selectively enhance Brillouin modes in the measured spectra. Moreover, we can independently control the polarization state of the reflected beam and Brillouin scattering.
Note that, even if the polarization state of the reflected laser $|\psi_{refl}(\omega_{laser})\rangle$ and the Brillouin scattered signals $|\psi_B\rangle$ stay on the same hemisphere of the Poincaré sphere, this is sufficient to filter out the laser and acquire Stokes Brillouin spectra with frequencies going from 18 GHz to 90 GHz. Similarly, anti-Stokes Brillouin spectra can be acquired with frequencies going from -18 GHz to -90 GHz.

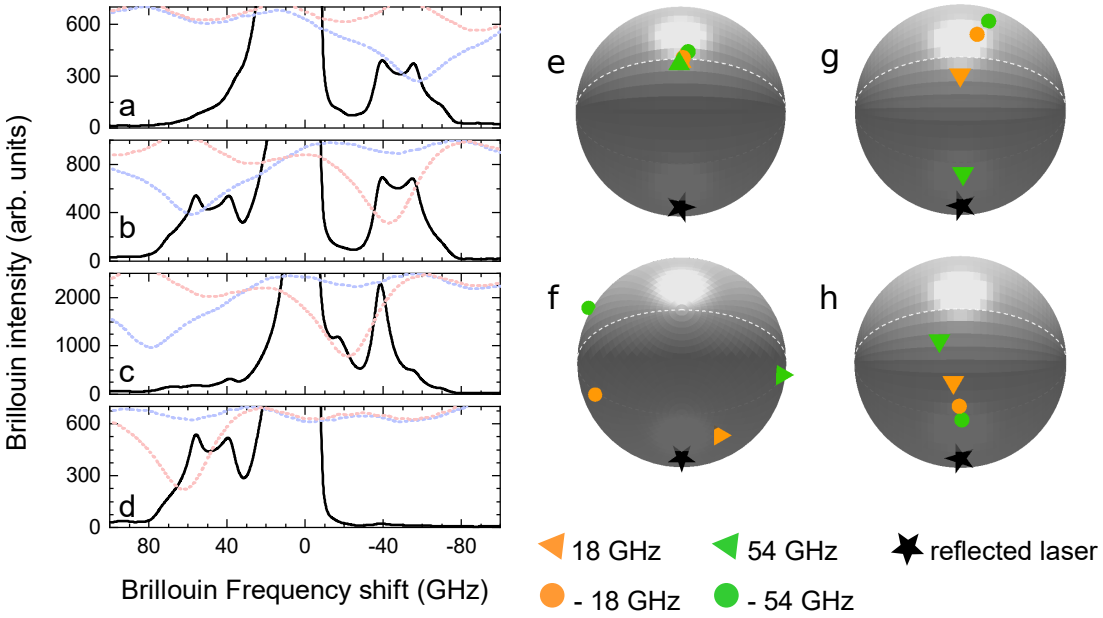

Figure 5.17: Experimental Brillouin spectra acquired on a micropillar with $e = 0.58$, with the excitation laser blue-detuned from the optical modes **a**, between the optical modes **b,c** and red-detuned from the optical modes **d**. The peak at ± 18 GHz corresponds to the fundamental confined acoustic mode of the resonator. The peak at ± 37 GHz corresponds to bulk Brillouin scattering from the substrate. The peak at ± 54 GHz corresponds to the third harmonic of the confined mode. **e-h** Simulated polarization of the reflected laser and Brillouin signals plotted on Poincaré spheres, using the experimental conditions of **a-d**, respectively. The Poincaré spheres are rotated such that the reflected laser state is localized at the South pole.

In the experiments presented above, the polarization of the incident beam is always fixed to $|D\rangle$. In that configuration, the laser is equally projected on $|H\rangle$ and $|V\rangle$. As a result, the coupling of the laser with the optical modes only depends on the laser wavelength. Moreover, it is relatively straightforward to experimentally ensure that the laser is in $|D\rangle$ in a cross-polarized setup, by looking at the reflectivity spectrum with rotation of polarization, as in Fig.5.10 for example. In Appendix C, we discuss the effect of the polarization of the incident laser on the efficiency of the Brillouin filtering.

5.5 Conclusions

In this chapter we have demonstrated that we are able to control the polarization state of the Brillouin scattering signal in polarization-dependent optical cavities. We first described how it is possible to independently rotate the polarization state of the reflected beam and Brillouin scattering signal in a micropillar with elliptical cross-section. Then, we presented the experimental setup enabling us to measure Brillouin spectra in the range of few tens of GHz.
The experimental results show that we are able to measure both Stokes and anti-Stokes modes from ± 18 GHz to ± 90 GHz in a 3D resonator. This is a technical challenge, since the low difference in wavelength between the Brillouin signal and the laser does not allow wavelength filtering and the spatial mode matching of both fields prevents us from applying spatial filtering. We exploit the wavelength-dependent polarization-rotation induced by the ellipticity to independently control the polarization state of the Brillouin signal and the reflected excitation laser to filter out the signal of interest.
As a consequence, we bend the polarization selection rules of Brillouin scattering. By controlling the shape of the micropillars, we deterministically control the polarization state of the Brillouin signal. Moreover, the polarization of different Brillouin modes can be independently controlled. The principle that we exploit here is similar to birefringent materials that scatter light with an energy dependent change of polarization [143, 144]. In the case of micropillars with elliptical cross-sections the birefringence is tuned to control the extent of rotation of polarization, whereas in birefringent materials the change in polarization depends on the penetration depth in the material.
We investigated different parameters controlling the polarization state of Brillouin scattering: the laser wavelength, the ellipticity of the cross-section and the polarization state of the incident laser. In complement to the Brillouin spectroscopy experiments, we performed simulations of the different polarization states which support the experimental spectra. The ideal conditions to measure background-free enhanced spontaneous Brillouin scattering spectra with the best filtering possible is an interplay between the ellipticity of the cross-section, the wavelength and polarization state of the laser and the coupling of the Brillouin mode to the optical cavity modes. The same working principle applies to any photonic system with localized, polarization-sensitive modes, such as plasmonic resonators, photonic crystals, and birefringent micro and nano-structures [159–161].

Main contributions:

- Modification of the Brillouin scattering polarization selection rules using micropillars with an elliptical cross-section
- Implementation of a novel Brillouin spectroscopy scheme based on polarization filtering

Conclusions and perspectives

The engineering of high-frequency mechanical vibrations at the nanoscale paves the way to the development of a broad variety of technologies. The interaction of phonons with photons and electrons make them a versatile platform with a large range of applications [1]. These include thermal transport management [80, 162], quantum technologies [37, 110], sensing [14, 163] and lasers [26, 74]. Therefore, it is essential to control phonon propagation, confinement and detection at the nanoscale. GaAs/AlAs-based acoustic superlattices can be used to manipulate the confinement of ultrahigh-frequency acoustic waves [50, 83]. Acoustic mirrors, Fabry-Perot cavities, filters, or acoustic potentials can be engineered by controlling the phonon propagation in superlattices [41, 46, 47]. Moreover, GaAs/AlAs-based resonators have well-known optical properties. GaAs/AlAs micropillar cavities confine light in three dimensions, making them suitable for quantum technologies based on quantum dots and quantum wells [52, 164, 165]. In this thesis, we have investigated optophononic multilayer devices working in the $20-300$ GHz frequency range. We designed samples that simultaneously confine light in the near-infrared range and sound at frequency of few tens of GHz and developed experimental techniques to detect the confined acoustic mode through Brillouin spectroscopy.

The first research line concentrated on the engineering of nanophononic resonators and novel strategies to confine phonons in multilayer systems. By benefiting from the topological properties of the superlattices it is possible to create interface states. The strategy involves the variation in the thickness ratio of the two materials constituting the unit cell to induce a modification in the symmetry of the modes around a bandgap that can be associated to the Zak phase of the bands [120, 130]. By concatenating two DBRs with opposite symmetry properties, it is possible to create an interface state. In Chapter 3, we presented a repertoire of topological resonators for which we extended this principle to create acoustic interface states at high-order bandgaps. We designed versatile topological devices with nanophononic interface states simultaneously created in a broad frequency range. In addition, we presented interface states of hybrid structures that combine two superlattices containing bandgaps of different orders centered around the same acoustic frequency. Furthermore, the colocalization of light and sound in GaAs/AlAs multilayers results in the band inversion simultaneously occurring in both domains. As a consequence, topological acoustic resonators at a frequency around 18 GHz are also topological optical resonators at a wavelength around 920 nm, leading to enhanced optophononic interactions.
Our second research line consisted in developing experimental Brillouin spectroscopy schemes to access confined acoustic modes at a resonance frequency around 18 GHz.

Experimental techniques to measure thermal fluctuations are of great interest in the context of cavity optomechanics. For acoustic phonons with frequencies at 18 GHz, the small wavelength shift between the intense reflected laser and the weak Brillouin signal makes the access to the Brillouin signal a challenge in standard double-chamber spectrometers. Chapter 4 was dedicated to the implementation of a Brillouin experimental scheme on planar cavities, while Chapter 5 was focused on Brillouin spectroscopy on micropillar cavities.
In planar cavities, the double optical resonance simultaneously enhances the incident laser and the scattered Brillouin signal [100]. This results in an angular offset between the reflected laser and the scattered signal. In Chapter 4, we proposed an experimental technique based on the double optical resonance to perform Brillouin spectroscopy at high frequencies on one-dimensional optophononic Fabry-Perot resonators. We used a single-mode fiber to spatially filter the Brillouin signal, while exciting the sample with an angle of incidence θ_{in}. In addition, we used a tandem of an etalon and a double spectrometer to spectrally filter out the laser and increase the resolution of the spectra. This technique shows its full potential at 18 GHz. In that case, both the laser and the Brillouin signal are tuned with an angle of incidence, improving the spatial filtering with the single-mode fiber.
While the previous technique is adapted to planar cavities, it is not suitable for micropillar cavities for which the main challenge to perform Brillouin spectroscopy measurements is that the spatial mode of the reflected laser and of the Brillouin signal overlap. In Chapter 5, we presented an experimental technique for Brillouin spectroscopy on micropillars with an elliptical cross-section to control the polarization of the different beams. Elliptical micropillar resonators have polarization-dependent optical resonances that induce wavelength-dependent rotation of polarization when the incident beam polarization is not aligned with an eigenmode of the cavity. Due to the wavelength shift between the reflected laser and the Brillouin scattering signal, they obtain different polarization states. Thus, by inducing an artificial shape-dependent birefringence, the intrinsic polarization selection rules of Brillouin scattering in GaAs/AlAs can be altered. We benefit from this to filter out the laser on the basis of polarization.

One perspective of this work is to engineer the confined acoustic modes in multilayered systems to design new devices for different application purposes.
The first design could be a multilayer structure with a surface acoustic mode. In contrast to Fabry-Perot resonators, where the mode is confined in a spacer in between two DBRs, we can benefit from the difference in acoustic impedance between GaAs and air to generate a surface mode [166]. This structure could be integrated with other systems for sensing applications or actuation. For example, mesoporous thin film layers could be deposited at the surface of an open acoustic cavity to act as a spacer. Mesoporous materials present adaptable mesopores which allows chemical functionalization under liquid infiltration [167–170]. The functionalization modifies the elastic properties of the material, which changes the acoustic resonance. Mesoporous materials present the advantage of being easily accessible and their growth is fully controlled. By combining them with multilayered acoutic cavities, they are a promising platform for nanoacoustic sensing. The DBR-based open cavity could also be integrated with two-dimensional

materials like transition metal dichalcogenide or graphene that can be used to obtain tunable phonon transducers. [171, 172].

A second category of devices we could conceive are quasi-periodic multilayered structures based on the Fibonacci and Aubry-André models, with GaAs and AlAs layers as building blocks for the series. These structures present different types of topological states such as: localized, extended or critical modes [173–175]. Multilayered quasicrystals designed according to higher-order Fibonacci sequences are large structures with layer thicknesses covering multiple scales. The short acoustic wavelengths in GaAs/AlAs associated to high-frequency acoustic phonons enables us to grow layers with thicknesses going from few nm to few µm, limiting the overall size of the structure. In addition, the linear dispersion relation of acoustic phonons enables to study localization phenomena in quasicrystals designed according to higher-order Fibonacci sequences, inaccessible in optics or electronics. The localized acoustic phonons can be experimentally accessed through prump-probe spectroscopy and inelastic Brillouin scattering spectroscopy. These devices can be fabricated by molecular beam epitaxy (MBE) that enables a precise control over the thickness of each layer at the atomic scale. The structures can thus be fabricated to operate from the gigahertz up to the terahertz range.

In terms of Brillouin spectroscopy, the experimental approach we proposed here allows us to measure 18 GHz acoustic modes on micropillars resonators. A perspective of this work would be to implement noise spectroscopy measurements coupled to the optimized measurement schemes developed in this thesis. We would then be able to study resonators with acoustic frequencies considerably higher than the state of the art in optomechanics. Noise spectroscopy measurements are widely used in optomechanics to access the phononic population in acoustic resonators, as well as to study optomechanical backaction [33, 105, 110]. The standard detection equipment is optimized to perform experiments on optomechanical systems with an optical resonance in the mid-infrared (around 1.5 µm), with large optical Q-factor and an acoustic mode at low frequency (up to few GHz). Thus, performing sensitive measurement on an optomechanical system with high-frequency acoustic modes at 18 GHz and an optical wavelength resonant in the NIR range ($\sim$920 nm) is a challenge. Some experimental details must be considered. The detection system, comprising a photodetector and a spectrum analyzer, requires a large acoustic frequency bandwidth with a high sensitivity in the NIR range. To perform this experiment, there are three major parameters to control. First, the laser power needs to be large enough to have a signal-to-noise ratio observable by the detection line. However, it is limited by the saturation power of the detector and by the minimal power inducing phonon lasing. Second, the laser wavelength should be tuned to the position of the highest sensitivity, at the slope of the optical mode. Third, the spectrum analyzer resolution bandwidth and frequency span have to be carefully tuned according to the characteristics of the signal of interest.
The signal of interest is rather weak compared to the noise levels of the photodetector and spectrum analyzer and it might be particularly difficult to detect it. To address this issue, improvements could be done to the setup: implementing a homodyne detection with a balanced photodetector would increase the signal-to-noise ratio. A way of

improving the signal intensity would be to enhance the photoelastic interaction in the micropillar. Etching micropillars with a smaller radius to increase the lateral confinement of the phonons or modifying the GaAs/AlAs thickness ratio in the unit cell of the DBRs would enhance the Brillouin-cross section. Another alternative to optimize the measurement of thermal fluctuations in GaAs/AlAs Fabry-Perot optophononic resonators would be to design resonators that confine phonons at a frequency $\sim$13 GHz, corresponding to an optical wavelength of 1.3 µm. In that case, the resonant optical wavelength and acoustic frequency would fall in the maximum of sensitivity of the photodetector and spectrum analyzer, resulting in an improved ability to measure Brownian motion.

Finally, GaAs/AlAs-based micropillars are suitable platforms towards the quantum regime. Optophononic micropillars can host quantum dots, whose optical excitation can be mediated by phonons [52]. Controlling the state of a quantum dot embedded in an optophononic resonator with confined high frequency cavity phonons would offer a novel degree of freedom for the operation of quantum systems. It would also be possible to generate single phonons through the emission of single photons.

The ultimate control of acoustic nanowaves in optophononic systems and the development of adaptive spectroscopy schemes like the ones developed in this thesis constitute an essential step toward the study of optomechanical systems at ultrahigh acoustic frequencies. The engineering of acoustic phonons has strong implications on the development of novel quantum and classical applications where phonons can be used to probe and actuate nanodevices.

List of publications

- Multiple topological states in nanophononic superlattice devices

  A. Rodriguez, E. Cardozo de Oliveira, N.D. Lanzillotti-Kimura.
  In progress

- Elliptical micropillars for efficient generation and detection of coherent acoustic phonons

  A. Rodriguez, C. Xiang, E. Cardozo de Oliveira, L. Le Gratiet, I. Sagnes, M. Morassi, A. Lemaître, and N.D. Lanzillotti-Kimura
  In progress

- Brillouin scattering selection rules in polarization-sensitive photonic resonators

  A. Rodriguez, P. Priya, E. C. de Oliveira, L. L. Gratiet, I. Sagnes, M. Morassi, A. Lemaître, F. Pastier, L. Lanco, M. Esmann, and N. D. Lanzillotti-Kimura.
  arXiv:2209.12659 [cond-mat, physics:physics], Sept. 2022.

- Simultaneous confinement of acoustic phonons and near infrared photons in GaAs/AlAs multilayers by band inversion

  P. Priya, A. Rodriguez, O. Ortiz, A. Lemaitre, M. Esmann, and N. D. Lanzillotti-Kimura.
  in Nanoengineering: Fabrication, Properties, Optics, Thin Films, and Devices XIX, Vol. **12202**, pp. 45–57 (Oct. 2022).

- Topological optical and phononic interface mode by simulta- neous band inversion

  O. Ortiz, P. Priya, A. Rodriguez, A. Lemaitre, M. Esmann, and N.D. Lanzillotti-Kimura.
  Optica **8**, 598 (2021).

- Fiber-based angular filtering for high-resolution Brillouin spectroscopy in the 20-300 GHz frequency range

  A. Rodriguez, P. Priya, O. Ortiz, P. Senellart, C Gomez-Carbonell, A. Lemaître, M. Esmann, and N.D. Lanzillotti-Kimura.
  Optics Express **29**, 2637 (2021).

- Fiber-integrated microcavities for efficient generation of co- herent acoustic phonons

  O. Ortiz, F. Pastier, A. Rodriguez, P. Priya, A. Lemaitre, C. Gomez-Carbonell, I. Sagnes, A. Harouri, P. Senellart, V. Giesz, M. Esmann, and N.D. Lanzillotti-Kimura.
  Applied Physics Letters **117**, 183102 (2020).

Appendix A

Macroscopic description of the Raman scattering process

In this section we present the process of Raman scattering using a macroscopic description from which we can obtain the polarization selection rules. This method is described in details in reference [84]. Let us consider an electromagnetic plane wave propagating in a semiconductor material. The electric field is given by:

$$\vec{E}(\vec{r},t) = \vec{E}_i(\vec{k}_i,t) \times \cos(\vec{k}_i \cdot \vec{r} - \omega_i t), \tag{A.1}$$

where $\vec{k}_i$ is the incident optical wavevector and ω_i is angular frequency. The electromagnetic wave in the medium causes a sinusoidal polarization wave:

$$\vec{P}(\vec{r},t) = \vec{P}_i(\vec{k}_i,t) \times \cos(\vec{k}_i \cdot \vec{r} - \omega_i t) \tag{A.2}$$

The polarization of the medium is related to the electromagnetic wave by the electric susceptibility tensor of the material χ:

$$\vec{P}(\vec{r},t) = \vec{\chi}(\vec{k}_i,\omega_i) \times \vec{E}(r,t). \tag{A.3}$$

Due to thermal excitation, the atoms in the lattice vibrate. The resulting atomic displacement can be expressed as a plane wave:

$$\vec{u}(\vec{r},t) = \vec{u}(\vec{q},\omega_{ac}) \times \cos(\vec{q} \cdot \vec{r} - \omega_{ac} t), \tag{A.4}$$

where $\vec{q}$ is the phonon wavevector and ω_{ac} is the acoustic frequency.
The phonon displacement causes fluctuations in the electric susceptibility. In an adiabatic approximation (i.e. the electrons adiabatically follow the atomic displacement), the electric susceptibility χ can thus be expressed as a function of $\vec{u}(\vec{r},t)$ and expanded as a Taylor series. We can then formulate the polarization wave with an acoustic wave propagating in the medium as:

$$\vec{P}(\vec{r},t,\vec{u}) = \vec{\chi}(\vec{k}_i,\omega_i,\vec{u}) \times \vec{E}(r,t). \tag{A.5}$$

The polarization wave can be separated into two terms:

$$\vec{P}(\vec{r},t,\vec{u}) = \vec{P}_0 + \vec{P}_{ind}, \tag{A.6}$$

where $\vec{P}_0$ is the polarization without perturbation in the system and $\vec{P}_{ind}$ is the polarization induced by an acoustic wave propagating in the system. The two terms are expressed as

$$\vec{P}_0(\vec{r},t,\vec{u}) = \vec{\chi}_0(\vec{k}_i,\omega_i,\vec{u})\vec{E}_i(\vec{k}_i,t) \times \cos(\vec{k}_i\cdot\vec{r}-\omega_i t) \tag{A.7}$$

and

$$\begin{aligned}\vec{P}_{ind}(\vec{r},t,\vec{u}) \;=\; & \frac{1}{2}\left.\frac{\partial\chi}{\partial\vec{u}}\right|_0 \vec{u}(\vec{q},\omega_{ac})\vec{E}_i(\vec{k}_i,\omega_i) \quad \times \\ & \left\{\cos[(\vec{k}_i-\vec{q})\cdot\vec{r}-(\omega_i-\omega_{ac})t]+\cos[(\vec{k}_i+\vec{q})\cdot\vec{r}-(\omega_i+\omega_{ac})t]\right\}.\end{aligned} \tag{A.8}$$

$\vec{P}_{ind}(\vec{r},t,\vec{u})$ is constituted of two sinusoidal waves shifted by a frequency ω_{ac} from the frequency of the incident wave. Those two contributions are the sources of the scattered fields known as Stokes and anti-Stokes scattering. Both fields verify the energy and wavevector conservation. Stokes scattering is an optical plane wave with a wavevector $\vec{k}_S = \vec{k}_i - \vec{q}$ and a frequency $\omega_S = \omega_i - \omega_{ac}$. Anti-Stokes scattering is an optical wave with a wavevector $\vec{k}_{aS} = \vec{k}_i + \vec{q}$ and a frequency $\omega_{aS} = \omega_i + \omega_{ac}$.

Polarization selection rules

The intensity of the scattered field depends on its polarization $\vec{e}_s$ as $|\vec{P}_{ind}\cdot\vec{e}_s|^2$. If we define the polarization of the incident beam $\vec{e}_i$, the intensity of the scattered field is proportional to

$$I_S \propto \left|\vec{e}_i\cdot\left.\frac{\partial\chi}{\partial\vec{u}}\right|_0 \vec{u}(\omega_{ac})\cdot\vec{e}_s\right|^2 \tag{A.9}$$

We define the Raman tensor to be $R = (\partial\chi/\partial\vec{u})_0\vec{u}(\omega_{ac})$. The Raman polarization selection rules are defined by the symmetries of this tensor. Moreover, the Raman active modes depend on the orientation of the incident wavevector to the lattice and on the incident polarization. For some geometries, the scattered field intensities vanish.
In this thesis, we consider inelastic scattering in GaAs and AlAs, which are zinc-blende-type semiconductors. The samples are grown along the (001) direction. We regard a backscattering and forward scattering configuration where $\vec{k}_i$ and $\vec{k}_{S/aS}$ are anti-parallel. For longitudinal optical phonons the polarization is preserved. That is the scattered light and the reflected laser have parallel polarizations [84]. Note that the development described here is only valid for optical phonons.

Appendix B

The Jones matrices formalism

The Jones formalism is employed to describe the polarization state of a plane wave and its evolution through an optical system. In this formalism, each optical element is represented by a Jones matrix (see Table B.1) in the H/V polarization basis. The polarization of the incident beam before the the sample is controlled by θ_1 and θ_2, the angles of the quarter and half waveplates with their fast axis, respectively. The rotation of the waveplates is then defined using the following rotation matrix:

$$M = \begin{bmatrix} cos(\theta) & -sin(\theta) \\ sin(\theta) & cos(\theta) \end{bmatrix} \tag{B.1}$$

The Jones matrix of the sample is given by:

$$M_{sample} = \begin{bmatrix} r_H & 0 \\ 0 & r_V \end{bmatrix}, \tag{B.2}$$

where $r_{H/V}$ are the reflectivity coefficients defined in equations 5.8-5.9. The reflectivity contrast, resonance wavelength and linewidth of the modes are obtained by fitting the experimental reflectivity of the elliptical micropillar with the Lorentzian model. The different optical elements are described by the following Jones matrices:

linear H polarizer	$P_H = \begin{bmatrix} 1 & 0 \\ 0 & 0 \end{bmatrix}$
linear V polarizer	$P_V = \begin{bmatrix} 0 & 0 \\ 0 & 1 \end{bmatrix}$
quarter waveplate	$W_{\lambda/4} = e^{-i\pi/4} \begin{bmatrix} 1 & 0 \\ 0 & -i \end{bmatrix}$
half waveplate	$W_{\lambda/2} = \begin{bmatrix} 1 & 0 \\ 0 & -1 \end{bmatrix}$

Table B.1: Jones matrices of waveplates and polarizers in the H/V basis [157]

Appendix C

Influence of the polarization state of the laser on the Brillouin polarization state

We consider the elliptical pillar studied in Fig.5.16 in the cases where the laser is blue and red-detuned as in panels **a** and **d** of Fig.C.1, respectively. We numerically vary the polarization of the incident beam while keeping the laser wavelength fixed. Figure C.1**b,c** and **e,f** show the filtering efficiency, that is the contrast between the polarization state of the reflected laser $|\psi_{refl}(\omega_{laser})\rangle$ and the polarization state of the Brillouin scattering of the fundamental acoustic mode $|\psi_B(\pm 18GHz)\rangle$. The filtering efficiency is maximum (i.e = 2) when both fields have polarization states on opposite poles of the Poincaré sphere. Panels **b** and **c** of Fig.C.1 show the filtering efficiency as a function of the laser polarization state for the anti-Stokes and Stokes Brillouin signal of the fundamental acoustic mode at 18 GHz when the laser is blue-detuned, respectively. The overall pattern is similar in both cases: there is a large area centered around $|V\rangle$ where the filtering is maximum. The Stokes signal is coupled to the optical cavity modes and is thus more sensitive to polarization changes. As a consequence, the filtering is more efficient for the mode in Stokes scattering than in anti-Stokes. Panels **e** and **f** of Fig.C.1 show the filtering efficiency as a function of the laser polarization state for the anti-Stokes and Stokes Brillouin signal of the fundamental acoustic mode at 18 GHz when the laser is red-detuned, respectively. The Poincaré spheres are mirrored to the previous case, with the maximum of efficiency centered around $|H\rangle$. Here, the anti-Stokes signal is resonant with the optical modes, resulting in a more efficient filtering.
Note that in the experiment we fixed the polarization of the incident laser to $|D\rangle$, as indicated on the Poincaré spheres of Fig.C.1 with black dots. According to the simulations, the filtering is not the most effective for this polarization.

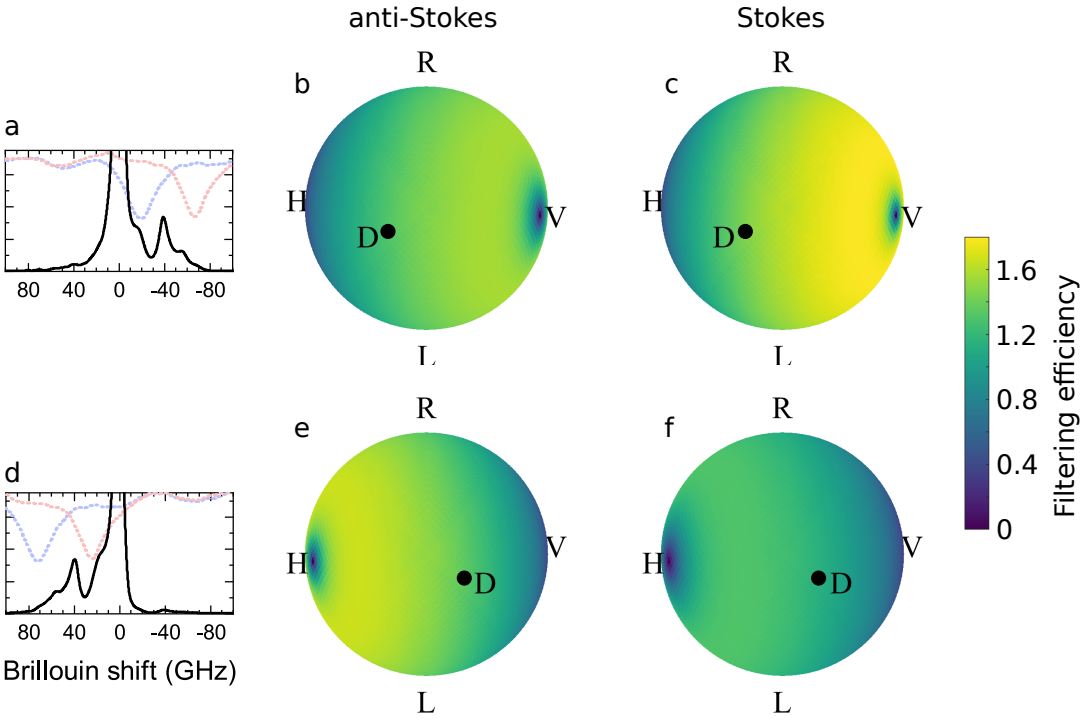

Figure C.1: Experimental Brillouin spectra acquired on a micropillar with $e = 0.41$, with the excitation laser **a** blue-detuned from the optical modes and **d** red-detuned from the optical modes. **b** and **c** show the filtering efficiency of the fundamental mode at 18 GHz in anti-Stokes and Stokes Brillouin scattering as a function of the incident polarization state for the blue detuned laser. Likewise, **e** and **f** show the filtering efficiency of the fundamental mode at 18 GHz in anti-Stokes and Stokes Brillouin scattering as a function of the incident polarization state for the red-detuned laser. The black dots indicate the polarization state of the incident laser in the experiment.

In order to find the optimal filtering conditions, let us tune the laser wavelength over the cavity modes. We extract the maximum of filtering efficiency as a function of the laser wavelength. Figure C.2 shows Poincaré spheres where we plot the polarization of the incident laser that gives the best Brillouin filtering for the anti-Stokes and Stokes fundamental mode at ± 18 GHz (panel **a** and **b**, respectively) and mode at ± 54 GHz (panel **c** and **d**, respectively) as a function of wavelength. When the laser is tuned outside of the two optical cavity modes, the polarization state of the incident laser behaves similarly depending on the wavelength for the four cases. When the laser is blue-detuned from the optical cavity modes, the optimal polarization of the incident beam has a ring-shape centered around $|V\rangle$ and centered around $|H\rangle$ when the laser is red-detuned. The incident polarization is never purely $|V\rangle$ or $|H\rangle$, since that would prevent any rotation of polarization of the different fields. However, when the laser is between the cavity modes, the polarization state of the incident beam evolves differently as a function of wavelength. The transition from the $|V\rangle$ side of the sphere to the $|H\rangle$ side happens at longer wavelengths in the case of anti-Stokes scattering than Stokes scattering, and more particularly for the mode at 54 GHz. On the contrary, the mode at -54 GHz in Stokes scattering goes from $|V\rangle$ to $|H\rangle$ at lower wavelengths. The polarization of the incident beam is further scattered toward $|D\rangle$ in the case of the

mode at ±54 GHz. From this simulation, we observed that the experimental polarization scheme that we initialized is not the most effective for our objective. Indeed by fixing the polarization state of the incident laser to $|D\rangle$, we cannot achieve an optimal filtering. Nevertheless, for certain wavelengths the incident polarization state is approaching $|D\rangle$. Therefore, by adjusting the polarization state of the incident laser in the experiment, it should be possible to increase the signal to noise ratio. Note that the model used here does not take into account the mismatch between the spatial modes of the incident beam (circular Gaussian shape) and of the micropillar (elliptical cross-section) that contributes to uncertainty in the actual projection of the polarization on the H/V basis of the micropillar. Nevertheless, we are able to measure Brillouin scattering spectra with an excellent laser rejection. The achieved filtering with an incident beam diagonally polarized is above average.

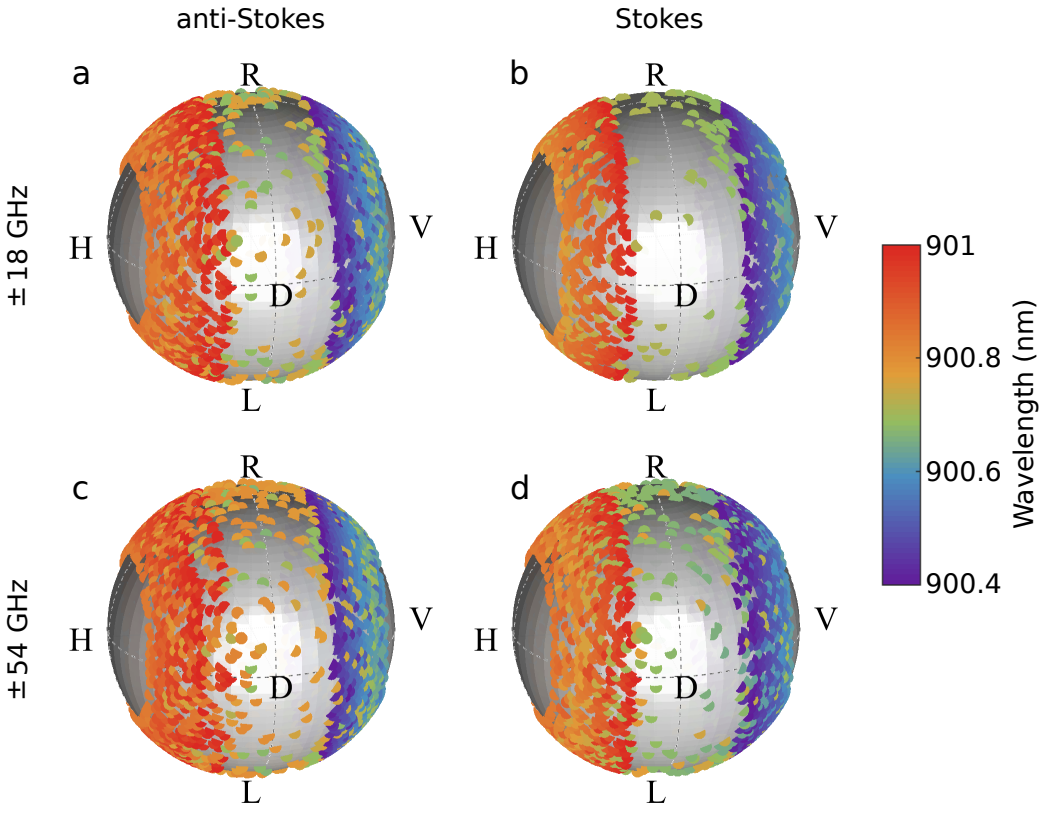

Figure C.2: Incident polarization as function of wavelength giving the best polarization filtering of the fundamental acoustic mode at ±18 GHz in **a** anti-Stokes and **b** Stokes Brillouin scattering. Similarly for the mode at ±54 GHz in **c** anti-Stokes and **d** Stokes Brillouin scattering. The mode splitting and reflectivity characteristics of the micropillar are the ones of the studied micropillar with $e = 0.41$.

It is important to mention that the best filtering does not mean that the mode is observable with the best contrast. The amplitude of the Brillouin spectrum also depends on the coupling with the optical modes, which is defined by the incident wavelength and polarization [46, 91]. Therefore, the polarization of the incident beam is a compromise between the one giving the best polarization and the one giving the best coupling with the optical modes.

Bibliography

[1]S. Volz, J. Ordonez-Miranda, A. Shchepetov, M. Prunnila, J. Ahopelto, T. Pezeril, G. Vaudel, V. Gusev, P. Ruello, E. M. Weig, M. Schubert, M. Hettich, M. Grossman, T. Dekorsy, F. Alzina, B. Graczykowski, E. Chavez-Angel, J. Sebastian Reparaz, M. R. Wagner, C. M. Sotomayor-Torres, S. Xiong, S. Neogi, and D. Donadio, "Nanophononics: state of the art and perspectives", The European Physical Journal B **89**, 15 (2016).

[2]A. A. Balandin, "Nanophononics: Phonon Engineering in Nanostructures and Nanodevices", Journal of Nanoscience and Nanotechnology **5**, 1015–1022 (2005).

[3]N. D. Lanzillotti-Kimura, A. Fainstein, A. Lemaître, and B. Jusserand, "Nanowave devices for terahertz acoustic phonons", Applied Physics Letters **88**, 083113 (2006).

[4]A. O. Krushynska, D. Torrent, A. M. Aragón, R. Ardito, O. R. Bilal, B. Bonello, F. Bosia, Y. Chen, J. Christensen, A. Colombi, S. A. Cummer, B. Djafari-Rouhani, F. Fraternali, P. I. Galich, P. D. Garcia, J.-P. Groby, S. Guenneau, M. R. Haberman, M. I. Hussein, S. Janbaz, N. Jiménez, A. Khelif, V. Laude, M. J. Mirzaali, P. Packo, A. Palermo, Y. Pennec, R. Picó, M. R. López, S. Rudykh, M. Serra-Garcia, C. M. S. Torres, T. A. Starkey, V. Tournat, and O. B. Wright, "Emerging topics in nanophononics and elastic, acoustic, and mechanical metamaterials: an overview", Nanophotonics, `10.1515/nanoph-2022-0671` (2023).

[5]J. Ragland, S. Abadi, and K. Sabra, "Long-term noise interferometry analysis in the northeast Pacific Ocean", The Journal of the Acoustical Society of America **151**, 194–204 (2022).

[6]B. Gomez and U. Kadri, "Earthquake source characterization by machine learning algorithms applied to acoustic signals", Scientific Reports **11**, 23062 (2021).

[7]S. Kumar and H. P. Lee, "The Present and Future Role of Acoustic Metamaterials for Architectural and Urban Noise Mitigations", Acoustics **1**, 590–607 (2019).

[8]K. Ishikawa, K. Yatabe, and Y. Oikawa, "Seeing the sound of castanets: Acoustic resonances between shells captured by high-speed optical visualization with 1-mm resolution", The Journal of the Acoustical Society of America **148**, 3171–3180 (2020).

[9]H. Boutin, N. Fletcher, J. Smith, and J. Wolfe, "Relationships between pressure, flow, lip motion, and upstream and downstream impedances for the trombone", The Journal of the Acoustical Society of America **137**, 1195–1209 (2015).

[10]J. Harrington, M. Gubian, M. Stevens, and F. Schiel, "Phonetic change in an Antarctic winter", The Journal of the Acoustical Society of America **146**, 3327–3332 (2019).

[11]X. Cai, H. Follet, L. Peralta, M. Gardegaront, D. Farlay, R. Gauthier, B. Yu, E. Gineyts, C. Olivier, M. Langer, A. Gourrier, D. Mitton, F. Peyrin, Q. Grimal, and P. Laugier, "Anisotropic elastic properties of human femoral cortical bone and relationships with composition and microstructure in elderly", Acta Biomaterialia **90**, 254–266 (2019).

[12]A. Elfes, "Sonar-based real-world mapping and navigation", IEEE Journal on Robotics and Automation **3**, 249–265 (1987).

[13]M. Baudoin, J.-L. Thomas, R. A. Sahely, J.-C. Gerbedoen, Z. Gong, A. Sivery, O. B. Matar, N. Smagin, P. Favreau, and A. Vlandas, "Spatially selective manipulation of cells with single-beam acoustical tweezers", Nature Communications **11**, 4244 (2020).

[14]S. Sbarra, L. Waquier, S. Suffit, A. Lemaître, and I. Favero, "Multimode Optomechanical Weighting of a Single Nanoparticle", Nano Letters **22**, 710–715 (2022).

[15]X. Fan, A. D. Smith, F. Forsberg, S. Wagner, S. Schröder, S. S. A. Akbari, A. C. Fischer, L. G. Villanueva, M. Östling, M. C. Lemme, and F. Niklaus, "Manufacture and characterization of graphene membranes with suspended silicon proof masses for MEMS and NEMS applications", Microsystems & Nanoengineering **6**, 1–17 (2020).

[16]Priya, E. R. C. de Oliveira, and N. D. Lanzillotti-Kimura, *Perspectives on high-frequency nanomechanics, nanoacoustics, and nanophononics*, arXiv:2301.07451 [cond-mat, physics:physics, physics:quant-ph], Jan. 2023.

[17]A. Tavakoli, C. Blanc, H. Ftouni, K. J. Lulla, A. D. Fefferman, E. Collin, and O. Bourgeois, "Universality of thermal transport in amorphous nanowires at low temperatures", Physical Review B **95**, 165411 (2017).

[18]M. Nomura, J. Shiomi, T. Shiga, and R. Anufriev, "Thermal phonon engineering by tailored nanostructures", Japanese Journal of Applied Physics **57**, 080101 (2018).

[19]J.-S. Heron, C. Bera, T. Fournier, N. Mingo, and O. Bourgeois, "Blocking phonons via nanoscale geometrical design", Physical Review B **82**, 155458 (2010).

[20]M. Nomura, R. Anufriev, Z. Zhang, J. Maire, Y. Guo, R. Yanagisawa, and S. Volz, "Review of thermal transport in phononic crystals", Materials Today Physics **22**, 100613 (2022).

[21]J. Kettler, N. Vaish, L. M. de Lépinay, B. Besga, P.-L. de Assis, O. Bourgeois, A. Auffèves, M. Richard, J. Claudon, J.-M. Gérard, B. Pigeau, O. Arcizet, P. Verlot, and J.-P. Poizat, "Inducing micromechanical motion by optical excitation of a single quantum dot", Nature Nanotechnology **16**, 283–287 (2021).

[22]M. Yuan, K. Biermann, and P. V. Santos, "Manipulation of flying and single excitons by GHz surface acoustic waves", AVS Quantum Science **4**, 035901 (2022).

[23]A. Devos, F. Poinsotte, J. Groenen, O. Dehaese, N. Bertru, and A. Ponchet, "Strong Generation of Coherent Acoustic Phonons in Semiconductor Quantum Dots", Physical Review Letters **98**, 207402 (2007).

[24]Y. Chu, P. Kharel, W. H. Renninger, L. D. Burkhart, L. Frunzio, P. T. Rakich, and R. J. Schoelkopf, "Quantum acoustics with superconducting qubits", Science **358**, 199–202 (2017).

[25]D. Hatanaka, M. Asano, H. Okamoto, Y. Kunihashi, H. Sanada, and H. Yamaguchi, "On-Chip Coherent Transduction between Magnons and Acoustic Phonons in Cavity Magnomechanics", Physical Review Applied **17**, 034024 (2022).

[26]D. L. Chafatinos, A. S. Kuznetsov, S. Anguiano, A. E. Bruchhausen, A. A. Reynoso, K. Biermann, P. V. Santos, and A. Fainstein, "Polariton-driven phonon laser", Nature Communications **11**, 4552 (2020).

[27]M. Poblet, R. Berté, H. D. Boggiano, Y. Li, E. Cortés, G. Grinblat, S. A. Maier, and A. V. Bragas, "Acoustic Coupling between Plasmonic Nanoantennas: Detection and Directionality of Surface Acoustic Waves", ACS Photonics **8**, 2846–2852 (2021).

[28]A. Schliesser, R. Rivière, G. Anetsberger, O. Arcizet, and T. J. Kippenberg, "Resolved-sideband cooling of a micromechanical oscillator", Nature Physics **4**, 415–419 (2008).

[29]L. Ding, C. Baker, P. Senellart, A. Lemaitre, S. Ducci, G. Leo, and I. Favero, "High Frequency GaAs Nano-Optomechanical Disk Resonator", Physical Review Letters **105**, 263903 (2010).

[30]S. Anguiano, A. Bruchhausen, B. Jusserand, I. Favero, F. Lamberti, L. Lanco, I. Sagnes, A. Lemaître, N. Lanzillotti-Kimura, P. Senellart, and A. Fainstein, "Micropillar Resonators for Optomechanics in the Extremely High 19–95-GHz Frequency Range", Physical Review Letters **118**, 263901 (2017).

[31]M. Esmann, F. R. Lamberti, A. Harouri, L. Lanco, I. Sagnes, I. Favero, G. Aubin, C. Gomez-Carbonell, A. Lemaître, O. Krebs, P. Senellart, and N. D. Lanzillotti-Kimura, "Brillouin scattering in hybrid optophononic Bragg micropillar resonators at 300 GHz", Optica **6**, 854 (2019).

[32]J. Doster, T. Shah, T. Fösel, P. Paulitschke, F. Marquardt, and E. M. Weig, "Observing polarization patterns in the collective motion of nanomechanical arrays", Nature Communications **13**, 2478 (2022).

[33]D. Navarro-Urrios, N. E. Capuj, M. F. Colombano, P. D. García, M. Sledzinska, F. Alzina, A. Griol, A. Martínez, and C. M. Sotomayor-Torres, "Nonlinear dynamics and chaos in an optomechanical beam", Nature Communications **8**, 14965 (2017).

[34]J. Zhang, O. Ortiz, X. L. Roux, E. Cassan, L. Vivien, D. Marris-Morini, N. D. Lanzillotti-Kimura, and C. Alonso-Ramos, "Subwavelength engineering for Brillouin gain optimization in silicon optomechanical waveguides", Optics Letters **45**, 3717–3720 (2020).

[35]D. Cattiaux, I. Golokolenov, S. Kumar, M. Sillanpää, L. Mercier de Lépinay, R. R. Gazizulin, X. Zhou, A. D. Armour, O. Bourgeois, A. Fefferman, and E. Collin, "A macroscopic object passively cooled into its quantum ground state of motion beyond single-mode cooling", Nature Communications **12**, 6182 (2021).

[36]D. Saleta Reig, S. Varghese, R. Farris, A. Block, J. D. Mehew, O. Hellman, P. Woźniak, M. Sledzinska, A. El Sachat, E. Chávez-Ángel, S. O. Valenzuela, N. F. van Hulst, P. Ordejón, Z. Zanolli, C. M. Sotomayor Torres, M. J. Verstraete, and K.-J. Tielrooij, "Unraveling Heat Transport and Dissipation in Suspended MoSe2 from Bulk to Monolayer", Advanced Materials **34**, 2108352 (2022).

[37]R. Riedinger, A. Wallucks, I. Marinković, C. Löschnauer, M. Aspelmeyer, S. Hong, and S. Gröblacher, "Remote quantum entanglement between two micromechanical oscillators", Nature **556**, 473–477 (2018).

[38]G. Andersson, S. W. Jolin, M. Scigliuzzo, R. Borgani, M. O. Tholén, J. Rivera Hernández, V. Shumeiko, D. B. Haviland, and P. Delsing, "Squeezing and Multimode Entanglement of Surface Acoustic Wave Phonons", PRX Quantum **3**, 010312 (2022).

[39]Y. Chu, P. Kharel, T. Yoon, L. Frunzio, P. T. Rakich, and R. J. Schoelkopf, "Creation and control of multi-phonon Fock states in a bulk acoustic-wave resonator", Nature **563**, 666–670 (2018).

[40]M. D. Anderson, S. Tarrago Velez, K. Seibold, H. Flayac, V. Savona, N. Sangouard, and C. Galland, "Two-Color Pump-Probe Measurement of Photonic Quantum Correlations Mediated by a Single Phonon", Physical Review Letters **120**, 233601 (2018).

[41]O. Ortíz, M. Esmann, and N. D. Lanzillotti-Kimura, "Phonon engineering with superlattices: Generalized nanomechanical potentials", Physical Review B **100**, 085430 (2019).

[42]N. D. Lanzillotti-Kimura, A. Fainstein, B. Perrin, B. Jusserand, O. Mauguin, L. Largeau, and A. Lemaître, "Bloch Oscillations of THz Acoustic Phonons in Coupled Nanocavity Structures", Physical Review Letters **104**, 197402 (2010).

[43]N. D. Lanzillotti-Kimura, A. Fainstein, A. Lemaitre, B. Jusserand, and B. Perrin, "Coherent control of sub-terahertz confined acoustic nanowaves: Theory and experiments", Physical Review B **84**, 115453 (2011).

[44]C. Colvard, T. A. Gant, M. V. Klein, R. Merlin, R. Fischer, H. Morkoc, and A. C. Gossard, "Folded acoustic and quantized optic phonons in (GaAl)As superlattices", Physical Review B **31**, 2080–2091 (1985).

[45]A. J. Kent, R. N. Kini, N. M. Stanton, M. Henini, B. A. Glavin, V. A. Kochelap, and T. L. Linnik, "Acoustic Phonon Emission from a Weakly Coupled Superlattice under Vertical Electron Transport: Observation of Phonon Resonance", Physical Review Letters **96**, 215504 (2006).

[46]M. Trigo, A. Bruchhausen, A. Fainstein, B. Jusserand, and V. Thierry-Mieg, "Confinement of Acoustical Vibrations in a Semiconductor Planar Phonon Cavity", Physical Review Letters **89**, 227402 (2002).

[47]N. D. Lanzillotti-Kimura, B. Perrin, A. Fainstein, B. Jusserand, and A. Lemaître, "Nanophononic thin-film filters and mirrors studied by picosecond ultrasonics", Applied Physics Letters **96**, 053101 (2010).

[48]A. Fainstein, N. D. Lanzillotti-Kimura, B. Jusserand, and B. Perrin, "Strong Optical-Mechanical Coupling in a Vertical GaAs/AlAs Microcavity for Subterahertz Phonons and Near-Infrared Light", Physical Review Letters **110**, 037403 (2013).

[49]G. Arregui, N. Lanzillotti-Kimura, C. Sotomayor-Torres, and P. García, "Anderson Photon-Phonon Colocalization in Certain Random Superlattices", Physical Review Letters **122**, 043903 (2019).

[50]F. R. Lamberti, Q. Yao, L. Lanco, D. T. Nguyen, M. Esmann, A. Fainstein, P. Sesin, S. Anguiano, V. Villafañe, A. Bruchhausen, P. Senellart, I. Favero, and N. D. Lanzillotti-Kimura, "Optomechanical properties of GaAs/AlAs micropillar resonators operating in the 18 GHz range", Optics Express **25**, 24437–24447 (2017).

[51]O. Ortiz, P. Priya, A. Rodriguez, A. Lemaitre, M. Esmann, and N. D. Lanzillotti-Kimura, "Topological optical and phononic interface mode by simultaneous band inversion", Optica **8**, 598 (2021).

[52]S. Thomas, M. Billard, N. Coste, S. Wein, Priya, H. Ollivier, O. Krebs, L. Tazaïrt, A. Harouri, A. Lemaitre, I. Sagnes, C. Anton, L. Lanco, N. Somaschi, J. Loredo, and P. Senellart, "Bright Polarized Single-Photon Source Based on a Linear Dipole", Physical Review Letters **126**, 233601 (2021).

[53]H. Xue, Y. Yang, and B. Zhang, "Topological acoustics", Nature Reviews Materials **7**, 974–990 (2022).

[54]G. Ma, M. Xiao, and C. T. Chan, "Topological phases in acoustic and mechanical systems", Nature Reviews Physics **1**, 281–294 (2019).

[55]X. Zhang, M. Xiao, Y. Cheng, M.-H. Lu, and J. Christensen, "Topological sound", Communications Physics **1**, 1–13 (2018).

[56]L. Lu, J. D. Joannopoulos, and M. Soljačić, "Topological photonics", Nature Photonics **8**, 821–829 (2014).

[57]H. Ren, T. Shah, H. Pfeifer, C. Brendel, V. Peano, F. Marquardt, and O. Painter, "Topological phonon transport in an optomechanical system", Nature Communications **13**, 3476 (2022).

[58]P. Ruello and V. E. Gusev, "Physical mechanisms of coherent acoustic phonons generation by ultrafast laser action", Ultrasonics **56**, 21–35 (2015).

[59]F. Kargar and A. A. Balandin, "Advances in Brillouin–Mandelstam light-scattering spectroscopy", Nature Photonics **15**, 720–731 (2021).

[60]R. Prevedel, A. Diz-Muñoz, G. Ruocco, and G. Antonacci, "Brillouin microscopy: an emerging tool for mechanobiology", Nature Methods **16**, 969–977 (2019).

[61]G. Antonacci, T. Beck, A. Bilenca, J. Czarske, K. Elsayad, J. Guck, K. Kim, B. Krug, F. Palombo, R. Prevedel, and G. Scarcelli, "Recent progress and current opinions in Brillouin microscopy for life science applications", Biophysical Reviews **12**, 615–624 (2020).

[62]G. Yan, A. Bazir, J. Margueritat, and T. Dehoux, "Evaluation of commercial virtually imaged phase array and Fabry-Pérot based Brillouin spectrometers for applications to biology", Biomedical Optics Express **11**, 6933–6944 (2020).

[63]X. Wang, S.-C. Huang, S. Hu, S. Yan, and B. Ren, "Fundamental understanding and applications of plasmon-enhanced Raman spectroscopy", Nature Reviews Physics **2**, 253–271 (2020).

[64]G. Rozas, B. Jusserand, and A. Fainstein, "Fabry-Pérot-multichannel spectrometer tandem for ultra-high resolution Raman spectroscopy", Review of Scientific Instruments **85**, 013103 (2014).

[65]O. Ortiz, F. Pastier, A. Rodriguez, Priya, A. Lemaitre, C. Gomez-Carbonell, I. Sagnes, A. Harouri, P. Senellart, V. Giesz, M. Esmann, and N. D. Lanzillotti-Kimura, "Fiber-integrated microcavities for efficient generation of coherent acoustic phonons", Applied Physics Letters **117**, 183102 (2020).

[66]Z. Coker, M. Troyanova-Wood, A. J. Traverso, T. Yakupov, Z. N. Utegulov, and V. V. Yakovlev, "Assessing performance of modern Brillouin spectrometers", Optics Express **26**, 2400–2409 (2018).

[67]Y. Ike, S. Tsukada, and S. Kojima, "High-resolution Brillouin spectroscopy with angular dispersion-type Fabry-Perot interferometer and its application to a quartz crystal", Review of Scientific Instruments **78**, 076104 (2007).

[68]X.-L. Liu, H.-N. Liu, J.-B. Wu, H.-X. Wu, T. Zhang, W.-Q. Zhao, and P.-H. Tan, "Filter-based ultralow-frequency Raman measurement down to 2 cm ^{1} for fast Brillouin spectroscopy measurement", Review of Scientific Instruments **88**, 053110 (2017).

[69]G. Antonacci, S. De Panfilis, G. Di Domenico, E. DelRe, and G. Ruocco, "Breaking the Contrast Limit in Single-Pass Fabry-Pérot Spectrometers", Physical Review Applied **6**, 054020 (2016).

[70]D. Navarro-Urrios, N. E. Capuj, J. Gomis-Bresco, F. Alzina, A. Pitanti, A. Griol, A. Martínez, and C. M. Sotomayor Torres, "A self-stabilized coherent phonon source driven by optical forces", Scientific Reports **5**, 15733 (2015).

[71]B. Stiller, B. Stiller, B. Stiller, M. Merklein, M. Merklein, C. Wolff, K. Vu, P. Ma, S. J. Madden, B. J. Eggleton, and B. J. Eggleton, "Coherently refreshing hypersonic phonons for light storage", Optica **7**, 492–497 (2020).

[72]K. C. Lee, B. J. Sussman, M. R. Sprague, P. Michelberger, K. F. Reim, J. Nunn, N. K. Langford, P. J. Bustard, D. Jaksch, and I. A. Walmsley, "Macroscopic non-classical states and terahertz quantum processing in room-temperature diamond", Nature Photonics **6**, 41–44 (2012).

[73]M. Sledzinska, B. Graczykowski, J. Maire, E. Chavez-Angel, C. M. Sotomayor-Torres, and F. Alzina, "2D Phononic Crystals: Progress and Prospects in Hypersound and Thermal Transport Engineering", Advanced Functional Materials **30**, 1904434 (2020).

[74]N. T. Otterstrom, R. O. Behunin, E. A. Kittlaus, Z. Wang, and P. T. Rakich, "A silicon Brillouin laser", Science **360**, 1113–1116 (2018).

[75]P. Sesin, S. Anguiano, A. E. Bruchhausen, A. Lemaître, and A. Fainstein, "Cavity optomechanics with a laser-engineered optical trap", Physical Review B **103**, L081301 (2021).

[76]L. Qiu, I. Shomroni, P. Seidler, and T. J. Kippenberg, "Laser Cooling of a Nanomechanical Oscillator to Its Zero-Point Energy", Physical Review Letters **124**, 173601 (2020).

[77]E. Yablonovitch, "Photonic Crystals", Journal of Modern Optics **41**, 173–194 (1994).

[78]I. Ghorbel, F. Swiadek, R. Zhu, D. Dolfi, G. Lehoucq, A. Martin, G. Moille, L. Morvan, R. Braive, S. Combrié, and A. De Rossi, "Optomechanical gigahertz oscillator made of a two photon absorption free piezoelectric III/V semiconductor", APL Photonics **4**, 116103 (2019).

[79]N. D. Lanzillotti-Kimura, A. Fainstein, C. A. Balseiro, and B. Jusserand, "Phonon engineering with acoustic nanocavities: Theoretical considerations on phonon molecules, band structures, and acoustic Bloch oscillations", Physical Review B **75**, 024301 (2007).

[80]O. Florez, G. Arregui, M. Albrechtsen, R. C. Ng, J. Gomis-Bresco, S. Stobbe, C. M. Sotomayor-Torres, and P. D. García, "Engineering nanoscale hypersonic phonon transport", Nature Nanotechnology **17**, 947–951 (2022).

[81]J. Nakagawa, Y. Kage, T. Hori, J. Shiomi, and M. Nomura, "Crystal structure dependent thermal conductivity in two-dimensional phononic crystal nanostructures", Applied Physics Letters **107**, 023104 (2015).

[82]S. Yang, J. H. Page, Z. Liu, M. L. Cowan, C. T. Chan, and P. Sheng, "Focusing of Sound in a 3D Phononic Crystal", Physical Review Letters **93**, 024301 (2004).

[83]A. Crespo-Poveda, A. S. Kuznetsov, A. Hernández-Mínguez, A. Tahraoui, K. Biermann, and P. V. Santos, "GHz guided optomechanics in planar semiconductor microcavities", Optica **9**, 160 (2022).

[84]P. Y. Yu and M. Cardona, *Fundamentals of Semiconductors*, Graduate Texts in Physics (Berlin, Heidelberg, 2010).

[85]F.-R. Lamberti, "Opto-phononic confinement in GaAs/AlAs-based resonators", Theses (Université Sorbonne Paris Cité, July 2018).

[86]O. H. O. Cabello, "Coherent acoustic-phonon dynamics in GaAs/AlAs heterostructures", PhD thesis (Université Paris-Saclay, Mar. 2021).

[87]M. A. Afromowitz, "Refractive index of Ga1xAlxAs", Solid State Communications **15**, 59–63 (1974).

[88]M. De Luca, C. Fasolato, M. A. Verheijen, Y. Ren, M. Y. Swinkels, S. Kölling, E. P. A. M. Bakkers, R. Rurali, X. Cartoixà, and I. Zardo, "Phonon Engineering in Twinning Superlattice Nanowires", Nano Letters **19**, 4702–4711 (2019).

[89]M. Cardona and G. Güntherodt, eds., *Light Scattering in Solids V*, Vol. 66/1, Topics in Applied Physics (Berlin/Heidelberg, 1989).

[90]P. Lacharmoise, A. Fainstein, B. Jusserand, and V. Thierry-Mieg, "Optical cavity enhancement of light–sound interaction in acoustic phonon cavities", Applied Physics Letters **84**, 3274–3276 (2004).

[91]A. Fainstein, B. Jusserand, and V. Thierry-Mieg, "Raman efficiency in a planar microcavity", Physical Review B **53**, R13287–R13290 (1996).

[92]P. Priya, A. Rodriguez, O. Ortiz, A. Lemaitre, M. Esmann, and N. D. Lanzillotti-Kimura, "Simultaneous confinement of acoustic phonons and near infrared photons in GaAs/AlAs multilayers by band inversion", in Nanoengineering: Fabrication, Properties, Optics, Thin Films, and Devices XIX, Vol. 12202 (Oct. 2022), pp. 45–57.

[93]N. D. Lanzillotti Kimura, "Nanophononics in the GHz-THz range", Habilitation à diriger des recherches (Université Paris-Saclay, Mar. 2021).

[94]A. Mlayah, J.-R. Huntzinger, and N. Large, "Raman-Brillouin light scattering in low-dimensional systems: Photoelastic model versus quantum model", Physical Review B **75**, 245303 (2007).

[95]J. He, B. Djafari-Rouhani, and J. Sapriel, "Theory of light scattering by longitudinal-acoustic phonons in superlattices", Physical Review B **37**, 4086–4098 (1988).

[96]H. Kuzmany, *Solid-State Spectroscopy* (Springer, Berlin, Heidelberg, 2009).

[97]N. D. Lanzillotti-Kimura, A. Fainstein, B. Jusserand, and A. Lemaître, "Resonant Raman scattering of nanocavity-confined acoustic phonons", Physical Review B **79**, 035404 (2009).

[98]M. Cardona and R. Merlin, "Light Scattering in Solids IX", in *Light Scattering in Solid IX*, edited by M. Cardona and R. Merlin, Topics in Applied Physics (Berlin, Heidelberg, 2007), pp. 1–14.

[99]A. Fainstein and B. Jusserand, "Raman Scattering in Resonant Cavities", in *Light Scattering in Solid IX*, Vol. 108, edited by C. E. Ascheron, A. H. Duhm, M. Cardona, and R. Merlin, Series Title: Topics in Applied Physics (Berlin, Heidelberg, 2006), pp. 17–110.

[100]A. Fainstein, B. Jusserand, and V. Thierry-Mieg, "Raman Scattering Enhancement by Optical Confinement in a Semiconductor Planar Microcavity", Physical Review Letters **75**, 3764–3767 (1995).

[101]S. Anguiano, A. E. Bruchhausen, I. Favero, I. Sagnes, A. Lemaître, N. D. Lanzillotti-Kimura, and A. Fainstein, "Optical cavity mode dynamics and coherent phonon generation in high- Q micropillar resonators", Physical Review A **98**, 013816 (2018).

[102]N. D. Lanzillotti-Kimura, A. Fainstein, A. Huynh, B. Perrin, B. Jusserand, A. Miard, and A. Lemaître, "Coherent Generation of Acoustic Phonons in an Optical Microcavity", Physical Review Letters **99**, 217405 (2007).

[103]P. Sesin, P. Soubelet, V. Villafañe, A. E. Bruchhausen, B. Jusserand, A. Lemaître, N. D. Lanzillotti-Kimura, and A. Fainstein, "Dynamical optical tuning of the coherent phonon detection sensitivity in DBR-based GaAs optomechanical resonators", Physical Review B **92**, 075307 (2015).

[104]I. Favero and K. Karrai, "Optomechanics of deformable optical cavities", Nature Photonics **3**, 201–205 (2009).

[105]I. Yeo, P.-L. de Assis, A. Gloppe, E. Dupont-Ferrier, P. Verlot, N. S. Malik, E. Dupuy, J. Claudon, J.-M. Gérard, A. Auffèves, G. Nogues, S. Seidelin, J.-P. Poizat, O. Arcizet, and M. Richard, "Strain-mediated coupling in a quantum dot–mechanical oscillator hybrid system", Nature Nanotechnology **9**, 106–110 (2014).

[106]H. R. Böhm, S. Gigan, F. Blaser, A. Zeilinger, M. Aspelmeyer, G. Langer, D. Bäuerle, J. B. Hertzberg, and K. C. Schwab, "High reflectivity high-Q micromechanical Bragg mirror", Applied Physics Letters **89**, 223101 (2006).

[107]M. J. Burek, J. D. Cohen, S. M. Meenehan, N. El-Sawah, C. Chia, T. Ruelle, S. Meesala, J. Rochman, H. A. Atikian, M. Markham, D. J. Twitchen, M. D. Lukin, O. Painter, and M. Lončar, "Diamond optomechanical crystals", Optica **3**, 1404 (2016).

[108]A. Schliesser, P. Del'Haye, N. Nooshi, K. J. Vahala, and T. J. Kippenberg, "Radiation Pressure Cooling of a Micromechanical Oscillator Using Dynamical Backaction", Physical Review Letters **97**, 243905 (2006).

[109]S. Gröblacher, J. B. Hertzberg, M. R. Vanner, G. D. Cole, S. Gigan, K. C. Schwab, and M. Aspelmeyer, "Demonstration of an ultracold micro-optomechanical oscillator in a cryogenic cavity", Nature Physics **5**, 485–488 (2009).

[110]J. Chan, T. P. M. Alegre, A. H. Safavi-Naeini, J. T. Hill, A. Krause, S. Gröblacher, M. Aspelmeyer, and O. Painter, "Laser cooling of a nanomechanical oscillator into its quantum ground state", Nature **478**, 89–92 (2011).

[111]O. Arcizet, P.-F. Cohadon, T. Briant, M. Pinard, and A. Heidmann, "Radiation-pressure cooling and optomechanical instability of a micromirror", Nature **444**, 71–74 (2006).

[112]G. Anetsberger, O. Arcizet, Q. P. Unterreithmeier, R. Rivière, A. Schliesser, E. M. Weig, J. P. Kotthaus, and T. J. Kippenberg, "Near-field cavity optomechanics with nanomechanical oscillators", Nature Physics **5**, 909–914 (2009).

[113]C. Xiong, X. Sun, K. Y. Fong, and H. X. Tang, "GHz aluminum nitride optomechanical wheel resonators", in 2012 IEEE International Frequency Control Symposium Proceedings (May 2012), pp. 1–4.

[114]X. Zeng, W. He, M. H. Frosz, A. Geilen, P. Roth, G. K. L. Wong, P. S. Russell, and B. Stiller, "Stimulated Brillouin scattering in chiral photonic crystal fiber", Photonics Research **10**, 711 (2022).

[115]J. Asbóth, L. Oroszlány, and A. Pályi, *A Short Course on Topological Insulators*, Lecture Notes in Physics 919 (2016).

[116]C. L. Kane and E. J. Mele, "Quantum Spin Hall Effect in Graphene", Physical Review Letters **95**, 226801 (2005).

[117]T. Ozawa, H. M. Price, A. Amo, N. Goldman, M. Hafezi, L. Lu, M. C. Rechtsman, D. Schuster, J. Simon, O. Zilberberg, and I. Carusotto, "Topological photonics", Reviews of Modern Physics **91**, 015006 (2019).

[118]N. V. Hauff, H. Le Jeannic, P. Lodahl, S. Hughes, and N. Rotenberg, "Chiral quantum optics in broken-symmetry and topological photonic crystal waveguides", Physical Review Research **4**, 023082 (2022).

[119]M. Hafezi, S. Mittal, J. Fan, A. Migdall, and J. M. Taylor, "Imaging topological edge states in silicon photonics", Nature Photonics **7**, 1001–1005 (2013).

[120]M. Xiao, Z. Zhang, and C. Chan, "Surface Impedance and Bulk Band Geometric Phases in One-Dimensional Systems", Physical Review X **4**, 021017 (2014).

[121]P. St-Jean, A. Dauphin, P. Massignan, B. Real, O. Jamadi, M. Milicevic, A. Lemaître, A. Harouri, L. Le Gratiet, I. Sagnes, S. Ravets, J. Bloch, and A. Amo, "Measuring Topological Invariants in a Polaritonic Analog of Graphene", Physical Review Letters **126**, 127403 (2021).

[122]N. Pernet, P. St-Jean, D. D. Solnyshkov, G. Malpuech, N. Carlon Zambon, Q. Fontaine, B. Real, O. Jamadi, A. Lemaître, M. Morassi, L. Le Gratiet, T. Baptiste, A. Harouri, I. Sagnes, A. Amo, S. Ravets, and J. Bloch, "Gap solitons in a one-dimensional driven-dissipative topological lattice", Nature Physics **18**, 678–684 (2022).

[123]S. Klembt, T. H. Harder, O. A. Egorov, K. Winkler, R. Ge, M. A. Bandres, M. Emmerling, L. Worschech, T. C. H. Liew, M. Segev, C. Schneider, and S. Höfling, "Exciton-polariton topological insulator", Nature **562**, 552–556 (2018).

[124]M. Esmann, F. R. Lamberti, A. Lemaître, and N. D. Lanzillotti-Kimura, "Topological acoustics in coupled nanocavity arrays", Physical Review B **98**, 161109 (2018).

[125]G. Arregui, O. Ortíz, M. Esmann, C. M. Sotomayor-Torres, C. Gomez-Carbonell, O. Mauguin, B. Perrin, A. Lemaître, P. D. García, and N. D. Lanzillotti-Kimura, "Coherent generation and detection of acoustic phonons in topological nanocavities", APL Photonics **4**, 030805 (2019).

[126]M. Xiao, G. Ma, Z. Yang, P. Sheng, Z. Q. Zhang, and C. T. Chan, "Geometric phase and band inversion in periodic acoustic systems", Nature Physics **11**, 240–244 (2015).

[127]M. Esmann and N. D. Lanzillotti-Kimura, "A Topological View on Optical and Phononic Fabry–Perot Microcavities through the Su–Schrieffer–Heeger Model", Applied Sciences **8**, 527 (2018).

[128]W. P. Su, J. R. Schrieffer, and A. J. Heeger, "Solitons in Polyacetylene", Physical Review Letters **42**, 1698–1701 (1979).

[129]J. Zak, "Berry's phase for energy bands in solids", Physical Review Letters **62**, 2747–2750 (1989).

[130]M. Esmann, F. R. Lamberti, P. Senellart, I. Favero, O. Krebs, L. Lanco, C. Gomez Carbonell, A. Lemaître, and N. D. Lanzillotti-Kimura, "Topological nanophononic states by band inversion", Physical Review B **97**, 155422 (2018).

[131]S. Speziale, H. Marquardt, and T. S. Duffy, "Brillouin Scattering and its Application in Geosciences", Reviews in Mineralogy and Geochemistry **78**, 543–603 (2014).

[132]R. C. Ng, A. E. Sachat, F. Cespedes, M. Poblet, G. Madiot, J. Jaramillo-Fernandez, O. Florez, P. Xiao, M. Sledzinska, C. M. Sotomayor-Torres, and E. Chavez-Angel, "Excitation and detection of acoustic phonons in nanoscale systems", Nanoscale **14**, 13428–13451 (2022).

[133]S. M. Lindsay, M. W. Anderson, and J. R. Sandercock, "Construction and alignment of a high performance multipass vernier tandem Fabry–Perot interferometer", Review of Scientific Instruments **52**, 1478–1486 (1981).

[134]R. Mock, B. Hillebrands, and R. Sandercock, "Construction and performance of a Brillouin scattering set-up using a triple-pass tandem Fabry-Perot interferometer", Journal of Physics E: Scientific Instruments **20**, 656 (1987).

[135]F. Scarponi, S. Mattana, S. Corezzi, S. Caponi, L. Comez, P. Sassi, A. Morresi, M. Paolantoni, L. Urbanelli, C. Emiliani, L. Roscini, L. Corte, G. Cardinali, F. Palombo, J. Sandercock, and D. Fioretto, "High-Performance Versatile Setup for Simultaneous Brillouin-Raman Microspectroscopy", Physical Review X **7**, 031015 (2017).

[136]S. Anguiano, G. Rozas, A. E. Bruchhausen, A. Fainstein, B. Jusserand, P. Senellart, and A. Lemaître, "Spectra of mechanical cavity modes in distributed Bragg reflector based vertical GaAs resonators", Physical Review B **90**, 045314 (2014).

[137]F. R. Lamberti, M. Esmann, A. Lemaître, C. Gomez Carbonell, O. Krebs, I. Favero, B. Jusserand, P. Senellart, L. Lanco, and N. D. Lanzillotti-Kimura, "Nanomechanical resonators based on adiabatic periodicity-breaking in a superlattice", Applied Physics Letters **111**, 173107 (2017).

[138]A. Fainstein and B. Jusserand, "Performance of semiconductor planar microcavities for Raman-scattering enhancement", Physical Review B **57**, 2402–2406 (1998).

[139]S. Flågan, P. Maletinsky, R. J. Warburton, and D. Riedel, "Microcavity platform for widely tunable optical double resonance", Optica **9**, 1197–1209 (2022).

[140]G. Antonacci, G. Lepert, C. Paterson, and P. Török, "Elastic suppression in Brillouin imaging by destructive interference", Applied Physics Letters **107**, 061102 (2015).

[141]M. S. Kang, A. Brenn, and P. St.J. Russell, "All-Optical Control of Gigahertz Acoustic Resonances by Forward Stimulated Interpolarization Scattering in a Photonic Crystal Fiber", Physical Review Letters **105**, 153901 (2010).

[142]G. Bashan, H. H. Diamandi, Y. London, K. Sharma, K. Shemer, E. Zehavi, and A. Zadok, "Forward stimulated Brillouin scattering and opto-mechanical non-reciprocity in standard polarization maintaining fibres", Light: Science & Applications **10**, 119 (2021).

[143]P. Alonso-Gutiérrez, M. L. Sanjuán, and M. C. Morón, "Raman selection rules in uniaxial media: The nonpolar modes of $\mathrm{Mn}{\mathrm{Ga}}_{2}{\mathrm{Se}}_{4}$", Physical Review B **71**, 085205 (2005).

[144]C. Kranert, C. Sturm, R. Schmidt-Grund, and M. Grundmann, "Raman Tensor Formalism for Optically Anisotropic Crystals", Physical Review Letters **116**, 127401 (2016).

[145]B. Gayral, J. M. Gérard, B. Legrand, E. Costard, and V. Thierry-Mieg, "Optical study of GaAs/AlAs pillar microcavities with elliptical cross section", Applied Physics Letters **72**, 1421–1423 (1998).

[146]D. M. Whittaker, P. S. S. Guimaraes, D. Sanvitto, H. Vinck, S. Lam, A. Daraei, J. A. Timpson, A. M. Fox, M. S. Skolnick, Y.-L. D. Ho, J. G. Rarity, M. Hopkinson, and A. Tahraoui, "High Q modes in elliptical microcavity pillars", Applied Physics Letters **90**, 161105 (2007).

[147]B. Gayral, "Modification de l'emission spontanee de boites quantiques semi-conductrices dans des microcavites optiques", These de doctorat (Paris 6, Jan. 2000).

[148]S. Anguiano, P. Sesin, A. E. Bruchhausen, F. R. Lamberti, I. Favero, M. Esmann, I. Sagnes, A. Lemaître, N. D. Lanzillotti-Kimura, P. Senellart, and A. Fainstein, "Scaling rules in optomechanical semiconductor micropillars", Physical Review A **98**, 063810 (2018).

[149]S. Sun, H. Kim, G. S. Solomon, and E. Waks, "A quantum phase switch between a single solid-state spin and a photon", Nature Nanotechnology **11**, 539–544 (2016).

[150]C. Arnold, J. Demory, V. Loo, A. Lemaître, I. Sagnes, M. Glazov, O. Krebs, P. Voisin, P. Senellart, and L. Lanco, "Macroscopic rotation of photon polarization induced by a single spin", Nature Communications **6**, 6236 (2015).

[151]K. Halterman, S. Feng, and P. L. Overfelt, "Guided modes of elliptical metamaterial waveguides", Physical Review A **76**, 013834 (2007).

[152]S. Gerhardt, M. Deppisch, S. Betzold, T. H. Harder, T. C. H. Liew, A. Predojević, S. Höfling, and C. Schneider, "Polarization-dependent light-matter coupling and highly indistinguishable resonant fluorescence photons from quantum dot-micropillar cavities with elliptical cross section", Physical Review B **100**, 115305 (2019).

[153]C. W. Gardiner and M. J. Collett, "Input and output in damped quantum systems: Quantum stochastic differential equations and the master equation", Physical Review A **31**, 3761–3774 (1985).

[154]P. Hilaire, "A cavity-based spin-photon interface", These de doctorat (Sorbonne Paris Cité, June 2019).

[155]H. G. Jekrard, "Transmission of Light through Birefringent and Optically Active Media: the Poincaré Sphere", JOSA **44**, 634–640 (1954).

[156]C. Antón, P. Hilaire, C. A. Kessler, J. Demory, C. Gómez, A. Lemaître, I. Sagnes, N. D. Lanzillotti-Kimura, O. Krebs, N. Somaschi, P. Senellart, and L. Lanco, "Tomography of the optical polarization rotation induced by a single quantum dot in a cavity", Optica **4**, 1326–1332 (2017).

[157]D. H. Goldstein, *Polarized Light*, 3rd Edition (2011).

[158]J. Demory, "Initialisation de spin et rotation de polarisation dans une boîte quantique en microcavité", These de doctorat (Université Paris-Saclay (ComUE), Jan. 2016).

[159]K. O'Brien, N. D. Lanzillotti-Kimura, J. Rho, H. Suchowski, X. Yin, and X. Zhang, "Ultrafast acousto-plasmonic control and sensing in complex nanostructures", Nature Communications **5**, 4042 (2014).

[160]M. Esmann, S. F. Becker, J. Witt, J. Zhan, A. Chimeh, A. Korte, J. Zhong, R. Vogelgesang, G. Wittstock, and C. Lienau, "Vectorial near-field coupling", Nature Nanotechnology **14**, 698–704 (2019).

[161]M. Lejman, G. Vaudel, I. C. Infante, I. Chaban, T. Pezeril, M. Edely, G. F. Nataf, M. Guennou, J. Kreisel, V. E. Gusev, B. Dkhil, and P. Ruello, "Ultrafast acousto-optic mode conversion in optically birefringent ferroelectrics", Nature Communications **7**, 12345 (2016).

[162]O. Braun, R. Furrer, P. Butti, K. Thodkar, I. Shorubalko, I. Zardo, M. Calame, and M. L. Perrin, "Spatially mapping thermal transport in graphene by an opto-thermal method", npj 2D Materials and Applications **6**, 1–7 (2022).

[163]T. Jiang, Q. He, and Z.-K. Peng, "Enhanced directional acoustic sensing with phononic crystal cavity resonance", Applied Physics Letters **112**, 261902 (2018).

[164]F. Appas, F. Baboux, M. I. Amanti, A. Lemaítre, F. Boitier, E. Diamanti, and S. Ducci, "Flexible entanglement-distribution network with an AlGaAs chip for secure communications", npj Quantum Information **7**, 1–10 (2021).

[165]Q. Fontaine, D. Squizzato, F. Baboux, I. Amelio, A. Lemaître, M. Morassi, I. Sagnes, L. Le Gratiet, A. Harouri, M. Wouters, I. Carusotto, A. Amo, M. Richard, A. Minguzzi, L. Canet, S. Ravets, and J. Bloch, "Kardar–Parisi–Zhang universality in a one-dimensional polariton condensate", Nature **608**, 687–691 (2022).

[166]V. Villafañe, A. E. Bruchhausen, B. Jusserand, P. Senellart, A. Lemaître, and A. Fainstein, "Confinement of gigahertz sound and light in Tamm plasmon resonators", Physical Review B **92**, 165308 (2015).

[167]N. L. Abdala, M. Esmann, M. C. Fuertes, P. C. Angelomé, O. Ortiz, A. Bruchhausen, H. Pastoriza, B. Perrin, G. J. A. A. Soler-Illia, and N. D. Lanzillotti-Kimura, "Mesoporous Thin Films for Acoustic Devices in the Gigahertz Range", The Journal of Physical Chemistry C **124**, 17165–17171 (2020).

[168]P. Innocenzi and L. Malfatti, "Mesoporous thin films: properties and applications", Chemical Society Reviews **42**, 4198–4216 (2013).

[169]R. M. Gazoni, M. G. Bellino, M. C. Fuertes, G. Giménez, G. J. A. A. Soler-Illia, and M. L. M. Ricci, "Designed nanoparticle–mesoporous multilayer nanocomposites as tunable plasmonic–photonic architectures for electromagnetic field enhancement", Journal of Materials Chemistry C **5**, 3445–3455 (2017).

[170]G. Benetti, M. Gandolfi, M. J. Van Bael, L. Gavioli, C. Giannetti, C. Caddeo, and F. Banfi, "Photoacoustic Sensing of Trapped Fluids in Nanoporous Thin Films: Device Engineering and Sensing Scheme", ACS Applied Materials & Interfaces **10**, 27947–27954 (2018).

[171]J. Hu, W. Liu, W. Xie, W. Zhang, E. Yao, Y. Zhang, and Q. Zhan, "Strong coupling of optical interface modes in a 1D topological photonic crystal heterostructure/Ag hybrid system", Optics Letters **44**, 5642–5645 (2019).

[172]D. Li, H. Shan, C. Rupprecht, H. Knopf, K. Watanabe, T. Taniguchi, Y. Qin, S. Tongay, M. Nuß, S. Schröder, F. Eilenberger, S. Höfling, C. Schneider, and T. Brixner, "Hybridized Exciton-Photon-Phonon States in a Transition Metal Dichalcogenide van der Waals Heterostructure Microcavity", Physical Review Letters **128**, 087401 (2022).

[173]V. Goblot, A. Štrkalj, N. Pernet, J. L. Lado, C. Dorow, A. Lemaître, L. Le Gratiet, A. Harouri, I. Sagnes, S. Ravets, A. Amo, J. Bloch, and O. Zilberberg, "Emergence of criticality through a cascade of delocalization transitions in quasiperiodic chains", Nature Physics **16**, 832–836 (2020).

[174]M. Verbin, O. Zilberberg, Y. Lahini, Y. E. Kraus, and Y. Silberberg, "Topological pumping over a photonic Fibonacci quasicrystal", Physical Review B **91**, 064201 (2015).

[175]Y. E. Kraus, Y. Lahini, Z. Ringel, M. Verbin, and O. Zilberberg, "Topological States and Adiabatic Pumping in Quasicrystals", Physical Review Letters **109**, 106402 (2012).